Doctorate Dissertation

博士論文

Fast solar wind driven by parametric decay instability and Alfvén wave turbulence

(減衰不安定とアルフベン波乱流により駆動される高速太陽風)

A Dissertation Submitted for Degree of Doctor of Philosophy

December 2018

平成 30 年 12 月博士（理学）申請

Department of Earth and Planetary Science

Graduate School of Science, The University of Tokyo

東京大学大学院理学系研究科地球惑星科学専攻

Munehito Shoda

庄田宗人

Contents

Abstract

A continuous injection of energy and momentum is required to sustain the high-temperature corona and high-speed solar wind. A widely accepted idea is that the origin of such energy and momentum lies in the convective motion of the solar surface (photosphere) and the magnetic field transports them to upper atmosphere via Alfvén wave, which is called Alfvén-wave modeling or Alfvén wave scenario of the (fast) solar wind. Although the general framework of Alfvén-wave modeling is, at least theoretically, of little doubt, the detailed physics inside is yet controversial. Specifically, the thermalization mechanism of Alfvén wave in the corona and solar wind is unclear. Bearing in mind that the (magnetic) Reynolds number is quite large, turbulence and resultant cascading are required to obtain adequate heating.

A standard model, called reflection-driven Alfvén wave turbulence model, assumes that inward Alfvén waves generated by a partial reflection in the solar wind collide with outward Alfvén waves, triggering Alfvén wave turbulence to heat the solar wind. One problem that recently arose regarding this model is that the heating rate is insufficient. Therefore, we need to revisit and modify the standard model, incorporating new physics.

The standard model is based on reduced MHD equations in which compressional waves are ruled out. We assume that the shortage of heating is attributed to neglecting compressional waves. An overall motivation of this thesis is to update the standard model including compressional waves. Permission of compressibility is crucial in the solar wind, where plasma beta is low, because parametric decay instability works with a comparable time scale to Alfvén wave turbulence. For this purpose, we have performed two different simulations: one-dimensional and three-dimensional simulations.

In Chapter 3, we report the results of one-dimensional simulations. To consider the turbulent heating in one-dimensional geometry, we introduce a phenomenological turbulence model of Alfvén wave turbulence into compressible MHD equations. The turbulence model is set so that it becomes equivalent with commonly used Alfvén wave turbulence model in the limit of incompressibility. In the limit of infinite turn over time of turbulence, this model is identical to the previous work without turbulence. We have found that the dominant heating process in the solar wind is correlation-length dependent; with small correlation length most of the heating is by turbulence and with large correlation length shock heating is dominant. With the realistic correlation length, the turbulence is slightly stronger than shock. Using parameter survey, we have revealed several conclusions. First, the solar wind velocity is strongly affected by correlation length while the magnitude of energy injection determines the mass-loss rate. This result is consistent with previous works. Second, the observed large density fluctuation in the solar wind acceleration region is explained by parametric decay instability. Specifically, the largest-density-fluctuation region is the same as the largest-growth-rate region of parametric decay instability. Third, the cross-helicity evolution is explained based on linear reflection. These indicate that parametric decay instability plays a crucial role in the solar wind acceleration region but not in the distant solar wind.

In Chapter 4, we show the results of the three-dimensional simulation, the motivations of which are to validate the 1D model and to predict the data of *Parker Solar Probe*. Our simulation is the first-ever three-dimensional self-consistent simulation of the solar wind acceleration. Large density fluctuation is generated by parametric decay instability in the wind acceleration region consistently with 1D simulation. The turbulence in the solar wind is characterized by an imbalanced MHD turbulence in which the power spectra of outward and inward waves have different power indices. As a prediction of *Parker Solar Probe*, we have shown that the positive correlation between density and parallel-velocity fluctuations would be observed.

As a conclusion of this thesis, we propose an updated standard model of the solar wind

acceleration: the PDI-driven Alfvén wave turbulence model. Alfvén wave reflection, the source of turbulence in the solar wind, is triggered not only by simple linear refection but also by the parametric decay instability. The compressible waves plays a crucial role in the solar wind turbulence and therefore is never ignorable in the simulation.

Acknowledgments

It was really lucky for me that I had a chance to take a class by Takaaki Yokoyama, my supervisor. Without him, I would never have studied astrophysics. All of my work I have accomplished are thanks to his continuous encouragement and endless patience. I cannot thank him enough. My colleagues of Yokoyama lab also helped me through various discussions. It was my great honor to be a member of our laboratory.

I would also like to show my gratitude to all the members in Space Science Group in the Department of Earth and Planetary Science, School of Science, The University of Tokyo. Seminars in our group are always enjoyable and stimulating, and sometimes tough. All the questions and comments helped me improve my work.

During my visit in US, I was supported by Dr. Mahboubeh Asgari-Targhi and her family. I would like to express my appreciation to her. Thanks to her, I experienced and learned a lot of valuable things, including how I should behave when we lose our passport abroad and have to go back to Japan in three days! I also learned the importance of collaboration and discussion with others from her. I owe my growth as a researcher to her.

I have been supported by the Research Fellowship for Young Scientists of the Japan Society for the Promotion of Science (JSPS) and Leading Graduate Course for Frontiers of Mathematical Sciences and Physics (FMSP). Nearly all the numerical calculations are carried out on PC cluster, Cray XC30 and Cray XC50 at Center for Computational Astrophysics, National Astronomical Observatory of Japan.

Finally, I would like to express my special appreciation to my family and my fiancée Kanako for their continuous supports.

Chapter 1

General introduction:

Alfvén-wave modeling of the solar wind

The role of Alfvén waves in the fast solar wind is almost doubtless for two reasons. First, Parker's solar wind model and its extension cannot explain several observations of the solar wind without an additional driving force of the wind other than gas pressure. Second, Alfvén waves are now observed ubiquitously in the solar atmosphere to have sufficiently large energy to affect the solar wind formation. Here as the first Chapter of this thesis, we briefly summarize why the Alfvén wave modeling of the fast solar wind is necessary and accepted.

1.1 Parker's solar wind model

As the most fundamental theory of solar wind, we begin with Parker's solar wind model (Parker, 1958, 1965). Bearing in mind that the Sun has a hot atmosphere with temperature exceeding 10^6 K (Edlén, 1943) and that a continuous plasma outflow is suggested from comet tail observation (Biermann, 1957), Parker proposed an idea that the Sun should have a transonic outflow.

1.1.1 Hydrostatic solar atmosphere with thermal conduction

Suppose the solar atmosphere has no radial velocity and the atmosphere satisfies a hydrostatic equilibrium as

$$\frac{d}{dr}(2nk_BT) = -nm_p\frac{GM_\odot}{r^2}, \tag{1.1}$$

where n is the number density of hydrogen, k_B is the Boltzmann constant, T is the hydrogen temperature, m_p is the hydrogen (proton) mass, G is the gravitational constant, and $M_\odot$ is the solar mass. The solution of this equation is given as

$$p = p_\odot \exp\left[-\frac{m_pGM_\odot}{2k_B}\int_{r_\odot}\frac{dr}{r^2T(r)}\right]. \tag{1.2}$$

Suppose that $\lim_{r\to\infty} p = 0$ is required (to sustain the hydrostatic equilibrium). The actual asymptotic value of p is as large as the interstellar pressure $p_{\rm IS}$, which is negligibly small in the context of solar atmosphere and solar wind. Eq. (1.2) shows that this boundary condition is satisfied only when T decreases more rapid than $1/r$.

Chapman & Zirin (1957) showed, however, that T does not decrease so rapidly in the presence of thermal conduction. According to Spitzer & Härm (1953), the thermal conductive flux $F_{\rm cnd}$ is written in terms of T as

$$F_{\rm cnd} = -\kappa_0 T^{5/2}\frac{d}{dr}T, \tag{1.3}$$

where $\kappa_0 \approx 10^{-6}$ in cgs unit. The stationary condition requires that, in the absence of mechanical energy flux, the cooling and heating by $F_{\rm cnd}$ balances everywhere:

$$\frac{d}{dr}\left(4\pi r^2 F_{\rm cnd}\right) = 0. \tag{1.4}$$

Imposing the boundary condition $\lim_{r\to\infty} T = 0$, this is solved as

$$\frac{T}{T_\odot} = \left(\frac{r}{R_\odot}\right)^{-2/7}, \tag{1.5}$$

which yields a finite pressure at infinity. Thus, when the thermal conduction is at play, the hydrostatic atmosphere cannot be sustained.

1.1.2 Isothermal wind

In stead of hydrostatic equilibrium, Parker (1958) considered the dynamical equation of isothermal atmosphere and the solutions of them. The basic equations of the stationary expanding, isothermal atmosphere are

$$\frac{d}{dr}\left(\rho v_r r^2\right) = 0, \qquad v\frac{dv}{dr} = -\frac{1}{\rho}\frac{dp}{dr} - \frac{GM_\odot}{r^2}, \qquad p = a^2\rho, \tag{1.6}$$

where a denotes the sound speed. These equations are reduced to the following ordinary differential equation:

$$\left(v - \frac{a^2}{v}\right)\frac{dv}{dr} = \frac{2a^2}{r^2}\left(r - r_c\right), \tag{1.7}$$

where $r_c = GM_\odot/2a^2$. Eq. (1.7) has, as far as the author's knowledge, no analytic solution, but the qualitative behavior is easily understood. The sign of dv/dr is determined by $(v^2 - a^2)/v$ and $(r - r_c)$, and if always $v < a$, the solution has maximum at $r = r_c$. This is, however, not the case when the wind velocity reaches sound speed a at $r = r_c$, In such case, the wind velocity continues to increase beyond r_c and transit from subsonic to supersonic. The existence of this *transonic* solution was the most interesting point in Parker (1958). Figure 1.1 shows the typical solutions of the isothermal wind with two lines indicating the transonic and subsonic solutions.

Note that both subsonic and transonic winds can exist as a solution of stationary expansion while the actual solar wind is always transonic. One possibility for this is that the

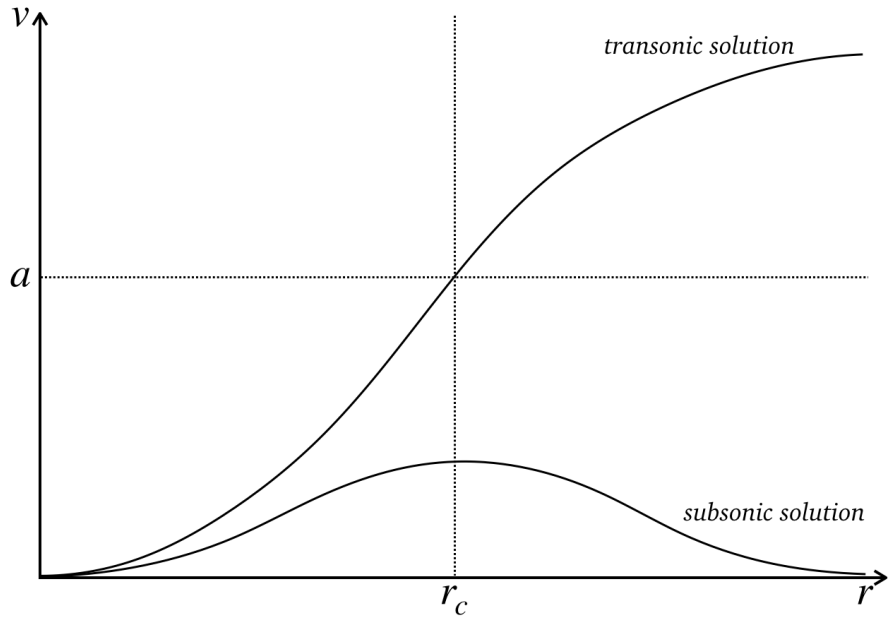

Figure 1.1: Typical solutions of the isothermal wind equation Eq. (1.7) with subsonic basal speed. Higher and lower lines indicate the transonic and subsonic solutions, respectively.

subsonic solution is unstable (Velli, 1994). It seems contradictory that the nature prefers the transonic solution that requires the condition $v_{r=r_c} = a$. This is one reason why Parker's theory was not always acceptable before the observation of the solar wind (see Gombosi et al. (2018) for detailed history).

1.1.3 Generalization of Parker model

The isothermal wind model is generalized in a straightforward way to the polytropic wind model or the conductive wind model (Parker, 1965). An interesting result of the polytropic wind theory is that the adiabatic wind ($p \propto \rho^{5/3}$) cannot exist. In terms of energetics, this means that the solar wind needs energy injection to make the practical polytropic index smaller than $5/3$. The classical models assume that the thermal conduction is a source for such energy injection or transport in the distant solar wind. This is why the classical models are called conductive wind model.

Several generalizations are proposed to the conductive wind models. Sturrock & Hartle (1966) and Hartle & Sturrock (1968) solve the energy equations of ion and electron separately to show that the conductive wind model cannot account for the ion temperature in the solar wind. In the collisionless solar wind, since electron cannot feed thermal energy to ion, the only heating mechanism of ion is the ion thermal conduction, which is too weak to sustain the high temperature against the adiabatic expansion. This indicates that ion should experience in-situ heating during the wind expansion. Although such heating mechanism is yet unclear, it should be associated with Alfvén waves because there exists a clear correlation between wind velocity and ion temperature; the fast solar wind, in which Alfvén waves dominate the fluctuations inside, shows higher ion temperature (Elliott et al., 2012; Cranmer et al., 2017).

Spitzer-Härm type thermal conduction (Spitzer & Härm, 1953) is widely assumed to work in the solar wind. However, some studies indicate that the Spitzer-Härm type thermal conduction is not applicable to the collisionless solar wind (Perkins, 1973; Hollweg, 1974, 1976). Hollweg (1976) proposed a new conductive flux that is applicable to the collisionless system, so called free-streaming flux given as

$$q_{\rm cnd} = \frac{3}{4}\alpha p v_r, \tag{1.8}$$

where α is a free parameter, p is the pressure and v_r is the solar wind velocity. Although free-streaming flux should be more realistic than Spitzer-Härm flux in the collisionless case, how to connect the Spitzer-Härm type conductive flux and free-streaming conductive flux remains controversial. Cranmer et al. (2007) and van Ballegooijen & Asgari-Targhi (2016) assume a bridging law between Spitzer-Härm flux and free-streaming flux in terms of dynamical expansion timescale and collision timescale, while Hollweg (1986) and Lionello et al. (2014) simply switches the flux in a radial-distance-dependent manner.

Another important generalization includes the super-radial expansion of the magnetic flux tube in the solar wind. Kopp & Holzer (1976) generalized Parker's wind model considering the expansion of the stream. One important effect of super radial expansion

is that multiple critical points (where the wind velocity equals sound speed) can exist. With large expansion in the vicinity of the Sun, the critical point becomes much closer to the Sun than Parker's model. This is crucial when we discuss the external energy and momentum injection (see Section 1.1.4), because the wind becomes slower when the bulk of energy/momentum injection is inside the critical point and vice versa.

There are several comprehensive parameter surveys of the conductive wind model (Durney, 1972; Durney & Hundhausen, 1974; Holzer & Leer, 1980). Most of the parameter surveys investigate the dependence on the coronal density and temperature. None of them, however, successfully explain the observations of the fast solar wind with realistic coronal values

1.1.4 External energy/momentum injection

The conductive wind model cannot account for the fast solar wind for two reasons. First, the conductive wind model is contradictory to the anti-correlation between the freezing-in temperature and wind velocity (von Steiger et al., 2000; Cranmer et al., 2017). The freezing-in temperature of the solar wind is the temperature calculated from the ionization state. In the collisionless solar wind, the freezing-in temperature represents the temperature of the source region. According to observation, the fast and slow solar winds blow out from cool and hot regions, respectively. This is contradictory to the conductive wind model, in which the thermal pressure gradient is the driving force to push plasma outward and faster wind is generated by hotter atmosphere. Second, the conductive wind model cannot explain the nearly constant mass-loss rate. The conductive wind model yields faster wind with much larger density than the slower wind, which is opposite to observation.

The pioneering work of the solar wind with external energy and momentum addition is by Leer & Holzer (1980). They show using parameter survey that the fast solar wind is explained by heat/momentum addition in the supersonic region. The model of Leer & Holzer (1980) is further extended by Hammer (1982) and Withbroe (1988) by including

the effect of chromospheric evaporation, that is, when the coronal heating is enhanced, the chromospheric plasma is heated up by thermal conduction to evaporate upward, making the corona heavier. Although neither Hammer (1982) nor Withbroe (1988) solve the chromosphere, this evaporation effect is included by changing the coronal density by the balance between conduction heating and radiative cooling. Hansteen & Leer (1995) further generalized these model by including chromosphere.

1.2 Alfvén-wave as a source of energy and momentum

1.2.1 Alfvén-wave heating and acceleration of the solar wind

Alfvén wave is a promising candidate of the source of energy and momentum. It is widely accepted that the solar wind is powered by the energy of magneto-convection on the photosphere (Steiner et al., 1998; van Ballegooijen et al., 2011). Alfvén wave can efficiently transport the energy of convective motion up to the distant solar wind, because Alfvén waves experience neither steepening nor refraction that are critically important for slow and fast mode waves.

The idea of Alfvén wave heating of the solar atmosphere dates back to Alfvén (1947) and Osterbrock (1961). Since the discovery of large-amplitude Alfvén waves, the solar wind acceleration by Alfvén-wave pressure is also widely studied (Alazraki & Couturier, 1971; Belcher, 1971; Jacques, 1977; Heinemann & Olbert, 1980). It is easily understood that Alfvén waves can push plasma when propagating in a stratified atmosphere. Suppose the energy flux of Alfvén wave is conserved, the magnetic fluctuation of Alfvén wave δB satisfies

$$\frac{\delta B^2}{4\pi} v_A S = \text{const.}, \tag{1.9}$$

where v_A is the Alfvén speed and S is the cross section of flux tube. Using the magnetic

flux conservation ($BS = \text{const.}$), we obtain

$$\frac{\delta B^2}{8\pi} = p_{\rm AW} \propto \rho^{1/2}, \tag{1.10}$$

where $p_{\rm AW}$ is the Alfvén wave pressure. Thus the acceleration rate by Alfvén wave pressure ($a_{\rm AW}$) is given by

$$a_{\rm AW} = -\frac{1}{\rho}\frac{d}{dr}p_{\rm AW} \propto -\frac{1}{\rho^{1/2}}\frac{d}{dr}\ln\rho. \tag{1.11}$$

Given that the density drops off exponentially with length scale H, the acceleration rate satisfies

$$a_{\rm AW} \propto \frac{1}{H}\rho^{-1/2}. \tag{1.12}$$

This indicates that the wave acceleration works efficiently in the distant region where ρ is low. Thus Alfvén wave is a promising candidate for the momentum injection in the supersonic region, which is essential in making the fast solar wind.

1.2.2 Observations of Alfvén waves in the solar atmosphere

There exists a number of observations that indicate Alfvén waves in the solar atmosphere. An overview of the observations of Alfvén waves in the solar wind is given in Figure 1.2. A number of techniques are used to detect Alfvén waves including imaging, spectroscopy and in-situ measurement. In the vicinity of the solar surface, imaging of transverse motion is widely used to detect Alfvén(ic) waves in the solar atmosphere. On the photosphere, tracking of granular motions (Matsumoto & Kitai, 2010) or bright-point motions (Chitta et al., 2012) are used to measure the transverse velocity, both of which yield velocity amplitude of approximately $1 - 2\ \mathrm{km\ s^{-1}}$. The energy flux of the photospheric transverse motion is in the order of $10^9\ \mathrm{erg\ cm^{-2}\ s^{-1}}$, which is much larger than the energy flux required for chromospheric heating, coronal heating and solar wind acceleration (Withbroe

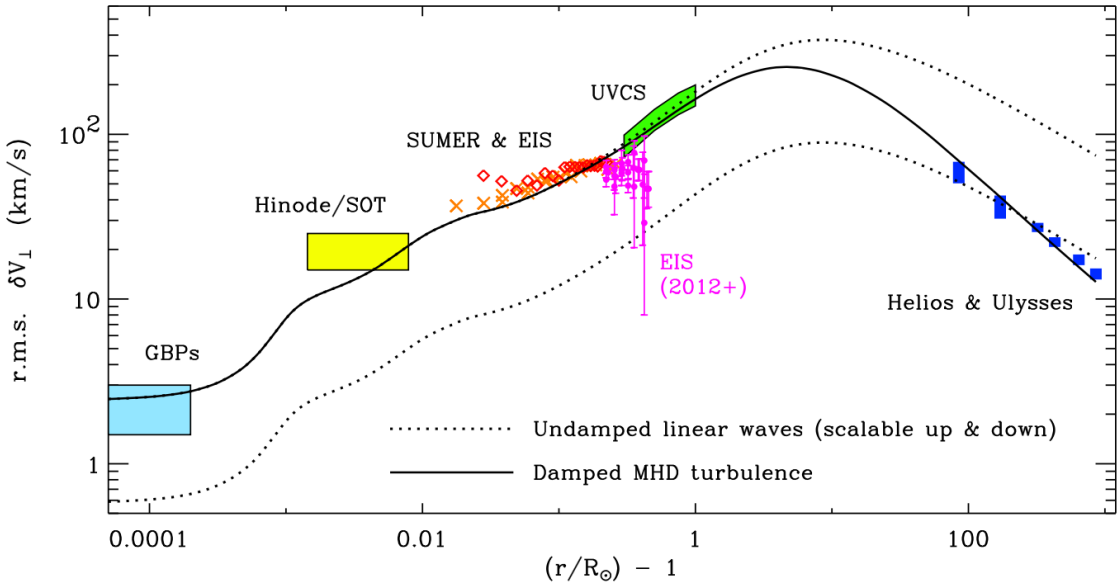

Figure 1.2: A compilation of the observations of Alfvén waves from the photosphere to the distant solar wind. Shown by solid and dashed lines are the theoretical models by Cranmer et al. (2007). Figure reproduced from Cranmer et al. (2017).

& Noyes, 1977).

The detection of Alfvén waves becomes much difficult in the higher atmosphere because of the superposition effect along the line of sight. When multiple waves exist with comparable contributions to observation, the observed quantity involve a mixture of contributing waves. To avoid this problem, an isolated wave guide such as jet-like structure is required for wave diagnostics. Such observation suffers from the limitation that waves with longer period than the lifetime of jet is in principle not detectable. To overcome such limitation, De Pontieu et al. (2007) use Monte-Carlo simulation together with *Hinode*/SOT observations to obtain the amplitude and period of the chromospheric Alfvén waves as $10 - 25\ \mathrm{km\ s^{-1}}$ and $100 - 500\ \mathrm{s}$, respectively. Such waves have sufficiently large power to drive the solar wind. A similar method is used to diagnose the coronal waves by *SDO*/AIA (McIntosh et al., 2011), obtaining the similar result with De Pontieu et al. (2007).

When we have an isolated wave guide, by investigating the oscillation of it, a direct

analysis becomes available. Okamoto & De Pontieu (2011) perform a statistical analysis of spicule oscillations to show that the high-frequency waves with period $\sim 40 - 50$ s are dominantly observed. Srivastava et al. (2017) also observes these high-frequency oscillations and shows that these high-frequency waves can potentially heat the corona. These high-frequency waves are possibly generated by mode conversion (Shoda & Yokoyama, 2018b). Meanwhile an imaging analysis of coronal plume oscillation indicates that the wave amplitude is not sufficiently large to drive the solar wind (Thurgood et al., 2014). Although it is widely accepted that upward Alfvén waves exist from the chromosphere to the coronal base, the properties of them are still on debate.

Indirect methods are used to detect waves in the tenuous corona and solar wind where imaging is no longer available. One of such methods are to measure the non-thermal broadening of spectral lines. When incoherent wave motions exist in the line-of-sight, because of the super position of random Doppler shift, the spectral line becomes broader than is expected from thermal broadening. Such wave/turbulence-induced line broadening is called non-thermal line broadening and is used to diagnose the turbulence intensity. In the vicinity of the Sun, SOHO/SUMER (Banerjee et al., 1998; Teriaca et al., 2003) and Hinode/EIS (Banerjee et al., 2009; Hahn & Savin, 2013) are widely used to observe the line profiles in the corona. In the farer region, the spectral lines are observed by SOHO/UVCS (Esser et al., 1999). As Figure 1.2 shows, the non-thermal broadening tends to increase with radial distance, indicating the upward wave propagation. One exceptional observation is by Hahn & Savin (2013) (pink symbols in Figure 1.2). In their analysis, the line broadening saturates at a certain height, which is contradictory with the other observations or theory.

In the interplanetary space beyond 0.3 au from the Sun, the velocity fluctuation is observed by in-situ measurements, mainly by Helios (inner heliosphere) and Ulysses (outer heliosphere) (Bavassano et al., 1982, 2000). The radial evolution of Alfvén waves given by these spacecrafts is consistent with simple linear propagation of Alfvén waves (Verdini & Velli, 2007).

1.2.3 Numerical simulations based on Alfvén wave modeling

Based on the background above, several theoretical models explains the solar wind acceleration based on Alfvén wave heating and acceleration. Velli et al. (1989) proposes an idea that unidirectional Alfvén waves can drive turbulence in the inhomogeneous solar wind. This idea is extended to coronal heating by Matthaeus et al. (1999) and now is called reflection-driven Alfvén wave turbulence model. A number of theoretical works based on Alfvén wave turbulence model shows that the observed Alfvén waves have potential to explain the observed solar wind via turbulent heating (Cranmer et al., 2007; Verdini et al., 2010; Chandran & Hollweg, 2009; Chandran et al., 2011; Usmanov et al., 2011; Lionello et al., 2014; van der Holst et al., 2014; Usmanov et al., 2018). Meanwhile, some models explain the fast solar wind without turbulence (Suzuki & Inutsuka, 2005, 2006) based on mode conversion to slow mode waves (Hollweg et al., 1982; Kudoh & Shibata, 1999; Matsumoto & Shibata, 2010). A common conclusion of these models is that, as long as Alfvén wave dissipates with appropriate rate in the solar wind, the fast solar wind is well explained. For more precise understanding, not only the averaged parameter such as wind velocity or density but also the fluctuations and turbulence inside should also be explained.

Chapter 2

Open questions and motivations

It is now widely accepted that the fast solar wind experiences non-thermal acceleration in addition to gas pressure acceleration. Wave pressure (or Maxwell stress) associated with Alfvén wave is a promising candidate for such additional momentum source. Alfvén wave and turbulence are also believed to be responsible for heating the corona and solar wind to the observed temperature. The current understanding is that the formation of fast solar wind is a natural consequence of Alfvén wave propagation and dissipation in the open field regions.

In spite of the consensus that Alfvén waves are necessary in the fast solar wind formation, several issues are still open, such as wave dissipation mechanism, origin of turbulent structure and scaling law of mass-loss rate. We summarize the open questions and motivations of this thesis in this Chapter.

2.1 Physical mechanism for Alfvén wave dissipation

There is almost no doubt that Alfvén waves play a central role in the fast solar wind. Several numerical simulations show that the corona and fast solar wind is formed when the magnetic field line anchored on the photospheric magnetic patches (Tsuneta et al., 2008) is shuffled with the observed velocity (Suzuki & Inutsuka, 2005; Cranmer et al., 2007; Matsumoto & Suzuki, 2014). However, the physical mechanism regarding Alfvén

wave dissipation is yet unclear. Let us review the standard understanding and the problem of it.

2.1.1 Standard model

The standard scenario of the Alfvén wave dissipation (or the conversion of Poynting flux to heat) is called reflection-driven Alfvén wave turbulence model (Velli et al., 1989; Matthaeus et al., 1999). Due to the inhomogeneity of the corona and solar wind, Alfvén waves are partially reflected (Ferraro & Plumpton, 1958; Heinemann & Olbert, 1980; An et al., 1990; Velli, 1993; Hollweg & Isenberg, 2007) to trigger the collision of outward and inward Alfvén waves. Such collision would drive MHD turbulence to heat the corona and accelerate the solar wind.

A numerical demonstrations of Alfvén wave turbulence scenario are performed by Oughton et al. (2001) and Dmitruk et al. (2002). Dmitruk et al. (2002) solved the reduced MHD equations (MHD equations without compressional waves) from the coronal base to the upper corona to show that laminar waves at the bottom evolve to turbulent waves in the upper corona because of wave reflection. Figure 2.1 shows the horizontal profiles of field-aligned electric current (that is enhanced by Alfvén wave turbulence) in the upper corona (top panel) and at the coronal base (bottom panel). As a result of turbulence, finer-scale structures are observed in the upper layer.

In the quasi-steady state, the averaged plasma heating rate is the same as averaged cascading rate that is determined by energy containing scale. This is a motivation to model the plasma heating rate in terms of large-scale or averaged amplitude of Alfvén waves. Using a turbulence model by Hossain et al. (1995), Dmitruk et al. (2002) compare the heating rate directly calculated from simulation and phenomenologically obtained from turbulence model. Figure 2.2 compares the directly calculated heating rate (thin line) and phenomenologically estimated heating rate (thick line). The two lines are in agreement with each other, validating the turbulence model.

The phenomenological model of Dmitruk et al. (2002) have been widely used. Sev-

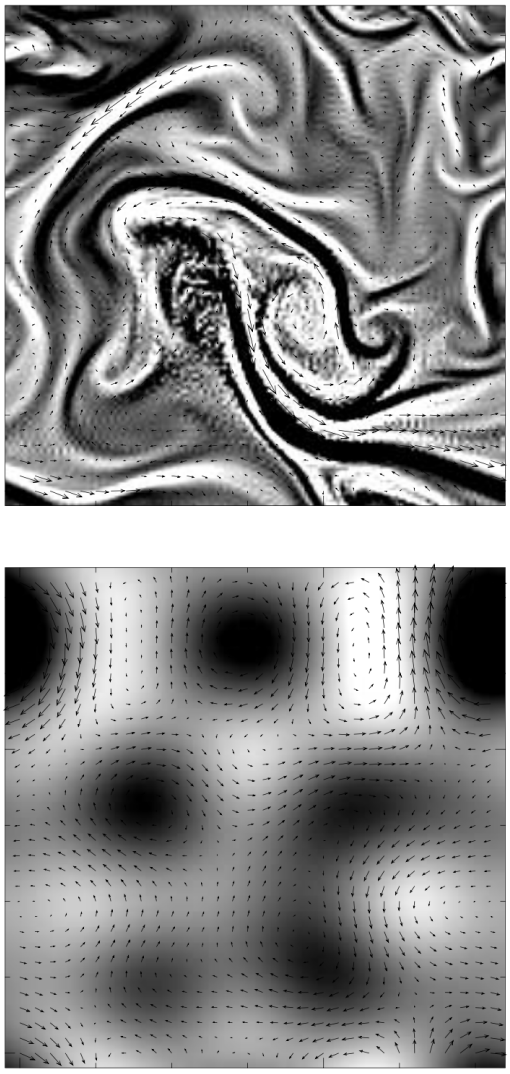

Figure 2.1: Horizontal profiles of the electric current along the mean magnetic field in the upper corona (top panel) and at the coronal base (bottom panel). Figure reproduced from Dmitruk et al. (2002).

eral works study the wave propagation with phenomenological turbulent dissipation to show that the turbulent heating is sufficiently large to sustain the solar wind (Cranmer & van Ballegooijen, 2005; Verdini & Velli, 2007; Chandran & Hollweg, 2009). These works are extended to self-consistent modeling that solves the feedback from the waves to background (Cranmer et al., 2007; Verdini et al., 2010; Lionello et al., 2014).

Increasing capability of super computer has recently enabled us to directly solve the

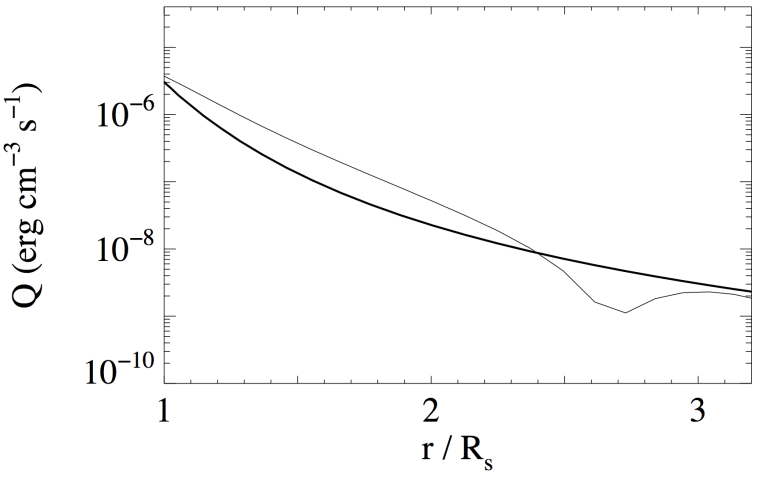

Figure 2.2: Plasma heating rates per unit mass directly calculated from simulation (thin line) and estimated from turbulence model (thick line) versus radial distance. Figure reproduced from Dmitruk et al. (2002).

reduced MHD equations without phenomenological model. The results, however, turned out in a negative manner; the direct numerical simulation yields much smaller heating rate compared with the phenomenological model. According to the results by Perez & Chandran (2013), the heating rate directly calculated from simulation does not exceed 10^{11} erg g^{-1} s^{-1} that is required to sustain the fast solar wind (Cranmer et al., 2007; Verdini et al., 2010; Chandran et al., 2011). The discrepancy between the calculated and required heating rates is discussed in more detail by van Ballegooijen & Asgari-Targhi (2016) and van Ballegooijen & Asgari-Targhi (2017). Figure 2.3 shows the heating rates calculated from three-dimensional reduced MHD simulation (black-solid line), calculated from the phenomenological model (blue line), and required to sustain the fast solar wind (black-dashed line) as functions of height. There exists roughly one-order-of-magnitude difference between the required and calculated heating rates, indicating the insufficient heating by Alfvén wave turbulence. Meanwhile, the phenomenological model yields sufficient heating. One possible reason is that the inverse cascading is not considered in the phenomenological model (van Ballegooijen & Asgari-Targhi, 2017).

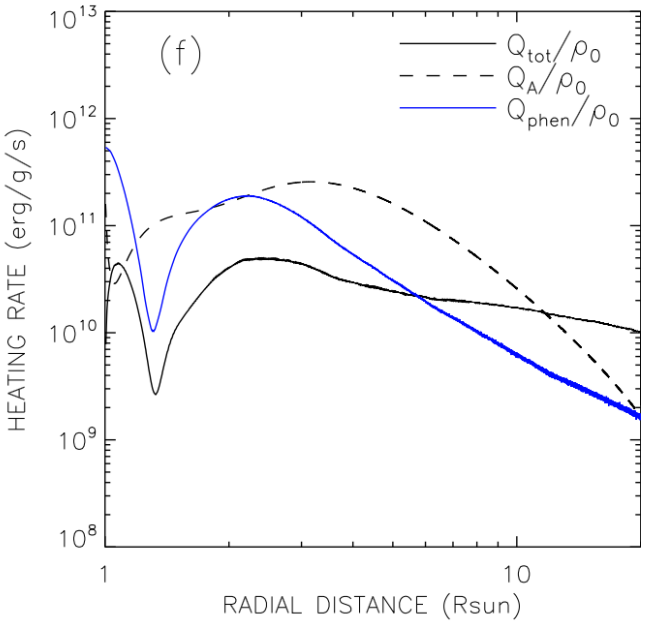

Figure 2.3: Heating rates required to sustain the solar wind (black dashed line) and obtained from 3D reduced MHD calculation (black solid line). Shown by blue solid line is the heating rate given by the phenomenological model. Figure reproduced from van Ballegooijen & Asgari-Targhi (2016).

One solution to compensates the gap between required and simulated heating rates is to introduce density fluctuation. This is because the density fluctuation enhances the wave reflection to promote Alfvén wave turbulence. van Ballegooijen & Asgari-Targhi (2016) show that density fluctuation with relative amplitude of 10% can drastically enhance the heating rate to be sufficient. Figure 2.4 shows the heating rates with 10% density fluctuation uniformly distributed from the coronal base to the solar wind. Alfvén wave turbulence in this case generates sufficiently large heating rate to sustain the fast solar wind.

Several observations show that large ($\sim 10\%$) density fluctuation does exist in the solar wind. Figure 2.5 is a compilation of various observations of density fluctuation in the solar wind. Blue rectangle near $r = 4R_\odot$ (Coles & Harmon, 1989; Spangler, 2002; Harmon & Coles, 2005) and black circles (Miyamoto et al., 2014) are obtained from radio-wave observations, while red and green rectangles approximate the density fluctu-

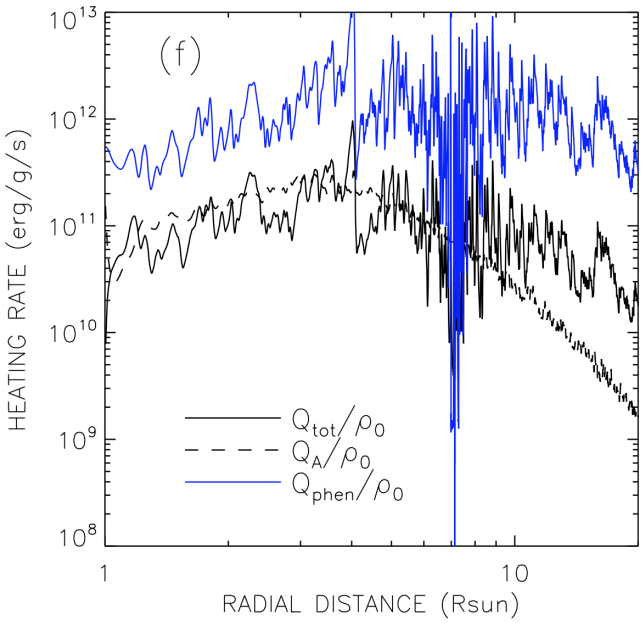

Figure 2.4: Same as Figure 2.3 but with density fluctuation. Figure reproduced from van Ballegooijen & Asgari-Targhi (2016).

ation reported in Marsch & Tu (1990). Not shown in this Figure, but recent observation of the coronal intensity fluctuation also shows the large ($\gtrsim 10\%$ of mean value) density fluctuation in $r > 1.2R_\odot$ (Hahn et al., 2018).

2.1.2 PDI as an origin of additional heating and reflection

The presence of non-negligible density fluctuation is of little doubt. Furthermore, recent simulation indicates that density fluctuation is essential in explaining the heating of the solar wind. The origin of the density fluctuation is, however, yet unclear. We aim to explain the origin and the magnitude of the observed density fluctuation in the solar wind.

Numerical simulations based on compressible MHD equations reveal that the density fluctuation is a natural consequence of Alfvén wave propagation in the solar wind. Suzuki & Inutsuka (2005) perform 1D compressible MHD simulation of the fast solar wind to show that the density is highly fluctuating in the wind acceleration region. This is later confirmed by 2D compressible MHD simulation by Matsumoto & Suzuki (2012) as seen

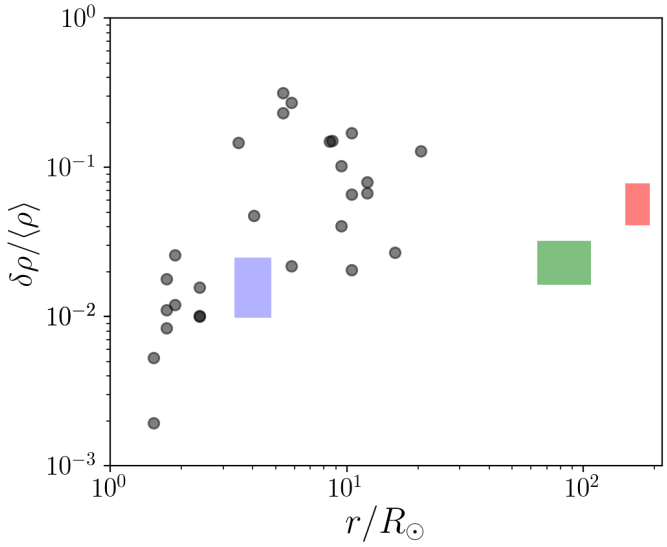

Figure 2.5: Compilation of the density fluctuation observation in the solar wind. Red and green rectangles approximate the density fluctuation reported in Marsch & Tu (1990). Blue rectangle near $r = 4R_\odot$ (Coles & Harmon, 1989; Spangler, 2002; Harmon & Coles, 2005) and black circles (Miyamoto et al., 2014) are from radio-wave observations.

in Figure 2.6. In the solar wind acceleration region ($2.5R_\odot \gtrsim r \gtrsim 10R_\odot$), density fluctuation becomes as large as a few tens percent. According to time-space diagram in Suzuki & Inutsuka (2006), the density fluctuation is slow mode (acoustic) waves. Since acoustic waves of photospheric origin dissipates quickly due to steepening, the slow mode waves in the solar wind should be in-situ generated waves.

The parametric decay instability (hereafter PDI) can be a source of slow mode waves in the solar wind. Via PDI, Alfvén waves resonantly collapses into forward acoustic waves and backward Alfvén waves. The growth rate of PDI is higher in lower-beta plasma, and thus the corona and solar wind are preferential regions for PDI growth. Recent theoretical (Tenerani & Velli, 2013; Réville et al., 2018) and observational (Bowen et al., 2018) studies indicate that PDI works in the solar wind.

The shortage of heating in the standard model is possibly solved by introducing PDI for two reasons. First, by generating slow shock waves, PDI directly enhance heating rate by adding shock wave heating. Second, by generating density fluctuation, Alfvén wave

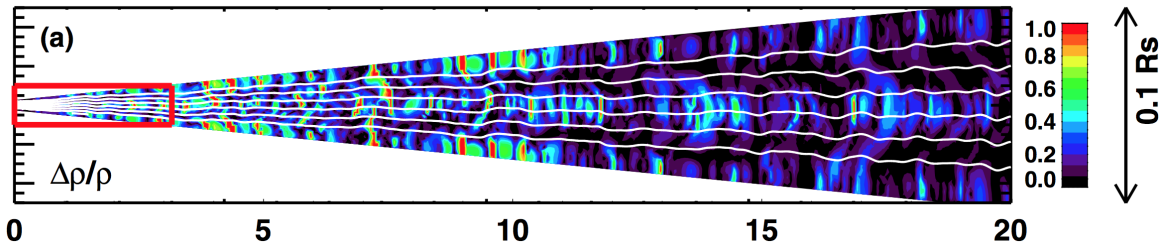

Figure 2.6: A snapshot of density fluctuation in the meridional plane with horizontal axis radial distance in the solar wind. Color contours indicate the magnitude of density fluctuation and white lines are magnetic field lines. Figure reproduced from Matsumoto & Suzuki (2012).

reflection is promoted. The enhanced reflection amplifies the turbulence, enhancing the heating rate.

2.1.3 Timescales of PDI and turbulence

PDI and turbulence work with similar timescales. The timescale of PDI ($\tau_{\rm PDI}$) is estimated by the growth rate given by Sagdeev & Galeev (1969):

$$\tau_{\rm PDI} \approx 1/\gamma_{\rm PDI}, \quad \gamma_{\rm PDI} = \frac{1}{2}\frac{\delta B}{B_0}\beta^{-1/4}\omega_0, \tag{2.1}$$

where B_0 and δB are the mean and fluctuation parts of magnetic field, $\beta = a^2/v_A^2$ is the (conventional) plasma beta, and ω_0 is the (typical) frequency of Alfvén wave. $\tau_{\rm PDI}$ is given as

$$\tau_{\rm PDI} \approx 10^3 \ {\rm s} \left(\frac{\delta B/B_0}{10^{-1}}\right)^{-1} \left(\frac{\beta}{10^{-2}}\right)^{1/4} \left(\frac{f_0}{10^{-3}\ {\rm Hz}}\right)^{-1}, \tag{2.2}$$

where we use $f_0 = \omega_0/2\pi$ instead of ω_0. Specifically, for the typical solar wind parameters ($\delta B/B_0 = 0.1$, $\beta = 0.01$), $\tau_{\rm PDI}$ is approximated as

$$\tau_{\rm PDI} \approx \tau_0, \tag{2.3}$$

where $\tau_0 = 1/f_0$ is the typical period of the Alfvén waves. Therefore in the solar wind, PDI grows with the timescale of injected wave period. Since the observed wave periods in the solar atmosphere and solar wind ($10^2 - 10^4$ s) are smaller than the Alfvén crossing time from the coronal base to wind acceleration region (10^4 s), PDI is expected to grow inside the wind acceleration region.

Meanwhile, the timescale of Alfvén wave turbulence $\tau_{\rm AWT}$ is defined as the timescale of outward-wave cascading, which is given as

$$\tau_{\rm AWT} \approx \frac{2\lambda_{\rm corr}}{z^-}, \tag{2.4}$$

where $\lambda_{\rm corr}$ is the correlation length and $z^- = v_\perp + B_\perp/\sqrt{4\pi\rho}$ is the downward Elsässer variable. We assume that the correlation length is proportional to the radius of flux tube:

$$\lambda_{\rm corr} = \lambda_{{\rm corr},\odot} \left(B_\odot/B\right)^{1/2}. \tag{2.5}$$

Using this , $\tau_{\rm AWT}$ is evaluated as

$$\tau_{\rm AWT} \approx 10^3 \ {\rm s} \left(\frac{\lambda_{{\rm corr},\odot}}{10^2 \ {\rm km}}\right) \left(\frac{B_\odot}{10^3 \ {\rm G}}\right)^{1/2} \left(\frac{B}{10^{-1} \ {\rm G}}\right)^{-1/2} \left(\frac{z^-}{20 \ {\rm km \ s^{-1}}}\right)^{-1}. \tag{2.6}$$

Comparing Eq. (2.2) and Eq. (2.6), the timescales of the PDI and Alfvén wave turbulence turn out to be comparable.

2.2 Turbulent structure in the solar wind

It has been known since the earliest observation of the solar wind that magnetic field spectrum shows a power-law distribution over a wide range of scales (Coleman, 1968), typically from 10^{-6} Hz (corresponding to the solar rotation) to lower than 10^{-2} Hz. For this reason, the solar wind has been regarded as a plasma turbulence laboratory with several mysterious features. Here we summarize the several open questions on the solar wind turbulence regarding the power spectrum and cross-helicity evolution.

2.2.1 Power spectrum of solar wind turbulence

Two mysteries exist regarding the power spectrum in the solar wind. First, the fast and slow solar winds possess different magnetic power spectrum (Bruno & Carbone, 2013) In the slow solar wind, the magnetic energy shows Kolmogorov-type spectrum, while in the fast solar wind the spectrum is described by a double power law, with lower- and higher-frequency ranges fitted by f^{-1} and $f^{-5/3}$ scalings, respectively. The transition point, or the spectral break point f_b radially evolves as $f_b \propto r^{-1.52}$ (Bruno & Carbone, 2013). The origin of these spectra are still under debate.

The other unsolved problem is the difference between the magnetic and velocity spectrum. The magnetic spectrum follows the Kolmogorov-type spectrum, while the velocity follows the Iroshnikov-Kraichnan-type spectrum (Podesta et al., 2007). To understand the origin of power spectrum, a direct calculation of solar wind turbulence is required.

2.2.2 Cross-helicity evolution in the solar wind

The (normalized) cross helicity σ_c is defined via Elsässer variables $\boldsymbol{z}^{\pm}$ as

$$\sigma_c = \frac{z^{+2} - z^{-2}}{z^{+2} + z^{-2}}, \tag{2.7}$$

which is an ideal invariant in incompressible MHD equations. In the actual solar wind, σ_c is no longer an invariant and evolves in radial direction. Three physical mechanisms are responsible for such radial evolution. First, wave reflection due to the inhomogeneity of the solar wind works to reduce $|\sigma_c|$ (Cranmer & van Ballegooijen, 2005; Verdini & Velli, 2007). Second, when the compressibility is permitted, it also tends to reduce $|\sigma_c|$ possibly by parametric decay instability (Grappin et al., 1993; Del Zanna et al., 2001; Shoda & Yokoyama, 2016). The third mechanism, called dynamical alignment, works in the opposite way. When Alfvén wave(incompressible MHD) turbulence is imbalanced, the system relaxes to $|\sigma_c| = 1$ (Dobrowolny et al., 1980; Stribling & Matthaeus, 1991; Hossain et al., 1995).

The observations of cross helicity in the solar wind shows that it becomes smaller as the radial distance gets larger. An approximate scaling of $e_\pm$ is given as (Bavassano et al., 1982, 2000)

$$e_+ \propto r^{-1.48}, \qquad e_- \propto r^{-0.42}. \tag{2.8}$$

In terms of cross helicity, the observation shows that the cross helicity decreases as r increases. This indicates that the linear reflection and compressible processes work more effectively than dynamical alignment. A linear propagation of Alfvén waves explains this trend (Verdini & Velli, 2007; Cranmer et al., 2017), although we cannot rule out the possibility of parametric decay instability in the distant solar wind (Malara & Velli, 1996; Malara et al., 2000; Del Zanna et al., 2015; Shoda & Yokoyama, 2016).

2.3 Mass-loss rate of solar/stellar wind

2.3.1 On the role of mass-loss rate

A theory of solar wind is often directly applicable to the winds from Sun-like stars. An especially important role of stellar wind is to brake the stellar rotation by extracting angular momentum. Since angular momentum is transported by magnetic field line, such mechanism is called magnetic braking. The time scale of magnetic braking is often comparable to or even smaller than the lifetime of star, and therefore it plays a crucial role in the stellar spin evolution through dynamo-wind interaction (Brun & Browning, 2017).

An analytical studies of angular momentum transport of magnetized stellar wind reveal that the angular momentum loss rate, or torque (τ_w), is expressed as (Weber & Davis, 1967; Sakurai, 1985),

$$\tau_w = \dot{M}_w r_A^2 \omega_*, \tag{2.9}$$

where $\dot{M}_w$ is the mass loss rate of stellar wind, r_A is the Alfvén radius where the radial

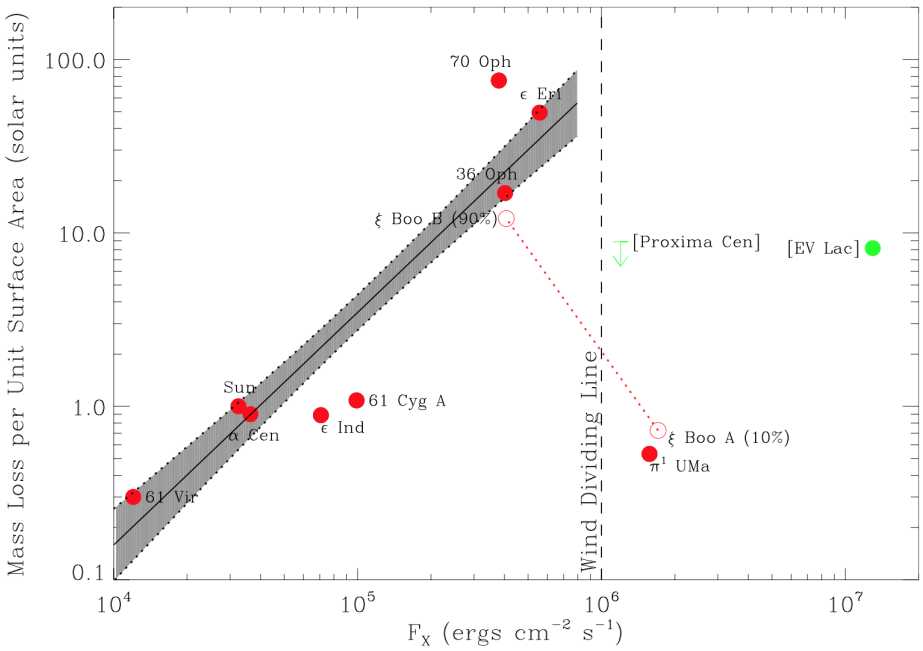

Figure 2.7: Observed mass-loss rate per unit surface area versus X-ray flux. The gray region indicates where the simple scaling law holds with upper limit shown by vertical dashed line so called wind dividing line. Figure reproduced from Wood et al. (2014).

Alfvén speed equals radial wind velocity, and ω_* is the angular frequency of stellar rotation. A number of studies have been dedicated to derive the scaling law of r_A (Matt & Pudritz, 2008; Matt et al., 2012; Réville et al., 2015), which is now formulated as (Réville et al., 2015)

$$r_A/r_* = K_1 \left[\frac{\Phi_{\rm open}}{\dot{M}_w r_*^2 v_{\rm esc} \left(1 + f^2/K_2^2\right)^{1/2}} \right]^m, \quad f = \Omega_* R_*^{3/2} \left(GM_\odot\right)^{-1/2} \tag{2.10}$$

where r_*, ω_* and M_* are the radius, angular frequency of rotation and mass of the star. $\Phi_{\rm open}$ is the amount of open magnetic flux, $\dot{M}_w$ is the mass-loss rate by wind and $v_{\rm esc}$ is the escape velocity. K_1, K_2 and m are dimensionless parameters. Such a physics-based scaling law of r_A is used to model the stellar rotation history (Gallet & Bouvier, 2013, 2015). We need to know the scaling law of $\dot{M}_w$ to derive the angular momentum loss rate because the other parameters are fundamental observables.

Observations of mass-loss rate is quite difficult. The stellar wind mass-loss rate is hardly detectable from direct observation. We instead observe the Lyα line in the termination shock of stellar wind (Wood et al., 2002; Wood, 2004), whose absorption is correlated with the ram pressure of stellar wind. Assuming that the stellar wind velocity is approximately $400\ \mathrm{km\ s^{-1}}$, one can deduce the mass-loss rate. Figure 2.7 shows the mass-loss rate per unit surface area versus X-ray luminosity F_X. Although a correlation between mass-loss rate and F_X is found in a certain range as

$$\dot{M}_w \propto 4\pi r_*^2 F_X^{1.34\pm0.18} \tag{2.11}$$

it fails in the high F_X range beyond the so called wind-dividing line. The positive correlation between mass-loss rate and X-ray flux is not trivial (or contradictory) because the stellar wind blows out from open field regions while the large fraction of X-ray is emitted from closed loops. Although the no theories have ever successfully explain the correlation and wind dividing line, the mass-loss rate is at least strongly affected by the magnetic activity of star.

2.3.2 Theory of mass-loss rate

Suzuki & Inutsuka (2006) conduct a various parameter survey of the solar wind acceleration. One interesting result is that the solar wind velocity does not monotonically increases with the injected power (the right bottom panel), because the solar wind density drastically increases with the wave amplitude and therefore the solar wind becomes more difficult to accelerate. The mass flux (mass-loss rate) is sensitive to the injected wave amplitude (the right middle panel): the mass-loss rate $\dot{M}_w$ is approximately scaled as

$$\dot{M}_w \propto dv_{\perp,0}^4 \quad \left(dv_{\perp,0} \gtrsim 0.5\ \mathrm{km\ s^{-1}}\right). \tag{2.12}$$

For comprehensive parameter survey on Alfvén wave driven solar wind, Cranmer et al. (2007) study Alfvén wave propagation in the solar atmosphere using the equation of

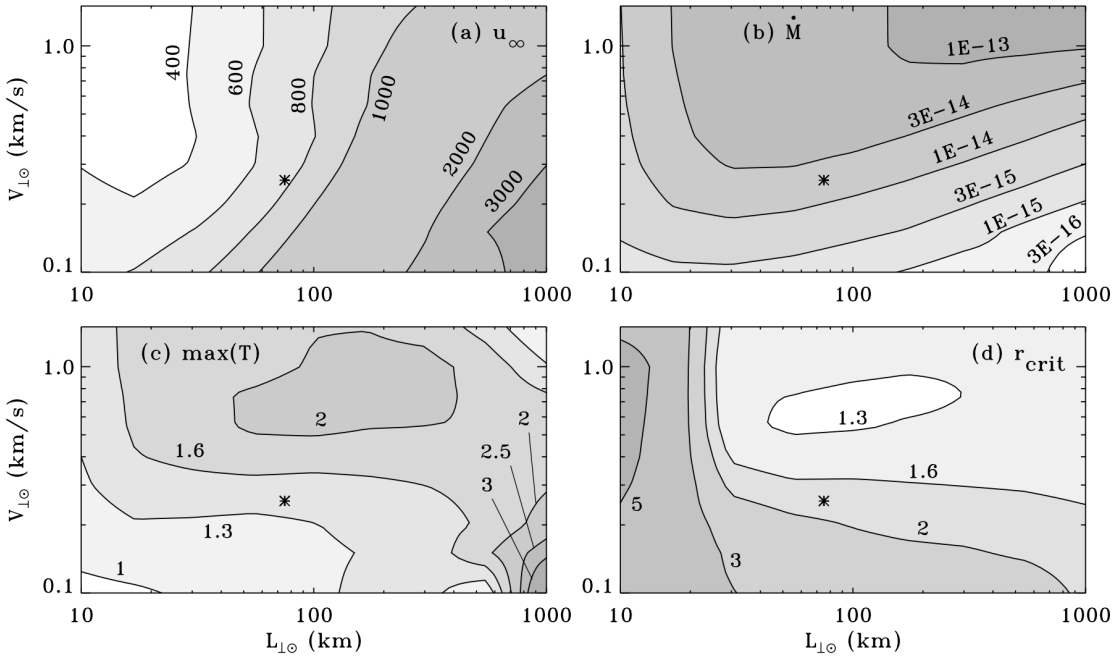

Figure 2.8: Dependence of solar wind parameters on the photospheric transverse velocity $v_{\perp,\odot}$ and perpendicular correlation length $L_{\perp,\odot}$ obtained by Cranmer et al. (2007). (a): termination solar wind velocity u_∞ in unit of $\mathrm{km\ s^{-1}}$, (b): mass-loss rate $\dot{M}$ in unit of $M_\odot\ \mathrm{yr^{-1}}$, (c): maximum temperature $\max(T)$ in unit of 10^6 K, (d): critical point position r_{crit} in unit of $R_\odot$. Figure reproduced from Cranmer et al. (2007).

wave-action conservation with phenomenological turbulent dissipation. The background atmosphere and wind where the Alfvén waves propagate are determined from the energy and momentum balance that takes into account wave heating and acceleration. Figure 2.8 shows the dependence of various solar wind parameters on the photospheric transverse velocity $v_{\perp,\odot}$ and photospheric transverse correlation length $L_{\perp,\odot}$. The termination velocity sensitively depends on the correlation length, while the mass-loss rate is controlled mainly by the transverse velocity (energy injection). This means that the position of heat deposition (that is controlled by the correlation length) determines the solar wind velocity (Leer & Holzer, 1980) while the total energy flux that is injected to the higher atmosphere is a key for mass-loss rate (Withbroe, 1988; Hansteen & Leer, 1995). Cranmer & Saar (2011) extends this work to general cool stars to show a sensitive dependence of mass-loss

rate on the photospheric energy flux.

2.4 Motivation of this thesis

Based on the current understanding by the previous studies shown above, we will mainly address the following three issues regarding fast solar winds: dissipation mechanism of Alfvén waves, turbulent structure and mass-loss rate. As discussed in Section 2.1, the standard model (reflection-driven Alfvén wave turbulence model) turns out to yield insufficient heating rate. In the presence of density fluctuation, the heating rate drastically increases and therefore the standard model revives. In understanding the Alfvén wave dissipation, we need to clarify the origin of such density fluctuation. The parametric decay instability is a promising candidate for the generation of large density perturbation. By taking into account the parametric decay instability, we aim to understand how the solar wind is heated. Section 2.2 summarizes several mysterious behavior of solar wind turbulence. To understand the physics underlying these observations, we investigate, for example, what kind of power spectrum is generated from compressible MHD simulation. The importance of mass-loss rate in the context of stellar physics is stressed in Section 2.3. The scaling law of mass-loss rate is needed to develop a model of angular momentum loss model. We investigate what kind of scaling law is obtained under realistic theoretical modeling.

Chapter 3

1D simulations with phenomenological turbulence model

3.1 Introduction

We report the results of one-dimensional simulations in this Chapter. To consider the effect of turbulence, we phenomenologically model the dynamics perpendicular to the field line. Low numerical cost of 1D simulation allows us to conduct parameter survey, leading to a better understanding of physics.

3.1.1 Toward a unified model of the fast solar wind

As discussed in Chapter 2 the dissipation mechanism of Alfvén waves in the solar wind is yet unclear. In addition to the recent reports that reflection-driven Alfvén wave turbulence scenario does not work (van Ballegooijen & Asgari-Targhi, 2016), what makes the situation controversial is that two different models independently reproduce the fast solar wind consistently with observation. One is the reflection-driven Alfvén wave turbulence model with a phenomenological treatment of turbulence in which Alfvén wave dissipates by turbulence (Cranmer et al., 2007; Verdini et al., 2010; Lionello et al., 2014), and the other is the parametric decay instability model in which Alfvén wave dissipates by conversion to slow-mode waves and shocks (Suzuki & Inutsuka, 2005, 2006). The former and latter

ignore the compressional waves and Alfvén wave turbulence, respectively. The actual solar wind should lie somewhere in-between, and therefore a unified model is required.

For this purpose, we develop a hybrid model that is based on compressible MHD equations and includes phenomenological turbulence model. Based on 1D compressible MHD equations in which the coupling between Alfvén wave compressional waves are automatically solved, we introduce additional terms that correspond to turbulent dissipation. Besides, for comparison with Cranmer et al. (2007) in which a comprehensive parameter survey is conducted based on turbulence heating scenario, we perform simulations with various parameters. Specifically we aim to understand how the mass-loss rate depends on the photospheric parameters.

3.1.2 Explanation of density fluctuation and cross helicity

The density fluctuation possibly plays a non-negligible role in the solar wind energetics. By introducing density fluctuation, due to the enhanced reflection of Alfvén waves, the heating rate of Alfvén wave turbulence becomes sufficiently large (van Ballegooijen & Asgari-Targhi, 2016). In this regard, the density fluctuation is essential, although the origin of it is unknown. Meanwhile, observations of density fluctuation indicate that the magnitude of density fluctuation becomes largest (as large as a few 10% of the mean value) in the wind acceleration region (Miyamoto et al., 2014). Fast mode propagation cannot account for such a large density fluctuation (Cranmer & van Ballegooijen, 2012), and therefore, the large density fluctuation in the wind acceleration region is a mystery. We aim to explain the observational behavior and the underlying physics of density fluctuation based on compressible MHD equations.

The cross helicity evolution is another constraint of theoretical model. Cross helicity is a measure of the imbalance between outward and inward Alfvén waves (see Chapter 2 for detail). Observationally, it is known that the cross helicity of the fast solar wind is large and gradually decreases as radial distance gets larger (Bavassano et al., 1982, 2000). This trend is usually explained as linear propagation of Alfvén waves (Verdini &

Velli, 2007; Verdini et al., 2010). In the presence of large density fluctuation, such an observational behavior becomes difficult to explain, because the large density fluctuation enhances the reflection rate, leading to low cross helicity. A simultaneous explanation of density fluctuation and cross helicity in the solar wind is challenging and is a severe constraint of theoretical model.

3.1.3 Purpose of 1D simulation

Purposes of 1D simulations are as follows. First, we aim to clarify the dominant dissipation mechanism of Alfvén waves in the solar wind. Specifically, we aim to reveal to what extent the fraction of turbulence and shock heatings are. For this purpose, we need to solve the generation of shock waves (parametric decay instability) and Alfvén wave turbulence simultaneously. Second, we investigate how the mass-loss rate of the solar wind is determined. Low numerical cost of 1D simulation enables us to conduct the parameter survey on the mass-loss rate. In addition to these, we aim to explain the observational behavior of the density fluctuation and cross helicity in the solar wind. The observed density fluctuation becomes largest in the wind acceleration region, the underlying physics of which is yet unclear. In the presence of large density fluctuation, the high cross helicity in the solar wind becomes difficult to explain, because the density fluctuation introduces additional reflection of Alfvén waves.

3.2 Method

To take into account the turbulent heating in 1D simulations, we utilize the phenomenological model of turbulence. Additional terms corresponding to turbulent dissipation are introduced to the usual 1D compressible MHD equations. Since this procedure is not trivial, we first explain how to implement the turbulence model, beginning with a review of model itself. The basic equations and numerical settings are shown later.

3.2.1 Phenomenological turbulence model

To solve the parametric decay instability and Alfvén wave turbulence simultaneously, we introduce additional source terms corresponding to turbulent dissipation into 1D compressible MHD equations. By doing so, the wave propagation (including) reflection and parametric decay instability are solved in the framework of 1D compressible MHD equations, while turbulent dissipation is solved by the additional terms. We discuss the implementation here.

Let us first review the phenomenological turbulence model in reduced MHD equations. The original reduced MHD equations that describe the Alfvén wave propagation in the solar wind are (Zhou & Matthaeus, 1990; Verdini & Velli, 2007)

$$\begin{aligned}&\frac{\partial}{\partial t}\boldsymbol{z}^{\pm} + (\boldsymbol{u} \pm \boldsymbol{v}_A)\cdot\nabla\boldsymbol{z}^{\pm} \\ &- \boldsymbol{z}^{\pm}(\boldsymbol{u} \mp \boldsymbol{v}_A)\cdot\nabla \ln \rho^{1/4} + \boldsymbol{z}^{\mp}(\boldsymbol{u} \mp \boldsymbol{v}_A)\cdot\nabla \ln\left(\rho^{1/4}A^{1/2}\right) = -\left(\boldsymbol{z}^{\mp}\cdot\nabla\right)\boldsymbol{z}^{\pm}, \quad (3.1)\end{aligned}$$

where $\boldsymbol{z}^{\pm} = \boldsymbol{v}_{\perp} \mp \boldsymbol{B}_{\perp}/\sqrt{4\pi\rho}$ are Elsässer variables. $\boldsymbol{u}$ and $\boldsymbol{v}_A$ denote the mean and Alfvén velocities, respectively. A denotes the cross section of flux tube that satisfies $AB_r = \mathrm{const.}$. The third and fourth terms in the left hand side of Eq. (3.1) correspond to the WKB (amplification) and reflection terms, respectively (Heinemann & Olbert, 1980). The right hand side represents the nonlinear interaction between forward ($\boldsymbol{z}^{+}$) and backward ($\boldsymbol{z}^{-}$) Alfvén waves. The widely-used phenomenological model simply approximates the right hand side as (Hossain et al., 1995; Matthaeus et al., 1999; Dmitruk et al., 2002; van Ballegooijen & Asgari-Targhi, 2017)

$$\left(\boldsymbol{z}^{\mp}\cdot\nabla\right)\boldsymbol{z}^{\pm} \approx c_d\frac{z^{\mp}_{\mathrm{rms}}}{2\lambda}\boldsymbol{z}^{\pm}, \quad (3.2)$$

where $z^{\mp}_{\mathrm{rms}}$ is the rms value of $\boldsymbol{z}^{\mp}$ and λ is the horizontal correlation length. This approx-

imation yields a quasi-linear equations for $\boldsymbol{z}_{\pm}$:

$$\frac{\partial}{\partial t}\boldsymbol{z}^{\pm} + (\boldsymbol{u} \pm \boldsymbol{v}_A)\cdot\nabla\boldsymbol{z}^{\pm} - \boldsymbol{z}^{\pm}(\boldsymbol{u} \mp \boldsymbol{v}_A)\cdot\nabla \ln \rho^{1/4} + \boldsymbol{z}^{\mp}(\boldsymbol{u} \mp \boldsymbol{v}_A)\cdot\nabla \ln\left(\rho^{1/4}A^{1/2}\right) = -c_d\frac{z^{\mp}_{\rm rms}}{2\lambda}\boldsymbol{z}^{\pm}. \tag{3.3}$$

The choice of coefficient c_d is not trivial. Several studies simply assume $c_d = 1$, while a recent 3D direct numerical simulation indicates that $c_d = 0.1$ is possibly more appropriate (van Ballegooijen & Asgari-Targhi, 2017). For this reason, we use $c_d = 0.1$ in this study.

Using the phenomenological approximation Eq. (3.2), we aim to derive the hybrid model that incorporates parametric decay instability and Alfvén wave turbulence. The equation of motion in the transverse velocity and the induction equation of the transverse magnetic field are expressed in the one-dimensional coordinate co-expanding with the background magnetic field as,

$$\rho\frac{d}{dt}\left(\sqrt{A}\boldsymbol{v}_{\perp}\right) = \frac{B_r}{4\pi}\frac{\partial}{\partial r}\left(\sqrt{A}\boldsymbol{B}_{\perp}\right), \tag{3.4}$$

$$\frac{\partial}{\partial t}\boldsymbol{B}_{\perp} = \frac{1}{\sqrt{A}}\frac{\partial}{\partial r}\left[\sqrt{A}\left(\boldsymbol{v}_{\perp}B_r - v_r\boldsymbol{B}_{\perp}\right)\right], \tag{3.5}$$

where A denotes the cross section of the flux tube. Using the mass conservation and the solenoidal condition,

$$\frac{d}{dt}\rho + \frac{\rho}{A}\frac{\partial}{\partial r}\left(Av_r\right) = 0, \qquad \frac{\partial}{\partial r}\left(AB_r\right) = 0, \tag{3.6}$$

we obtain the conservation laws of $\rho\boldsymbol{v}_{\perp}$ and $\boldsymbol{B}_{\perp}$ as

$$\frac{\partial}{\partial t}\left(\rho\boldsymbol{v}_{\perp}A^{3/2}\right) + \left[\left(\rho v_r\boldsymbol{v}_{\perp} - \frac{1}{4\pi}B_r\boldsymbol{B}_{\perp}\right)A^{3/2}\right] = 0, \tag{3.7}$$

$$\frac{\partial}{\partial t}\left(\boldsymbol{B}_{\perp}A^{1/2}\right) + \frac{\partial}{\partial r}\left[\left(v_r\boldsymbol{B}_{\perp} - \boldsymbol{v}_{\perp}B_r\right)A^{1/2}\right] = 0. \tag{3.8}$$

These are a part of usual one-dimensional compressible MHD equations. To incorporate the phenomenological dissipation of Alfvén wave turbulence, we add source terms in the

right hand sides as

$$\frac{\partial}{\partial t}\left(\rho \boldsymbol{v}_\perp A^{3/2}\right) + \left[\left(\rho v_r \boldsymbol{v}_\perp - \frac{1}{4\pi} B_r \boldsymbol{B}_\perp\right) A^{3/2}\right] = -\hat{\boldsymbol{\eta}}_1 \cdot \rho \boldsymbol{v}_\perp A^{3/2} - \hat{\boldsymbol{\eta}}_2 \cdot \sqrt{\frac{\rho}{4\pi}} \boldsymbol{B}_\perp A^{3/2}, \tag{3.9}$$

$$\frac{\partial}{\partial t}\left(\boldsymbol{B}_\perp A^{1/2}\right) + \frac{\partial}{\partial r}\left[\left(v_r \boldsymbol{B}_\perp - \boldsymbol{v}_\perp B_r\right) A^{1/2}\right] = -\hat{\boldsymbol{\eta}}_1 \cdot \boldsymbol{B}_\perp A^{1/2} - \hat{\boldsymbol{\eta}}_2 \cdot \sqrt{4\pi\rho} \boldsymbol{v}_\perp A^{1/2}, \tag{3.10}$$

where $\hat{\boldsymbol{\eta}}_1$ and $\hat{\boldsymbol{\eta}}_2$ are diagonal matrices:

$$\hat{\boldsymbol{\eta}}_1 = \begin{pmatrix} \frac{c_d}{4\lambda}\left(|z_x^+| + |z_x^-|\right) & 0 \\ 0 & \frac{c_d}{4\lambda}\left(|z_y^+| + |z_y^-|\right) \end{pmatrix}, \tag{3.11}$$

$$\hat{\boldsymbol{\eta}}_2 = \begin{pmatrix} \frac{c_d}{4\lambda}\left(|z_x^+| - |z_x^-|\right) & 0 \\ 0 & \frac{c_d}{4\lambda}\left(|z_y^+| - |z_y^-|\right) \end{pmatrix}, \tag{3.12}$$

where λ is the correlation length, $\boldsymbol{z}^\pm = \boldsymbol{v}_\perp \mp \boldsymbol{B}_\perp/\sqrt{4\pi\rho}$ are Elsässer variables, and x, y denote the perpendicular components. The physical meanings of $\hat{\boldsymbol{\eta}}_1$ and $\hat{\boldsymbol{\eta}}_2$ are turbulent dissipation and dynamical alignment, respectively. Note that $\hat{\boldsymbol{\eta}}_2$ arises only when the turbulence is imbalanced ($|z^+| \neq |z^-|$) and the dynamical alignment proceeeds (Dobrowolny et al., 1980; Stribling & Matthaeus, 1991; Hossain et al., 1995; Beresnyak & Lazarian, 2008; Chandran, 2008).

Let us show that Eq. (3.9) and (3.10) are consistent with the approximated reduced MHD equation Eq. (3.3). To rule out the compressible waves that do not appear in reduced MHD equations, we assume $\partial\rho/\partial t = 0$ and $\partial v_r/\partial t = 0$. This is not to assume the incompressibility; we still take into account the wind acceleration that comes from the

compressibility. Under this assumption, Eq.s (3.9) and (3.10) are written as

$$\frac{\partial}{\partial t}\boldsymbol{v}_\perp + u\frac{\partial}{\partial r}\boldsymbol{v}_\perp - v_A\frac{\partial}{\partial r}\boldsymbol{b}_\perp + u\boldsymbol{v}_\perp\frac{\partial}{\partial r}\ln\left(A^{1/2}\right) - v_A\boldsymbol{b}_\perp\frac{\partial}{\partial r}\ln\left(\rho^{1/2}A^{1/2}\right) = -\hat{\boldsymbol{\eta}}_1\cdot\boldsymbol{v}_\perp - \hat{\boldsymbol{\eta}}_2\cdot\boldsymbol{b}_\perp, \tag{3.13}$$

$$\frac{\partial}{\partial t}\boldsymbol{b}_\perp + u\frac{\partial}{\partial r}\boldsymbol{b}_\perp - v_A\frac{\partial}{\partial r}\boldsymbol{v}_\perp + v_A\boldsymbol{v}_\perp\frac{\partial}{\partial r}\ln\left(A^{1/2}\right) - u\boldsymbol{b}_\perp\frac{\partial}{\partial r}\ln\left(\rho^{1/2}A^{1/2}\right) = -\hat{\boldsymbol{\eta}}_1\cdot\boldsymbol{b}_\perp - \hat{\boldsymbol{\eta}}_2\cdot\boldsymbol{v}_\perp, \tag{3.14}$$

where we use the notation $u = v_r$ and $v_A = B_r/\sqrt{4\pi\rho}$. In terms of Elsässer variables these equations are written as

$$\begin{aligned}&\frac{\partial}{\partial t}\boldsymbol{z}^\pm + (u \pm v_A)\frac{\partial}{\partial r}\boldsymbol{z}^\pm \\ &- \boldsymbol{z}^\pm(u \mp v_A)\frac{\partial}{\partial r}\ln\left(\rho^{1/4}\right) + \boldsymbol{z}^\mp(u \mp v_A)\frac{\partial}{\partial r}\ln\left(\rho^{1/4}A^{1/2}\right) = -\hat{\boldsymbol{\eta}}^\mp\cdot\boldsymbol{z}^\pm,\end{aligned} \tag{3.15}$$

where

$$\hat{\boldsymbol{\eta}}^\mp = \hat{\boldsymbol{\eta}}_1 \mp \hat{\boldsymbol{\eta}}_2 = \begin{pmatrix} \frac{c_d}{2\lambda}|z_x^\mp| & 0 \\ 0 & \frac{c_d}{2\lambda}|z_y^\mp| \end{pmatrix}. \tag{3.16}$$

Eq. (3.15) is consistent with Eq. (3.3).

3.2.2 Basic equations and setting

The basic equations are 1.5D (one-dimensional, three-components) MHD equations in a expanding flux tube. We consider the variation along the flux tube and at the same time

we take into account the super-radial expansion.

$$\frac{\partial}{\partial t}\left(\rho r^2 f\right) + \frac{\partial}{\partial r}\left(\rho v_r r^2 f\right) = 0, \tag{3.17}$$

$$\frac{\partial}{\partial t}\left(\rho v_r r^2 f\right) + \frac{\partial}{\partial r}\left[\left(\rho {v_r}^2 + p + \frac{{\boldsymbol{B}_\perp}^2}{8\pi}\right) r^2 f\right] = \left(p + \frac{\rho {\boldsymbol{v}_\perp}^2}{2}\right)\frac{d}{dr}\left(r^2 f\right) - \rho g r^2 f, \tag{3.18}$$

$$\frac{\partial}{\partial t}\left(\rho \boldsymbol{v}_\perp r^3 f^{3/2}\right) + \frac{\partial}{\partial r}\left[\left(\rho v_r \boldsymbol{v}_\perp - \frac{B_r \boldsymbol{B}_\perp}{4\pi}\right) r^3 f^{3/2}\right] = -\hat{\boldsymbol{\eta}}_1 \cdot \rho \boldsymbol{v}_\perp r^3 f^{3/2} - \hat{\boldsymbol{\eta}}_2 \cdot \sqrt{\frac{\rho}{4\pi}} \boldsymbol{B}_\perp r^3 f^{3/2}, \tag{3.19}$$

$$\frac{\partial}{\partial t}\left(r\sqrt{f}\boldsymbol{B}_\perp\right) + \frac{\partial}{\partial r}\left[\left(\boldsymbol{B}_\perp v_r - B_r \boldsymbol{v}_\perp\right) r\sqrt{f}\right] = -\hat{\boldsymbol{\eta}}_1 \cdot \boldsymbol{B}_\perp r\sqrt{f} - \hat{\boldsymbol{\eta}}_2 \cdot \sqrt{4\pi\rho}\boldsymbol{v}_\perp r\sqrt{f}, \tag{3.20}$$

$$\frac{d}{dr}\left(r^2 f B_r\right) = 0, \tag{3.21}$$

$$\frac{\partial}{\partial t}\left[\left(e + \frac{1}{2}\rho \boldsymbol{v}^2 + \frac{\boldsymbol{B}^2}{8\pi}\right) r^2 f\right] + \frac{\partial}{\partial r}\left[\left(e + p + \frac{1}{2}\rho \boldsymbol{v}^2 + \frac{{\boldsymbol{B}_\perp}^2}{8\pi}\right) v_r r^2 f - B_r \frac{\boldsymbol{B}_\perp \cdot \boldsymbol{v}_\perp}{4\pi} r^2 f\right]$$

$$= r^2 f\left(-\rho g v_r + Q_{\mathrm{rad}} + Q_{\mathrm{cnd}}\right), \tag{3.22}$$

$$e = \frac{p}{\gamma - 1}, \quad p = \frac{\rho k_B T}{\mu m_H}., \quad g = \frac{G M_\odot}{r^2}, \tag{3.23}$$

where G is the gravitational constant and $M_\odot$ is the solar mass. f is the expansion factor (Schatten et al., 1969; Wang & Sheeley, 1990; Arge & Pizzo, 2000; Réville & Brun, 2017) of the flux tube in consideration. μ is the mean molecular mass in unit of m_H (hydrogen mass); if the plasma is composed of hydrogen, $\mu = 0.5$ for the fully-ionized case and $\mu = 1$ for the rarely-ionized case.

In the following sections, as ancillary variables, we use h and $\boldsymbol{z}^\pm$. h is used to denote the altitude from the solar surface:

$$h = r - R_\odot, \tag{3.24}$$

where $R_\odot$ is the solar radius. h is mainly used to express the location in the chromosphere,

	case I	case II
bottom boundary	photosphere	coronal base
top boundary	0.5 au	1.0 au
thermal conduction	Spitzer-Härm	Spitzer-Härm + free-streaming
radiative cooling	Newtonian + optically thin	None
fixed parameter	wave frequency	correlation length & amplitude
free parameter	correlation length & amplitude	wave frequecny

Table 3.1: Summary of numerical settings of case I and case II. In case I, since we solve the radiation-dominated chromosphere, the radiation is explicitly solved. While in case II, radiation is excluded because the chromosphere is out of the simulation domain. Instead, we incorporate the free-streaming heat flux that works in the distant solar wind.

the typical thickness is only a few $10^{-3}R_\odot$. $\boldsymbol{z}^\pm$ are the Elsässer variables (Elsässer, 1950):

$$\boldsymbol{z}^\pm = \boldsymbol{v}_\perp \mp \boldsymbol{B}_\perp/\sqrt{4\pi\rho}. \tag{3.25}$$

3.2.3 Simulation setting

Using the same basic equations, we perform two cases of simulations which we hereafter call case I and case II. We briefly summarize the numerical settings of the two cases in Table 3.1. The case I is to survey the dependence on the correlation length and wave injection amplitude, while the case II focuses on the dependence on frequency.

We apply free boundary condition at the top for every variable:

$$\left.\frac{\partial}{\partial r}X\right|_{\rm top} = 0 \ \ (\text{case I \& II}), \tag{3.26}$$

where X stands for the primitive variable such as ρ, p, etc. The choice of the top boundary

condition does not affect the calculation because the top boundary always lies in the supersonic and super-Alfvénic region where no fluctuations can propagate backward. This is why we need not use the transmitting boundary condition (Thompson, 1987; Del Zanna et al., 2001; Suzuki & Inutsuka, 2006) for the top boundary. Note that the transmitting boundary possibly yield a better result when we simulate the dynamical acceleration of the solar wind in which the radial velocity of the top boundary is subsonic in the initial phase.

Since the bottom boundary locates at different heights, the imposed values for the bottom boundary are different. The bottom boundary locates at the photosphere ($h_{\rm bottom} = 0\ {\rm Mm}$) in case I, while it locates at the coronal base ($h_{\rm bottom} = 10\ {\rm Mm}$) in case II. The fixed boundary conditions are used to the density, temperature, and radial magnetic field as

$$\rho_{\rm bottom} = 1.0 \times 10^{-7}\ {\rm g\ cm^{-3}}\ ({\rm case\ I}), \quad 8.5 \times 10^{-16}\ {\rm g\ cm^{-3}}\ ({\rm case\ II}), \tag{3.27}$$

$$T_{\rm bottom} = 6.0 \times 10^{3}\ {\rm K}\ ({\rm case\ I}), \quad 4.0 \times 10^{5}\ {\rm K}\ ({\rm case\ II}), \tag{3.28}$$

$$B_{r,{\rm bottom}} = 1.0 \times 10^{3}\ {\rm G}\ ({\rm case\ I}), \quad 1.0 \times 10^{1}\ {\rm G}\ ({\rm case\ II}). \tag{3.29}$$

The free boundary conditions are applied to the radial velocity v_r and inward Elsässer variable:

$$\left.\frac{\partial}{\partial r} v_r\right|_{\rm bottom} = 0, \qquad \left.\frac{\partial}{\partial r} \boldsymbol{z}^-\right|_{\rm bottom} = 0\ \ ({\rm case\ I\ \&\ II}). \tag{3.30}$$

The boundary condition of upward Elsässer variables are given with broadband spectrum:

$$\boldsymbol{z}^+ \propto \int_{2\pi f_{\rm min}}^{2\pi f_{\rm max}} d\omega \boldsymbol{P}(\omega) \sin\left(\omega t + \boldsymbol{\phi}_{\rm rand}(\omega)\right), \tag{3.31}$$

where $\boldsymbol{P}$ is the power spectrum and $\boldsymbol{\phi}_{\rm rand}$ is a random phase function of ω. In case I, the

spectrum is fixed to $\boldsymbol{P}(\omega) \propto \omega^{-1}$ and

$$f_{\min} = 10^{-3}\ \mathrm{Hz}, \qquad f_{\max} = 10^{-2}\ \mathrm{Hz}. \tag{3.32}$$

The root-mean-square amplitude of $\boldsymbol{z}^+$ is set to $2dv^+$, where dv^+ is the velocity amplitude of outward Alfvén-wave and is a free parameter in case I. The power spectrum and amplitude in case II is shown in Section 3.4.

The radial profiles of the expansion factor are given in each case as follows. In case I, $f(r)$ is given as

$$f(r) \propto \frac{f_{\max,1} \exp\left[(r - r_1)/\sigma_1\right] + f_1}{\exp\left[(r - r_1)/\sigma_1\right] + 1} \cdot \frac{f_{\max,2} \exp\left[(r - r_2)/\sigma_2\right] + f_2}{\exp\left[(r - r_2)/\sigma_2\right] + 1} \tag{3.33}$$

where

$$f_n = 1 - f_{\max,n} \exp\left[(R_\odot - r_n)/\sigma_n\right], \tag{3.34}$$

$$f_{\max,1} = 120, \quad f_{\max,2} = 4, \tag{3.35}$$

$$r_1 - R_\odot = 1\ \mathrm{Mm}, \quad r_2 - R_\odot = 200\ \mathrm{Mm}, \tag{3.36}$$

$$\sigma_1 = 0.25\ \mathrm{Mm}, \quad \sigma_2 = 350\ \mathrm{Mm}. \tag{3.37}$$

Note that the the first expansion occurs in the chromosphere and the second in the corona. In case II, because the chromosphere is not solved, $f(r)$ is given in a simpler way:

$$f(r) \propto \frac{f_{\max,1} \exp\left[(r - r_1)/\sigma_1\right] + f_1}{\exp\left[(r - r_1)/\sigma_1\right] + 1}, \tag{3.38}$$

where

$$f_1 = 1 - f_{\max,1} \exp\left[(R_\odot - r_1)/\sigma_1\right], \quad f_{\max,1} = 10, \quad r_1 = 1.3R_\odot, \quad \sigma_1 = 0.5R_\odot \tag{3.39}$$

Once $f(r)$ is given, the correlation length λ is calculated under the assumption that

the correlation length scales with the radius of flux tube:

$$\lambda = \lambda_\odot \sqrt{\frac{r^2 f}{R_\odot^2 f_\odot}}. \tag{3.40}$$

In case I, to exclude the turbulent dissipation in the chromosphere, we modify the correlation length as

$$\lambda = \lambda_\odot \sqrt{\frac{r^2 f}{R_\odot^2 f_\odot}} \max\left(1, \frac{\rho}{10^{-16}\ \mathrm{g\ cm^{-3}}}\right). \tag{3.41}$$

Conductive heating $Q_{\rm cnd}$ is expressed in terms of radial conductive flux $q_{\rm cnd}$ as

$$Q_{\rm cnd} = -\frac{1}{r^2 f}\frac{\partial}{\partial r}\left(q_{\rm cnd} r^2 f\right). \tag{3.42}$$

Bearing in mind that the Spitzer-Härm type flux overestimates the heat flux in the solar wind near 1 au, we employ two different fluxes: the Spitzer-Härm flux ($q_{\rm SH}$) and free-streaming flux ($q_{\rm FS}$) given as

$$q_{\rm SH} = -\kappa_0 T^{5/2}\frac{\partial}{\partial r}T, \qquad q_{\rm FS} = \frac{3}{4}\alpha p v_r, \tag{3.43}$$

where $\kappa_0 \approx 10^{-6}$ in cgs-Gaussian unit, and α is a free parameter of oder unity. The choice of α is not trivial. $\alpha = 4$ is often used in the theoretical models (Hollweg, 1986; van Ballegooijen & Asgari-Targhi, 2016), while $\alpha = 1.05$ is the best choice to explain the observed temperature (Cranmer et al., 2009). Here we use $\alpha = 2$ as an intermediate value.

We use different conductive fluxes for case I and case II. For case I, we simply impose Spitzer-Härm type conductive flux $q_{\rm SH}$ with quenching in the distant solar wind as

$$q_{\rm cnd} = q_{\rm SH}\ \min\left(1, \frac{\rho}{10^{-22}\ \mathrm{g\ cm^{-3}}}\right), \tag{3.44}$$

while in case II, we applied a bridging-law between $q_{\rm SH}$ and $q_{\rm FS}$ as

$$q_{\rm cnd} = \xi_{\rm cnd} q_{\rm SH} + (1 - \xi_{\rm cnd})\, q_{\rm FS}, \quad \xi_{\rm cnd} = \min\left(1, \frac{\rho}{10^{-21}\ {\rm g\ cm^{-3}}}\right). \tag{3.45}$$

In case I, we use a non uniform radial mesh that expands in r. This is due to the large gap of spatial scales of Alfvén wave between chromosphere and corona. In case II, we apply uniform mesh because the typical wavelength does not drastically vary in radial distance.

3.3 Result: Case I

3.3.1 Quasi-steady states with various correlation lengths

Figure 3.1 shows the snapshots of primitive variables (density, temperature, radial velocity, transverse velocity) in the quasi-steady states with $dv^+ = 0.5\,{\rm km\,s^{-1}}$. Four lines correspond to different photospheric correlation lengths: $\lambda_0 = 10$ km (red), $\lambda_0 = 10^2$ km (orange), $\lambda_0 = 10^3$ km (green), $\lambda_0 = 10^4$ km (blue). We find in every case the formation of cool lower atmosphere (chromosphere) and hot higher atmosphere (corona) separated by a sharp boundary (transition region). There is no difference in the four lines in the chromosphere because we switch off the turbulent dissipation in the lower atmosphere.

The corona and solar wind show several differences. When the correlation length becomes smaller (as the color of line approaches red), the coronal temperature becomes larger and the solar wind becomes heavier and slower. This indicates that the subsonic corona is heated preferentially by turbulent dissipation, and as a result of enhanced heating with smaller correlation length, the solar wind becomes slower because the energy is injected more to the lower atmosphere (Leer & Holzer, 1980; Hansteen & Velli, 2012). When the correlation length is large, large fluctuations appear in the density and radial velocity. This indicates that the compressible waves are more likely to be generated for larger correlation length. Considering the fact that the growth rate of PDI is larger when

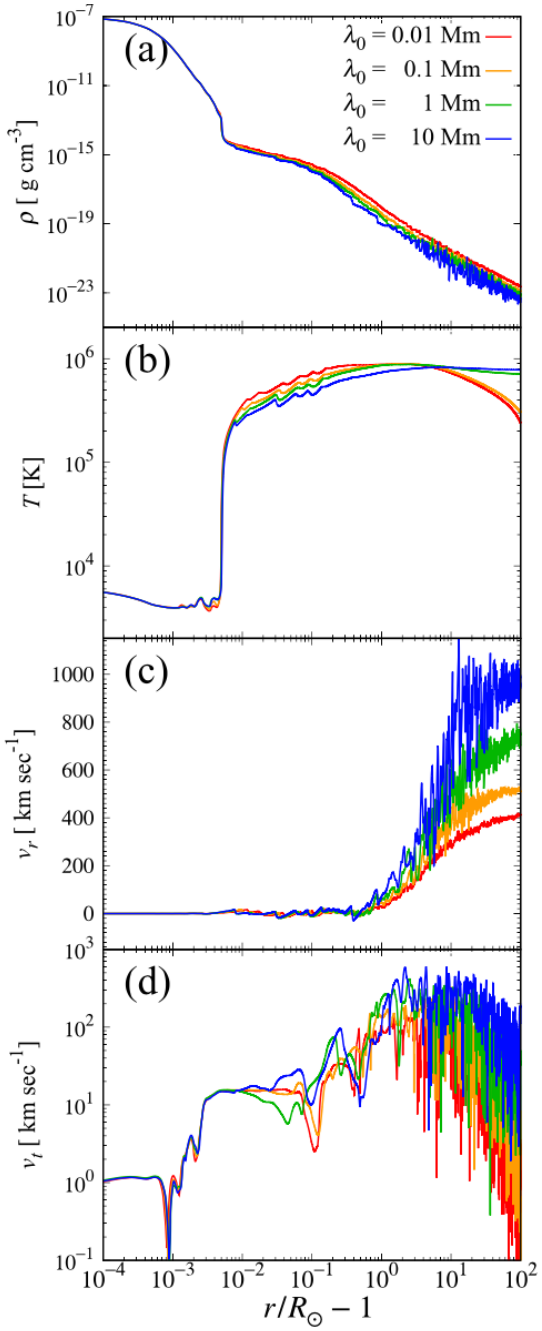

Figure 3.1: Quasi-steady states with fixed wave injection $dv^+ = 0.5\,\mathrm{km\,s^{-1}}$ and various correlation lengths. Red, orange, green, and blue lines correspond to photospheric correlation length of $\lambda_0 = 10\,\mathrm{km}$, $\lambda_0 = 10^2\,\mathrm{km}$, $\lambda_0 = 10^3\,\mathrm{km}$, $\lambda_0 = 10^4\,\mathrm{km}$, respectively. Each panel shows in the descending order the radial profile of density, temperature, radial velocity, and transverse velocity, respectively. Figure reproduced from Shoda et al. (2018a).

the plasma beta is smaller, the large density fluctuation is naturally interpreted as faster growth of PDI because of the smaller solar wind density and smaller plasma beta.

3.3.2 Density fluctuation and cross helicity

To see the clearer dependences on correlation length, we calculate the time-averaged fractional density fluctuation n and the normalized cross helicity σ_c. n indicates the amplitude of compressible waves while σ_c represents the population ratio between outgoing and reflected Alfvén waves. The time-averaged fractional density fluctuation is calculated as

$$n = \delta\rho/\langle\rho\rangle, \quad \delta\rho = \sqrt{\langle(\rho - \langle\rho\rangle)^2\rangle} \tag{3.46}$$

where $\langle X\rangle$ represents the time-average of X:

$$\langle X\rangle = \frac{1}{\tau_{\rm ave}}\int_{t_0}^{t_0+\tau_{\rm ave}} dtX, \tag{3.47}$$

where t_0 is when the system reaches the quasi-steady state and $\tau_{\rm ave} = 1000\,{\rm min}$. The averaged cross helicity σ_c is defined as

$$\sigma_c = \frac{z^+_{\rm rms} - z^-_{\rm rms}}{z^+_{\rm rms} + z^-_{\rm rms}}, \tag{3.48}$$

where

$$z^\pm_{\rm rms} = \sqrt{\langle \boldsymbol{z}^{\pm 2}\rangle}. \tag{3.49}$$

Figure 3.2 shows the radial profile of n (top) and σ_c (bottom) with various correlation lengths. We use the same color of line as Figure 3.1 to stand for the corresponding correlation length. The black circles that indicate the observational values by Miyamoto et al. (2014) show the same trend with the theoretical values. The peak of the density fluctuation in $10^{-3} \lesssim r/R_\odot - 1 \lesssim 10^{-2}$ comes from the steepening of slow-mode waves in the

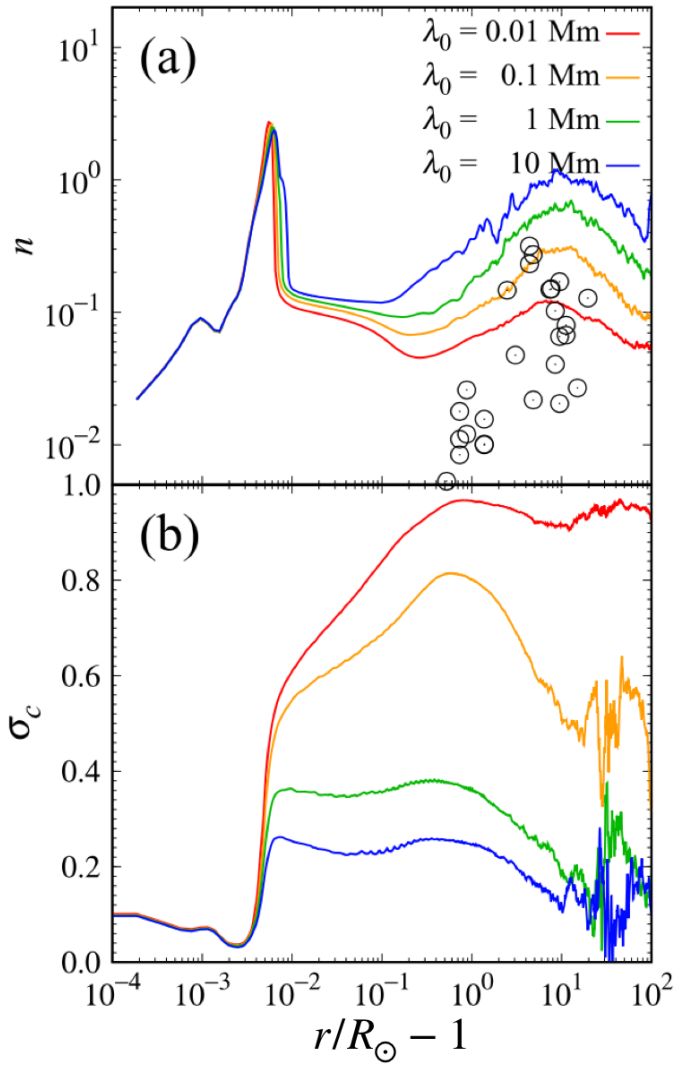

Figure 3.2: Radial profile of the time-averaged fractional density fluctuation n (top) and the normalized cross helicity σ_c (bottom). Red, orange, green, and blue lines correspond to photospheric correlation length of $\lambda_0 = 10\,\mathrm{km}$, $\lambda_0 = 10^2\,\mathrm{km}$, $\lambda_0 = 10^3\,\mathrm{km}$, $\lambda_0 = 10^4\,\mathrm{km}$, respectively. Black circles in the top panel indicate the observation by Miyamoto et al. (2014). Figure reproduced from Shoda et al. (2018a).

chromosphere. Another peak around $r/R_\odot \approx 10$ is positively correlated with correlation length. Bearing in mind that the density fluctuation in the wind acceleration region is generated by parametric decay instability, this result indicates that the correlation length of turbulence controls the saturation phase. In the bottom panel, the cross helicity shows monochromatic dependence on correlation length. Specifically when $\lambda_0 = 10^{-2}\,\mathrm{Mm}$, the

cross helicity in the solar wind is almost unit because of the dynamical alignment effect.

3.3.3 Heating mechanism

We calculate the heating rate via the following analysis. The internal energy equation is written in the following manner (Cranmer et al., 2007):

$$\frac{\partial e}{\partial t} + v_r \frac{\partial e}{\partial r} + \frac{e+p}{r^2 f}\frac{\partial}{\partial r}\left(v_r r^2 f\right) = Q_{\rm rad} + Q_{\rm cnd} + Q_{\rm heat}, \tag{3.50}$$

where $Q_{\rm heat}$ denotes the heat deposition by wave. In a quasi-steady state, by averaging the above equation in time we obtain

$$\langle Q_{\rm heat}\rangle = \langle v_r \frac{\partial e}{\partial r}\rangle + \langle \frac{e+p}{r^2 f}\frac{\partial}{\partial r}\left(v_r r^2 f\right)\rangle - \langle Q_{\rm rad}\rangle - \langle Q_{\rm cnd}\rangle. \tag{3.51}$$

Note that $\langle X\rangle$ represents the time averaged value of X (see Eq. (3.47)) and therefore

$$\langle \frac{\partial e}{\partial t}\rangle = 0. \tag{3.52}$$

The total heating rate $\langle Q_{\rm heat}\rangle$ is calculated in this manner. Meanwhile, the turbulent heating rate is calculated as (Cranmer et al., 2007; Verdini & Velli, 2007)

$$Q_{\rm turb} = \rho \sum_{i=x,y} c_d \frac{|z_i^+|z_i^{-2} + |z_i^-|z_i^{+2}}{4\lambda}. \tag{3.53}$$

Figure 3.3 shows the radial profiles of $\langle Q_{\rm heat}\rangle/\langle\rho\rangle$ (blue lines) and $\langle Q_{\rm turb}\rangle/\langle\rho\rangle$ (red lines) for three different λ_0 values. The left, middle, and right panels correspond to $\lambda_0 = 0.1\,{\rm Mm}$, $\lambda_0 = 1\,{\rm Mm}$, and $\lambda_0 = 10\,{\rm Mm}$, respectively. Since waves dissipate only by shock and turbulence, the gap between blue and red lines corresponds to the heating by shock wave. Figure 3.3 shows that the correlation length strongly affects the solar wind heating mechanism; when $\lambda_0 = 0.1\,{\rm Mm}$ the solar wind is heated by the turbulence, while the shock heating becomes dominant when $\lambda_0 = 10\,{\rm Mm}$. Interestingly, although

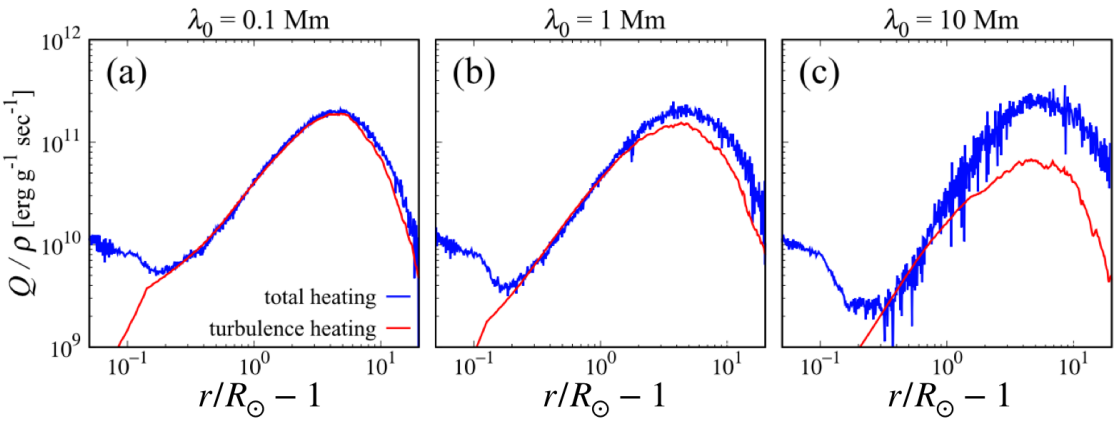

Figure 3.3: Plasma heating rate per particle Q/ρ for three different correlation lengths. Left, middle, and right panels correspond to $\lambda_0 = 0.1\,\mathrm{Mm}$, $\lambda_0 = 1\,\mathrm{Mm}$, and $\lambda_0 = 10\,\mathrm{Mm}$, respectively. The blue lines show the total heating rate that is calculated from the energy equation, while the red lines denote the turbulence heating rate given by the analytical expression. Figure reproduced from Shoda et al. (2018a).

the profile of $\langle Q_{\rm turb}\rangle/\langle\rho\rangle$ drastically changes with λ_0, the total heating rate is almost invariant.

Several noticeable features turns out from the profiles of $\langle Q_{\rm heat}\rangle/\langle\rho\rangle$ and $\langle Q_{\rm turb}\rangle/\langle\rho\rangle$. First the coronal base (just above the transition region) where $r/R_\odot - 1 \lesssim 0.1$ is heated preferentially by shock waves. This probably comes from a technical reason that we cut off the turbulence heating in the coronal base, but not unrealistic because both observation (Tian et al., 2014; Kanoh et al., 2016) and numerical simulation (Kudoh & Shibata, 1999; Matsumoto & Shibata, 2010; Iijima & Yokoyama, 2015) show the existence of chromospheric shock waves. In the subsonic corona where $0.1 \lesssim r/R_\odot - 1 \lesssim 1$, regardless of the correlation length, turbulence is the dominant heating mechanism. This is why the fast solar wind is generated when λ_0 is large (and the turbulence heating is small), and vice versa. In the solar wind the fraction of shock heating increases because the correlation length increases with radial distance and turnover time of turbulence becomes large.

3.3.4 Dependence on the injection amplitude

We have also performed a parameter survey on wave amplitude, which strongly affects the mass flux of the solar wind (Suzuki & Inutsuka, 2006; Cranmer et al., 2007). Figure 3.4 shows how the solar wind velocity, maximum temperature, and mass-loss rate changes with correlation length and the wave amplitude. Three panels show the time-averaged solar wind velocity v_r at $r = 0.5\,\mathrm{au}$ (left), maximum temperature (center), and mass-loss rate in unit of $M_\odot\ \mathrm{yr}^{-1}$, respectively. Three lines correspond to different injection amplitude of $dv^+ = 0.7\,\mathrm{km\,s^{-1}}$ (blue), $dv^+ = 0.5\,\mathrm{km\,s^{-1}}$ (green), $dv^+ = 0.4\,\mathrm{km\,s^{-1}}$ (red), respectively, and the horizontal axis indicates the photospheric correlation length λ_0. Regardless of the injection amplitude, the solar wind velocity is larger for larger λ_0. The mass-loss rate shows only a slight trend with respect to λ_0 and the maximum temperature is almost constant in λ_0. The dependence on dv^+ is as follows. The solar wind velocity decreases as dv^+ increases. This seems mysterious because the larger energy injection leads to smaller wind velocity. The reason for this apparent contradiction is the sensitive dependence of the mass-loss rate on dv^+; the mass flux becomes $3-4$ times larger when dv^+ increases from $0.5\,\mathrm{km\,s^{-1}}$ to $0.7\,\mathrm{km\,s^{-1}}$. Because heavier wind is more difficult to accelerate, the solar wind velocity decreases for larger energy input. The maximum temperature shows a weak dependence on the injected energy, possibly because the conductive cooling of the corona and solar wind is larger for larger temperature.

3.4 Result: Case II

We discuss the dynamics of the corona and solar wind with different injection frequency or spectrum of Alfvén waves. The first half of case II discusses monochromatic wave injection given as

$$z^+_{\theta,\mathrm{bottom}} = 2a\sin\left(2\pi f_0 t\right), \tag{3.54}$$

$$z^+_{\phi,\mathrm{bottom}} = 2a\cos\left(2\pi f_0 t\right), \tag{3.55}$$

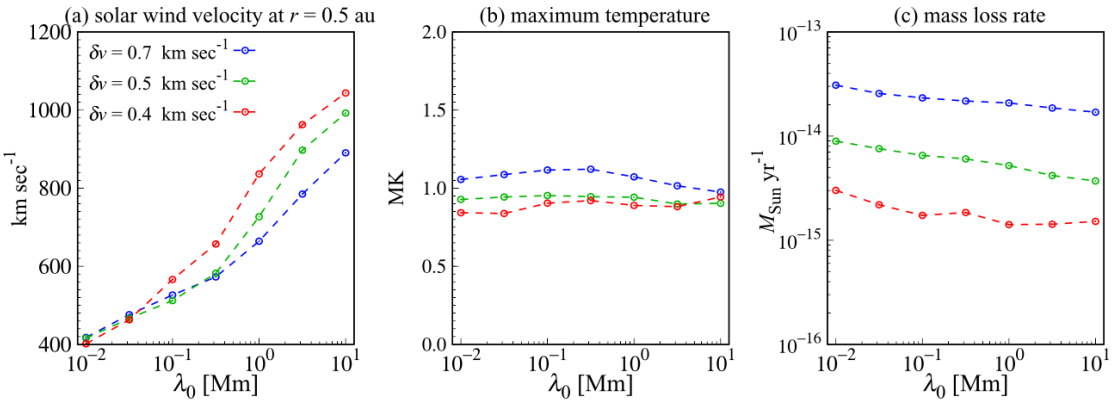

Figure 3.4: Dependence of solar wind parameters on the correlation length and the injected wave amplitude on the photosphere. Horizontal axis shows the photospheric correlation length and the different color of line corresponds to different wave amplitude. Three panels show the (a): termination velocity of the solar wind, (b): maximum temperature and (c): mass-loss rate, respectively. Figure reproduced from Shoda et al. (2018a).

where $a = 32\,\mathrm{km\,s^{-1}}$ and f_0 is a free parameter. The purpose of using monochromatic boundary condition is to simplify the physics. In the latter half, we impose a broadband wave injection at the bottom boundary given as

$$\boldsymbol{z}^+ \propto \int_{2\pi f_{\min}}^{2\pi f_{\max}} d\omega\, \omega^{-1} \sin\left(\omega t + \boldsymbol{\phi}_{\mathrm{rand}}(\omega)\right), \tag{3.56}$$

where $f_{\max}$ is fixed to 10^{-2} Hz and $f_{\min}$ is changed. The root-mean-square amplitude of outward Elsässer variable is fixed to $32\,\mathrm{km\,s^{-1}}$ at the lower boundary.

3.4.1 Monochromatic wave injection

Figure 3.5 shows the snapshots of quasi-steady states with various injection frequency. Each panel shows the radial profiles of mass density ρ, temperature T, radial velocity v_r, and Elsässer variables $z^{\pm}$, respectively. Three lines indicate the injection frequencies of $f_0 = 10^{-2.5}$ Hz, $f_0 = 10^{-3.5}$ Hz, and $f_0 = 10^{-4.5}$ Hz, respectively. In the bottom panel, the transparent solid lines and dashed lines indicate the outward and inward Elsässer amplitudes, respectively.

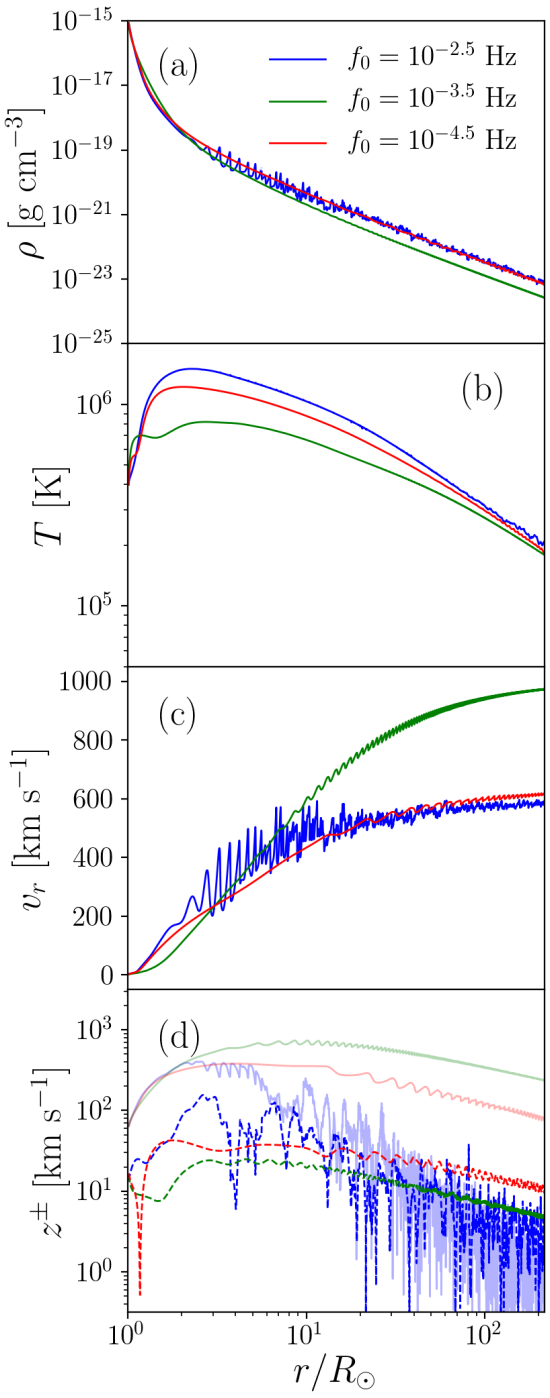

Figure 3.5: Snapshots of quasi-steady states with various wave injection frequency f_0 (monochromatic). Blue, green, and red lines correspond to $f_0 = 10^{-2.5}$ Hz, $f_0 = 10^{-3.5}$ Hz, $f_0 = 10^{-4.5}$ Hz, respectively. Transparent solid lines and dashed lines in the bottom panel indicate outward and inward Elsässer variables, respectively. Figure reproduced from Shoda et al. (2018b).

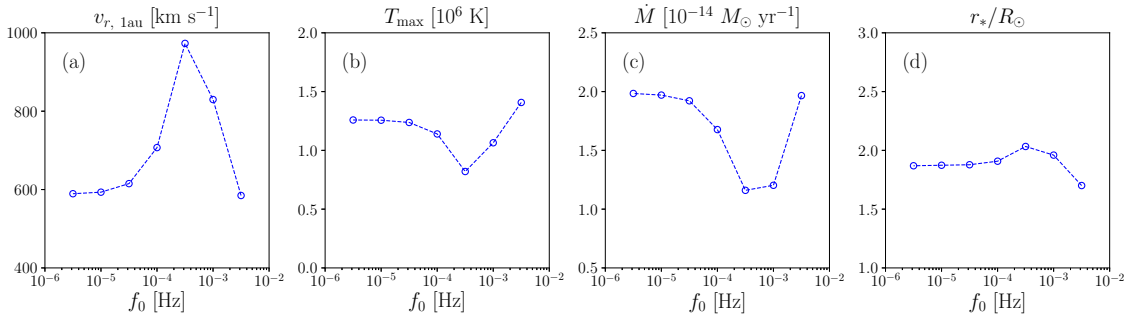

Figure 3.6: Time-averaged solar wind parameters with different wave injection frequencies f_0. Each panel shows the (a): radial velocity at 1 au, (b): maximum coronal temperature, (c): mass-loss rate, and (d): location of critical point, respectively. Figure reproduced from Shoda et al. (2018b).

The solar wind property does not monotonically depend on the injection frequency; the case with $f_0 = 10^{-3.5}$ Hz yields the most tenuous, coolest, fastest solar wind. This trend is more clearly seen in Figure 3.6, where we show the time-averaged wind parameters versus f_0. The non-monochromatic dependence on frequency indicates that two different wave heating mechanisms work depending on the wave frequency, and $f_0 = 10^{-3.5}$ Hz is a specific frequency that both processes do not work effectively. The parametric decay instability and the Alfvén wave turbulence can be such two mechanism. Since the growth rate of PDI is proportional to the wave frequency, the higher-frequency waves can dissipate easily via PDI. Meanwhile the cascading time of Alfvén wave turbulence depends on the amount of reflected wave, and therefore, low frequency waves that experience stronger reflection are preferable for turbulent dissipation.

$f_0 = 10^{-2.5}$ Hz shows quite different behavior compared with the other two cases; large-amplitude density fluctuations in the solar wind acceleration region and the amplitudes of $z^{\pm}$ are comparable around $r = 1$ au. This indicates that the parametric decay instability occurred only when $f_0 = 10^{-2.5}$ Hz. Note that the PDI yields the density fluctuation and the enhanced reflected Alfvén waves simultaneously. A mysterious result is that the PDI does not evolve when $f_0 \lesssim 10^{-3.5}$ Hz. The growth time of PDI is roughly

estimated as Eq. (2.2), which, when $f_0 = 10^{-4}$ Hz, yields

$$\tau_{\mathrm{PDI},\ f_0=10^{-4}\mathrm{Hz}} \approx 10^4 \text{ sec.} \tag{3.57}$$

The Alfvén-crossing time from the coronal base to 1 au is

$$\tau_{\mathrm{AC}} = \frac{1 \text{ au}}{v_A + v_r} \gtrsim \frac{1 \text{ au}}{10^3 \text{ km s}^{-1}} \approx 1.5 \times 10^5 \text{ sec}, \tag{3.58}$$

which is much larger than the growth time of PDI $\tau_{\mathrm{PDI},\ f_0=10^{-4}\mathrm{Hz}}$. It means that the Alfvén waves with frequency of 10^{-4} Hz has sufficiently long time for PDI growth before arriving 1 au, which is inconsistent with our numerical simulation. This indicates the strong quenching of PDI in the solar wind where plasma is expanding and accelerating.

3.4.2 Growth rate of PDI in the expanding/accelerating solar wind

The acceleration and expansion of the solar wind affects the development of waves and turbulence in the solar wind. Several works investigate the role of wind acceleration and expansion on PDI. Tenerani & Velli (2013) conduct 1D MHD simulations of PDI in a accelerating expanding box model to show the suppression of PDI by the diveregence of the wind. Similar result is confirmed in 2D MHD simulations under an expanding box model (Del Zanna et al., 2015). Here we derive a growth rate of PDI including the effects of expansion and acceleration of the solar wind.

Following Tenerani & Velli (2013), we evaluate quantitatively how wind acceleration and expansion quenches PDI. The conservation of mass is written as follows.

$$\frac{\partial}{\partial t}\left(\rho r^2 f\right) + \frac{\partial}{\partial r}\left(\rho v_r r^2 f\right) = 0. \tag{3.59}$$

Decoupling the mean (time-averaged) and fluctuation parts as

$$X = \overline{X} + \delta X, \tag{3.60}$$

the mass conservation is rewritten as

$$\frac{\partial}{\partial t}\left(\delta\rho r^2 f\right) + \frac{\partial}{\partial r}\left(\delta\rho\overline{v_r} r^2 f\right) + \frac{\partial}{\partial r}\left(\overline{\rho}\delta v_r r^2 f\right) = 0. \tag{3.61}$$

Suppose the $\delta\rho$ and δv_r satisfy a characteristic relation of slow-mode wave:

$$\delta\rho/\overline{\rho} = \delta v_r / c_s, \tag{3.62}$$

which yields

$$\frac{\partial}{\partial t}\left(\delta\rho r^2 f\right) + \frac{\partial}{\partial r}\left[\delta\rho\left(\overline{v_r} + c_s\right) r^2 f\right] = 0. \tag{3.63}$$

We assume that the spatial and temporal variation of $\delta\rho$ is approximately expressed as

$$\delta\rho \propto \exp\left[i\left(k(r)r - \omega t\right)\right]. \tag{3.64}$$

Here, for simplicity, we assume that $k(r)$ is always real and any amplification and decay of $\delta\rho$ are attributed to the imaginary part of ω. Then the relation between $k(r)$ and ω is given as

$$-i\omega + ik(r)\left(c_s + \overline{v_r}\right) + \frac{\left(c_s + \overline{v_r}\right)}{r^2 f}\frac{d}{dr}\left(r^2 f\right) + \frac{d}{dr}\left(c_s + \overline{v_r}\right) = 0. \tag{3.65}$$

When the background is nearly homogeneous, we obtain the dispersion relation of outward sound wave:

$$\omega = k(r)\left(c_s + \overline{v_r}\right). \tag{3.66}$$

When the background inhomogeneity is non-negligible, ω is expressed as

$$\omega = k(r)\left(c_s + \overline{v_r}\right) - i\gamma_{\rm exp} - i\gamma_{\rm acc}, \tag{3.67}$$

where $\gamma_{\rm exp}$ and $\gamma_{\rm acc}$ are factors of expansion and acceleration effects.

$$\gamma_{\rm exp} = (c_s + \overline{v_r}) \frac{d}{dr} \ln \left(r^2 f \right), \quad \gamma_{\rm acc} = \frac{d}{dr} (c_s + \overline{v_r}) \tag{3.68}$$

Eq. (3.67) shows the decay of density fluctuation by the wind expansion and acceleration. Since the growth of density fluctuation is a key in PDI, this result indicates that the PDI is possibly suppressed in the solar wind.

Another mechanism that suppresses PDI is the Doppler effect, or the box-stretching effect in the accelerating expanding box model (Tenerani & Velli, 2017). When we calculate the growth rate of PDI, we need to know the frequency of initial Alfvén wave. Exactly speaking, that frequency is the wave frequency in the co-moving frame with the background plasma. In a stationary solar wind, the frequency of Alfvén wave in the laboratory frame does not change, but it changes in the co-moving frame in the presence of accelerating flow. To see this effect, let us calculate how the intrinsic frequency changes as a result of accelerating flow. The dispersion relation of outward Alfvén wave is written as

$$\omega_0 = k(r) \left(v_A + v_r \right), \tag{3.69}$$

where ω_0 is the frequency observed from laboratory frame. When we observe from the co-moving frame, since the wavelength never changes (as long as the relativistic effect is negligible), the wave frequency $\tilde{\omega}$ should satisfy

$$\tilde{\omega} = k(r) v_A \tag{3.70}$$

Combining these two equations, we obtain

$$\tilde{\omega} = \frac{v_A}{v_A + v_r} \omega_0. \tag{3.71}$$

This equation shows that, in the presence of trans-Alfvénic flow, the intrinsic frequency

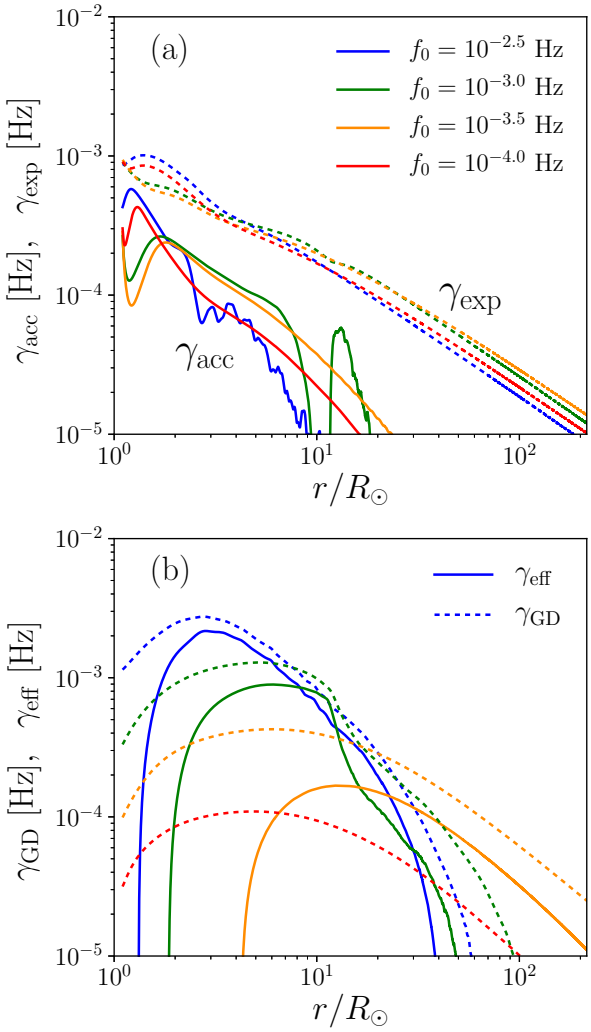

Figure 3.7: $\gamma_{\rm exp}$, $\gamma_{\rm acc}$, $\gamma_{\rm GD}$ and $\gamma_{\rm eff}$ versus heliocentric distance. Top panel corresponds to $\gamma_{\rm exp}$ (dashed line) and $\gamma_{\rm acc}$ (solid line), while bottom panel shows $\gamma_{\rm GD}$ and $\gamma_{\rm eff}$. Color of line corresponds to injection frequency: $f_0 = 10^{-2.5}$ Hz (blue), $f_0 = 10^{-3.0}$ Hz (green), $f_0 = 10^{-3.5}$ Hz (orange), $f_0 = 10^{-2.5}$ Hz (red). Figure reproduced from Shoda et al. (2018b).

becomes smaller. Note that the decrease of intrinsic frequency also appears in the wave action conservation (Bretherton & Garrett, 1968; Dewar, 1970). In the accelerating flow, the decrease in the wave energy density E is accompanied by the decrease in the intrinsic frequency $\tilde{\omega}$ to make the wave action density $E/\tilde{\omega}$ constant (in WKB regime).

We can now calculate the effective growth rate. First, the normalized growth rate is calculated as the largest growth mode of the Goldstein–Derby dispersion relation given

as (Goldstein, 1978; Derby, 1978)

$$\left(\tilde{\omega}^2 - \beta\tilde{k}^2\right)\left(\tilde{\omega} - \tilde{k}\right)\left(\tilde{\omega} + \tilde{k} - 2\right)\left(\tilde{\omega} + \tilde{k} + 2\right) = A^2\tilde{k}^2\left(\tilde{\omega}^3 + \tilde{k}\tilde{\omega}^2 - 3\tilde{\omega} + \tilde{k}\right), \tag{3.72}$$

where $\beta = a^2/v_A^2$, $\tilde{\omega} = \omega/\omega_0$, $\tilde{k} = k/k_0$, and $\eta = \delta B/B_0$ is the normalized Alfvén wave amplitude. ω_0 and k_0 are the frequency and wave number of the parent wave. We should note the ω_0 should not be the injection frequency $2\pi f_0$ but the frequency modified by the Doppler effect $2\pi f_0 v_r/\left(v_{r,0} + v_{A,0}\right)$. Denoting this growth rate as $\gamma_{\rm GD}$, the effective growth rate is given as

$$\gamma_{\rm eff} = \gamma_{\rm GD} - \gamma_{\rm eff} - \gamma_{\rm acc}. \tag{3.73}$$

Figure 3.7 shows $\gamma_{\rm exp}$, $\gamma_{\rm acc}$ (top panel) and $\gamma_{\rm GD}$, $\gamma_{\rm eff}$ (bottom panel) versus heliocentric distance. Color of line corresponds to injection frequency: $f_0 = 10^{-2.5}$ Hz (blue), $f_0 = 10^{-3.0}$ Hz (green), $f_0 = 10^{-3.5}$ Hz (orange), $f_0 = 10^{-4.0}$ Hz (red). The gap between solid and dashed line corresponds to the degree of growth-rate suppression. Interestingly, waves with $f_0 = 10^{-4}$ Hz are stabilized by the wind expansion/acceleration effects. The growth rate of $f_0 = 10^{-3.5}$ Hz waves is positive but sufficiently small that the wave resonance is prevented by the inhomogeneity of background (Tenerani & Velli, 2013).

3.4.3 Broadband wave injection

We next report the results with broadband wave injection focusing on the consistency with observation. For free parameter $f_{\rm min}$, we apply $f_{\rm min} = 10^{-3}$, 10^{-4}, 10^{-5} Hz. Regardless of $f_{\rm min}$, realistic solar wind is reproduced. Figure 3.8 shows the snapshots of quasi-steady states with different $f_{\rm min}$. Lines indicate the simulation results and symbols represent the observational values. In every simulation, high-temperature corona and fast solar wind are realistically reproduced. The difference between each run is not so significant as the monochromatic-wave case.

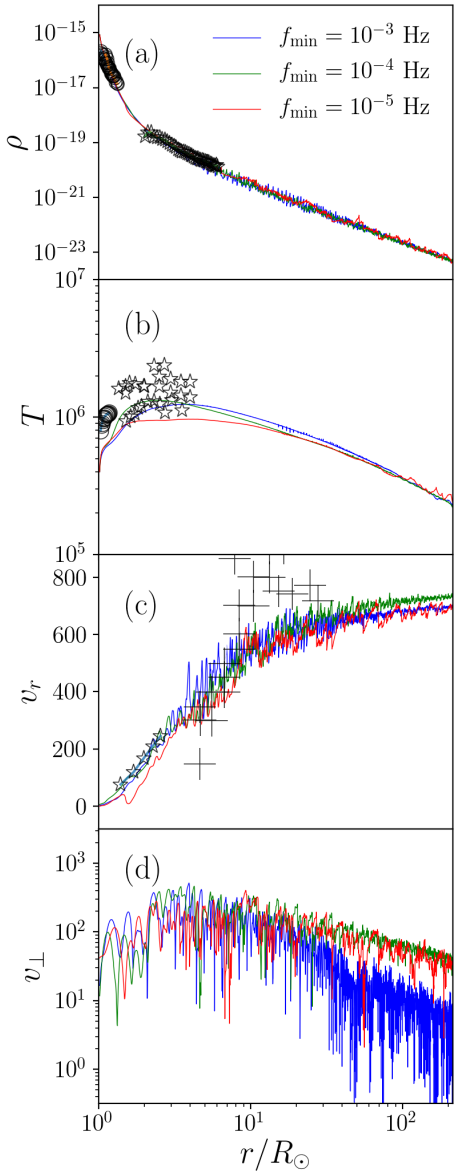

Figure 3.8: Snapshots in the quasi-steady states with different $f_{\rm min}$ values. Blue, green and red lines indicate $f_{\rm min} = 10^{-3}$ Hz, 10^{-4} Hz, 10^{-5} Hz, respectively. a: mass density. Shown by circles and stars are observations by Wilhelm et al. (1998) and by Lamy et al. (1997), respectively. b: temperature. Shown by circles and stars are observations by Landi (2008) and by Cranmer (2004, 2009), respectively. c: radial velocity. Shown by stars are ion outflow speed by Zangrilli et al. (2002), while the crosses represent the IPS observations (Kojima et al., 2004). d: transverse velocity. Figure reproduced from Shoda et al. (2018b).

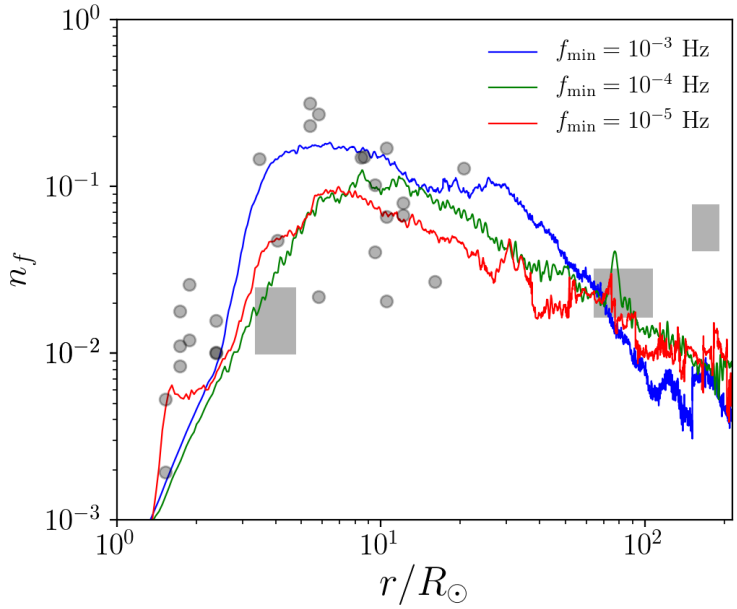

Figure 3.9: Fractional density fluctuation $n_f = \delta\rho/\rho$ versus radial distance. Red, green and blue lines correspond to $f_{\rm min} = 10^{-5}$ Hz, $f_{\rm min} = 10^{-4}$ Hz and $f_{\rm min} = 10^{-3}$ Hz, respectively. Shown by the gray symbols are the observational values. Figure reproduced from Shoda et al. (2018b).

Interestingly, the radial profile of density fluctuation is similar regardless of $f_{\rm min}$. Figure 3.9 shows the calculated density fluctuation the solid lines correspond to the simulations with $f_{\rm min} = 10^{-3}$ Hz (blue), $f_{\rm min} = 10^{-4}$ Hz (green), and $f_{\rm min} = 10^{-5}$ Hz (red), while grey symbols correspond to the observational values. Specifically, density fluctuation becomes maximum in the wind acceleration region for every line. This indicates that, as long as Alfvén waves include high-frequency components that are subject to parametric decay instability, the observed density fluctuation is explained.

Another observational constraint, the cross helicity evolution, is shown in Figure 3.10. The solid and dashed lines indicate the amplitudes of outward and inward Elsässer variables. Blue, green and red lines correspond to $f_{\rm min} = 10^{-3}$ Hz, $f_{\rm min} = 10^{-4}$ Hz and $f_{\rm min} = 10^{-5}$ Hz, respectively, while the gray lines indicate the observational trend by Bavassano et al. (2000). When $f_{\rm min} = 10^{-3}$ Hz, the outward wave amplitude becomes drastically smaller than the observational value. This inconsistency is possibly because

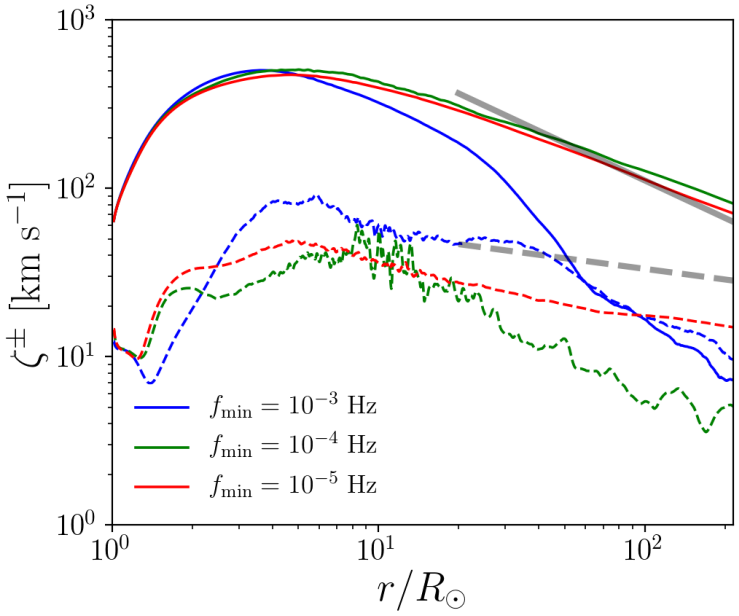

Figure 3.10: Amplitudes of Elsässer variables $\zeta^{\pm}$ (not $z^{\pm}$ in this Figure) as functions of heliocentric distance. Solid and dashed lines indicate the outward and inward Elsässer variables, respectively. Red, green and blue lines correspond to the minimum frequencies of $f_{\rm min} = 10^{-3}$ Hz (blue), $f_{\rm min} = 10^{-4}$ Hz (green) and $f_{\rm min} = 10^{-5}$ Hz, respectively. Also shown by grey lines are the observational trends by (Bavassano et al., 2000). Figure reproduced from Shoda et al. (2018b).

the parametric decay instability leads to an excessive reflection and dissipation of outward Alfvén waves. In other words, some fraction of outward Alfvén waves at the coronal bottom must be stable with respect to parametric decay instability to explain the observation. Indeed, the simulation is consistent with observation when $f_{\rm min} = 10^{-4}$ Hz or 10^{-5} Hz. Note that the Alfvén waves are subject to parametric decay instability only when $f_0 \lesssim 10^{-3.5}$ Hz.

3.5 Discussion

3.5.1 Heating mechanism in the solar wind

As Figure 3.3 shows, the total heating rate is almost invariant with respect to λ_0; if the turbulent heating becomes smaller, the shock heating compensates the decrement to maintain the total heating constant. This is explained as follows. When the turbulent heating becomes smaller, the plasma beta of the solar wind decreases because of the less chromospheric evaporation, which leads to the faster growth of the parametric decay instability. The faster growth of PDI by smaller turbulence heating yields larger shock heating to keep the total heating constant. This self-regulating mechanism is possibly a reason why the model without Alfvén wave turbulence (Suzuki & Inutsuka, 2005) and the model without PDI (Cranmer et al., 2007; Verdini et al., 2010) successfully explained the observation independently.

3.5.2 Parameter dependence of the solar/stellar wind

Figure 3.4 is worth comparing with previous works. First Cranmer et al. (2007) and Verdini et al. (2010) showed that the solar wind velocity is positively correlated with the correlation length, that is, large λ_0. large v_r. This is consistent with our result which shows the monotonic increase of v_r with respect to λ_0. The dependence of wave amplitude is discussed in Suzuki & Inutsuka (2006) and Cranmer et al. (2007), both of whom show a decreasing trend of v_r with respect to λ_0. This is also consistent with our work. The mass-loss rate of our work is also consistent with Cranmer et al. (2007) in that $\dot{M}$ shows slightly decreasing trend in λ_0 and sensitive dependence on dv^+.

3.5.3 Correlation length

The motivation of parameter survey with respect to λ_0 is not only to understand the physics, but also to prepare for the observation of the correlation length. Unfortunately, no one have ever observed the correlation length of Alfvén wave in the solar atmosphere,

and therefore, λ_0 is still a free parameter. λ_0 should, at least, depend on the wave generation mechanism. Provided that most of the Alfvén waves are generated inside the vortex motion of magnetic patches (van Ballegooijen et al., 1998, 2011), λ_0 should be typically 10^2 km (Berger et al., 1995; Berger & Title, 2001). Meanwhile if the swaying motion of the flux tube by the granular cell is dominant (Steiner et al., 1998), λ_0 should be the size of granular cell, that is, 10^3 km. To solve this problem, we need a super-high-resolution observation that resolves the fine-scale flow inside the magnetic elements, which is now impossible. Realistic numerical simulations, such as Moll et al. (2012) and Iijima & Yokoyama (2017) would be a powerful tool to determine the realistic value of λ_0.

3.5.4 On the role of parametric decay instability

Perez & Chandran (2013) showed that Alfvén wave turbulence is insufficient to deposit heat in the solar wind when $\lambda_0 = 1$ Mm. In our simulation, even when $\lambda_0 = 1$ Mm, the corona and solar wind are reproduced with realistic structure, indicating a sufficient heating. Since the dominant heating mechanism is the turbulence heating when $\lambda_0 = 1$ Mm, it means that PDI enhanced Alfvén wave turbulence. Reminding the fact that PDI generates backward Alfvén wave that drives turbulence, this is an acceptable understanding. In this regard, in contrast to the classical phrase of reflection-driven Alfvén-wave turbulence model, our model should be called PDI-driven Alfvén-wave turbulence model of the solar wind.

3.5.5 Frequency-filtering mechanism

The frequency-filtering mechanism can operate in the corona and solar wind due to the bimodal behavior of wave dissipation with respect to frequency. The low-frequency ($f_0 \lesssim 10^{-4}$ Hz) waves undergo linear reflection and generate Alfvénic turbulence from the interaction with counter-propagating waves. The high-frequency ($f_0 \gtrsim 10^{-3}$ Hz) waves dissipate through the PDI. As a result of the efficient heating, dense, hot and relatively slow winds are driven in the cases with $f_0 \lesssim 10^{-4}$ Hz or $f_0 \gtrsim 10^{-3}$ Hz. In contrast,

the intermediate-frequency ($f_0 \approx 10^{-3.5}$ Hz) waves are not severely subjected to these damping mechanisms. As a result, fast and less dense wind emanates from the relatively cool corona in this case. This indicates that the corona and solar wind have a frequency-filtering effect of the Alfvén wave, and as a result, the medium-frequency wave is likely to permeate. This is a possible reason for the hour-scale waves observed in the solar wind (Belcher & Davis, 1971).

3.5.6 Density fluctuation and cross helicity

As long as high-frequency waves that are subject to parametric decay instability have a non-negligible power, the observed density fluctuation is explained (Figure 3.9) Interestingly, the location of maximum density fluctuation is the same as that of maximum growth rate of parametric decay instability. These results support a scenario that the density fluctuation in the wind acceleration comes from parametric decay instability. Meanwhile, when all the injected Alfvén waves are unstable with respect to parametric decay instability, although density fluctuation is accountable, the cross helicity evolution is no longer consistent with observation (Figure 3.10). To summarize, high-frequency waves ($f_0 \gtrsim 10^{-3.5}$ Hz) are required to explain the density fluctuation and low-frequency waves ($f_0 \lesssim 10^{-3.5}$ Hz) are required to explain the cross helicity. The broadband nature of the Alfvén waves is a key to understand the observational facts.

3.6 Summary

By introducing new terms corresponding to turbulent dissipation of Alfvén wave turbulence into 1D compressible MHD equations, a model of the solar wind including parametric decay instability and Alfvén wave turbulence is constructed. The reflection-driven Alfvén wave turbulence (or standard) model is modified by parametric decay instability in two senses. First, due to the generation of shock waves by parametric decay instability, the heating rate is enhanced. Second, the reflection rate increases due to the large density

fluctuation to activate the turbulence in the solar wind. The shortage of heating in the standard model is resolved in this way.

The dominant heating mechanism is dependent on the correlation length. With the solar parameter (photospheric correlation length of $1\ \mathrm{Mm}$), turbulence heating is slightly larger than the shock heating in the wind acceleration region. It does not mean that the role of parametric decay instability is ignorable. Due to the large density fluctuation, in spite of modified turbulence model that weakens the turbulent dissipation (van Ballegooijen & Asgari-Targhi, 2017), the fast solar wind is reproduced. It indicates that the turbulence heating is supported by parametric decay instability. Consistently with previous works, the mass-loss rate is determined by the amplitude of injected Alfvén waves. The dependence of the mass-loss rate on the photospheric upward Poynting flux is super-linear, possibly because the reflection rate at the transition region is reduced for large energy input.

The parameter survey with respect to frequency has revealed that Alfvén waves with frequency smaller than $10^{-3.5}\ \mathrm{Hz}$ are not subject to parametric decay instability. This is because the acceleration, expansion and Doppler effect of the solar wind reduces the growth rate. An analytical expression of the growth rate is derived including these effects. We find that there exists a spatial correlation between growth rate of parametric decay instability and magnitude of density fluctuation, indicating that the origin of density fluctuation be parametric decay instability.

Our model is a unified model of Alfvén wave turbulence model (Cranmer et al., 2007; Verdini et al., 2010; Lionello et al., 2014) and parametric decay instability model (Suzuki & Inutsuka, 2005, 2006). However, the validation of the turbulence model is controversial. To validate the physical scenario revealed in this Chapter, we need to conduct the three dimensional simulation.

Chapter 4

3D simulations of the fast solar wind

4.1 Introduction

One-dimensional models with phenomenological turbulence model are discussed in Chapter 3. By introducing compressible processes into the standard Alfvén wave turbulence scenario, the observed density fluctuation turns out to be accountable by parametric decay instability. 1D simulation is, however, often controversial since we simplify the cascading processes via turbulence modeling. Another problem arises when we need to compare the observation of turbulence with simulation, because observational characteristics of turbulence such as power spectrum or correlation function are never predictable from 1D simulation. To summarize, although 1D simulation is useful in understanding physics, it has problems from both theoretical and observational aspects; theoretically turbulence modeling should be tested and modified using 3D simulation and observationally a direct prediction for in-situ measurement is necessary.

Based on discussions above, we conduct the first, three-dimensional, magnetohydrodynamic simulation of the solar wind acceleration. Although there exists 3D MHD simulation of the coronal loop heating (Dahlburg et al., 2016; Matsumoto, 2018), no 3D MHD simulations have ever successfully performed for coronal hole and fast solar wind, mainly because of anomalously quick thermal conduction. Based on the assumption that the ther-

mal conduction is Spitzer-Härm type, then the timescale of conduction $\tau_{\rm cnd}$ is given as

$$\tau_{\rm cnd} = \kappa_0^{-1} \frac{2k_B}{\gamma - 1} T^{-5/2} n_e \tag{4.1}$$

$$\approx 4 \times 10^{-5}\ {\rm s} \left(\frac{T}{10^6\ {\rm K}} \right)^{-5/2} \left(\frac{\Delta x}{1\ {\rm Mm}} \right)^2 \left(\frac{n_e}{10^4\ {\rm cc}} \right), \tag{4.2}$$

where Δx is the smallest spatial scale of fluctuation, practically the grid size. Thus the time scale of thermal conduction is in the order of 10^{-5} s, while the required time to accelerate the solar wind $\tau_{\rm acc}$ is given as the sound crossing time as

$$\tau_{\rm acc} \approx \int_{r_{\rm in}}^{r_{\rm out}} \frac{dr}{a + v_r} \gtrsim 2 \times 10^4\ {\rm s}, \tag{4.3}$$

where $r_{\rm in}$ and $r_{\rm out}$ are radial distances of inner and outer boundaries, respectively, and a and v_r are the sound and radial bulk velocities, respectively. Thus we need approximately 10^9 time steps for the solar wind to be accelerated, which is numerically too expensive. A recently proposed numerical method called super-time-stepping method (Meyer et al., 2012, 2014) enables us to reduce the numerical cost coming from parabolic terms such as thermal conduction. By employing this method, 3D simulations become available.

As an introduction of three-dimensional simulation, we discuss the reason why we need to conduct 3D simulation from both theoretical and observational view points.

4.1.1 Theoretical motivation

The theoretical motivations for 3D simulation are to overcome several limitations of 1D simulations. The first is that the phenomenological turbulence model used in Chapter 3 would be problematic for application to compressible MHD equations. The model is derived from reduced MHD, in which fast and slow mode waves are excluded. Note that the fast-mode turbulence has different feature than Alfvén wave turbulence, and thus the two modes should be solved seperately (Suzuki et al., 2007; Cranmer & van Ballegooijen, 2012), while our 1D model ignores the difference between fast mode wave and Alfvén

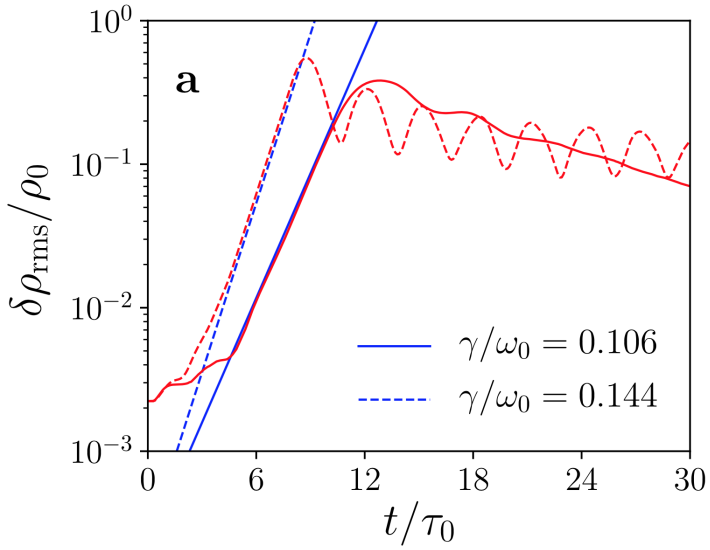

Figure 4.1: Comparison of the growth rates of parametric decay instability between 1D and 3D settings. The angles between the mean magnetic field and the wave number of density fluctuation are $0°$ (1D setting) and $45°$ (3D setting). Red solid and dashed lines indicate the magnitude of normalized density fluctuation as functions of time. Blue solid and dashed lines are the fitted lines in the growth phase of instability. Figure reproduced from Shoda & Yokoyama (2018a).

wave in low-beta region.

The phenomenological model of Alfvén wave turbulence is also worth being revisited. The simplest model of reduced MHD turbulence assume that the inward and outward Elsässer variables have the same correlation length ($\lambda^+ = \lambda^- = \lambda$) and the correlation length expands with the radius of flux tube ($\lambda \propto B_r^{-1/2}$). In reality, the correlation lengths of inward and outward Elsässer variables should be different and be solved independently via transport equation (Zank et al., 2017; Shiota et al., 2017; Zank et al., 2018). Besides, in the presence of compressible waves (density fluctuation) with finite perpendicular wave number, the phase mixing begins to work (Heyvaerts & Priest, 1983). For example, the phase mixing plays a non-negligible role in the early phase of parametric decay instability (Shoda & Yokoyama, 2018a) and therefore should be taken into account.

In 1D models, we limit the propagation direction parallel to the mean field. In the

actual corona and solar wind, the direction of wave propagation is possibly oblique to the mean field. In other words, fluctuations can be inhomogeneous perpendicular to the mean magnetic field. For example in the coronal bottom, taking the horizontal correlation length of $10\ \mathrm{Mm}$, correlation time (period) of $100\ \mathrm{s}$ and Alfvén speed of $1\ \mathrm{Mm\ s^{-1}}$, then the angle of wave number vector with respect to mean (vertical) magnetic field is

$$\Theta_{\boldsymbol{k}} = \tan^{-1}\left(\frac{100\ \mathrm{Mm}}{10\ \mathrm{Mm}}\right) = 84^{\circ}, \tag{4.4}$$

showing the almost perpendicular propagation. In fact, the density fluctuation near the coronal base is observed to be highly inhomogeneous perpendicular to magnetic field line (Raymond et al., 2014). The oblique wave number affects the growth of parametric decay instability. Figure 4.1 compares the growth of parametric decay instability between parallel and oblique propagations of compressible wave. Here the oblique case corresponds to the propagation angle of 45°. Dashed (parallel) and solid (oblique) red lines represent the root-mean-square density fluctuation versus time. The dashed and solid blue lines are the fitted exponential function. The oblique propagation case shows 26% smaller growth rate than the parallel propagation case. In other words, the 1D calculation overestimates the growth rate and thus the magnitude of density fluctuation.

4.1.2 Observational motivation

While the solar wind is believed to be heated and accelerated by turbulence, until 2017, observation of turbulence had been available beyond $0.3\ \mathrm{au}$ from the Sun, which is much farer from the wind acceleration region near $10R_{\odot}$. A new spacecraft *Parker Solar Probe* (hereafter *PSP*) has been launched and begun to observe the much closer region (Fox et al., 2016). The perihelion of *PSP* is expected to be as close as $9.86R_{\odot}$ from the center of the Sun, and thus the direct observation of solar wind turbulence in the wind acceleration region would be available. *PSP* has four instruments: FIELDS for electromagnetic and fluid values (Bale et al., 2016), IS⊙IS for energetic particles (McComas et al., 2016), WISPR

for coronal imaging (Vourlidas et al., 2016) and SWEAP for major particles (Kasper et al., 2016). Amongst these instruments, FILEDS would be the best to compare with our numerical calculation because we directly calculate fluid and electromagnetic field values.

By providing synthesized data based on our simulation results, one can make a direct comparison with the observed data with better interpretations. Suppose *PSP* flies in a quasi-periodically oscillating vortex with length L and period τ, then the time series of *PSP* data is predicted to have two time scales: τ and $L/v_{\rm PSP}$ where $v_{\rm PSP}$ is the velocity of *PSP*. In other words, *PSP* data involve both temporal and spatial variations of turbulence. In the vicinity of the Sun, these two time scales can be similar, and thus it is highly possible that observation cannot distinguish the spatial and temporal variation by itself. Numerical simulation and the direct prediction from it would be helpful to distinguish the two variations.

4.1.3 Purpose of 3D simulation

To summarize the introduction, we have two purposes to perform 3D simulation. First, to test the results and conclusions of 1D simulations, we discuss how similar the results of 3D simulations are to those of 1D simulations. Specifically, since the parametric decay instability (PDI) is the key in 1D simulations, we investigate whether PDI really works in three-dimensional setting.

Second, we aim to provide theoretical predictions for *Parker Solar Probe*. The data of *Parker Solar Probe* would involve both spatial and temporal variations of turbulence in the solar wind, making the physical interpretation difficult. For better interpretation, a direct prediction from simulation is required.

4.2 Method

The basic equations are ideal MHD equations with gravity and Spitzer-Härm type thermal conduction and are solved in the spherical coordinate. We describe in this section the basic

equations and numerical setting in this study.

4.2.1 Local spherical coordinate

The spherical coordinate is appropriate to follow the radial expansion of magnetic field line and is used in the calculation. Specifically, in order to make the horizontal coordinates symmetric, we use the local spherical coordinate that is defined as follows. In the usual spherical coordinate, a gradient of scalar X is given as

$$\nabla X = \boldsymbol{e}_r \frac{\partial X}{\partial r} + \boldsymbol{e}_\theta \frac{1}{r} \frac{\partial X}{\partial \theta} + \boldsymbol{e}_\phi \frac{1}{r \sin\theta} \frac{\partial X}{\partial \phi}. \tag{4.5}$$

The local spherical coordinate assumes $\theta \approx \pi/2$, which yields the approximated gradient as

$$\nabla X \approx \boldsymbol{e}_r \frac{\partial X}{\partial r} + \boldsymbol{e}_\theta \frac{1}{r} \frac{\partial X}{\partial \theta} + \boldsymbol{e}_\phi \frac{1}{r} \frac{\partial X}{\partial \phi}. \tag{4.6}$$

The accuracy of this approximation depends on the range of θ we consider. Replacing θ with $\theta' = \theta - \pi/2$, $\sin\theta$ is approximated as

$$\sin\theta \approx 1 - \frac{1}{2}\theta'^2. \tag{4.7}$$

Therefore, the error of our approximation is at most θ'^2. In the solar wind simulation, the required horizontal extension of the simulation domain at the coronal base is $10 - 20$ Mm (Perez & Chandran, 2013). In this case, the maximum error is

$$\max\left(\theta'^2\right) = \left(\frac{10\ \mathrm{Mm}}{R_\odot}\right)^2 \approx 10^{-4}. \tag{4.8}$$

4.2.2 Basic equations and numerical solver

The basic equations we use are the ideal MHD equations with gravity and thermal conduction given as

$$\frac{\partial}{\partial t}\boldsymbol{U} + \frac{1}{r^2}\frac{\partial}{\partial r}\left(\boldsymbol{F}_r r^2\right) + \frac{1}{r}\frac{\partial}{\partial \theta}\boldsymbol{F}_\theta + \frac{1}{r}\frac{\partial}{\partial \phi}\boldsymbol{F}_\phi = \boldsymbol{S}, \tag{4.9}$$

where

$$\boldsymbol{U} = \begin{pmatrix} \rho \\ \rho v_r \\ \rho v_\theta \\ \rho v_\phi \\ B_r \\ B_\theta \\ B_\phi \\ e \end{pmatrix}, \quad \boldsymbol{F}_r = \begin{pmatrix} \rho v_r \\ \rho v_r^2 - \dfrac{B_r^2}{4\pi} + p_T \\ \rho v_r v_\theta - \dfrac{B_r B_\theta}{4\pi} \\ \rho v_r v_\phi - \dfrac{B_r B_\phi}{4\pi} \\ 0 \\ v_r B_\theta - v_\theta B_r \\ v_r B_\phi - v_\phi B_r \\ (e + p_T) v_r - \dfrac{B_r}{4\pi}(\boldsymbol{v}\cdot\boldsymbol{B}) \end{pmatrix}, \quad \boldsymbol{F}_\theta = \begin{pmatrix} \rho v_\theta \\ \rho v_r v_\theta - \dfrac{B_r B_\theta}{4\pi} \\ \rho v_\theta^2 - \dfrac{B_\theta^2}{4\pi} + p_T \\ \rho v_\theta v_\phi - \dfrac{B_\theta B_\phi}{4\pi} \\ v_\theta B_r - v_r B_\theta \\ 0 \\ v_\theta B_\phi - v_\phi B_\theta \\ (e + p_T) v_\theta - \dfrac{B_\theta}{4\pi}(\boldsymbol{v}\cdot\boldsymbol{B}) \end{pmatrix},$$

$$\boldsymbol{F}_\phi = \begin{pmatrix} \rho v_\phi \\ \rho v_r v_\phi - \dfrac{B_r B_\phi}{4\pi} \\ \rho v_\theta v_\phi - \dfrac{B_\theta B_\phi}{4\pi} \\ \rho v_\phi^2 - \dfrac{B_\phi^2}{4\pi} + p_T \\ v_\phi B_r - v_r B_\phi \\ v_\phi B_\theta - v_\theta B_\phi \\ 0 \\ (e + p_T) v_\phi - \dfrac{B_\phi}{4\pi}(\boldsymbol{v}\cdot\boldsymbol{B}) \end{pmatrix}, \quad \boldsymbol{S} = \begin{pmatrix} 0 \\ \rho\left(v_\theta^2 + v_\phi^2\right)/r + \left(2p + \dfrac{B_r^2}{4\pi}\right)/r + \rho g \\ \left(\dfrac{1}{4\pi}B_r B_\theta - \rho v_r v_\theta\right)/r \\ \left(\dfrac{1}{4\pi}B_r B_\phi - \rho v_r v_\phi\right)/r \\ 0 \\ \left(v_r B_\theta - v_\theta B_r\right)/r \\ \left(v_r B_\phi - v_\phi B_r\right)/r \\ \rho g v_r + Q_{\mathrm{cnd}} \end{pmatrix},$$

where

$$e = \frac{p}{\gamma - 1} + \frac{1}{2}\rho \boldsymbol{v}^2 + \frac{\boldsymbol{B}^2}{8\pi}, \quad p_T = p + \frac{\boldsymbol{B}^2}{8\pi}, \quad g = -\frac{GM_\odot}{r^2}. \tag{4.10}$$

G is the gravitational constant and $M_\odot$ is the solar mass. For the specific heat ratio γ, we use the adiabatic value: $\gamma = 5/3$. The hyperbolic divergence cleaning method

(Dedner et al., 2002) is used to remove the numerically generated $\nabla \cdot \boldsymbol{B}$. Note that the conserved variable $\boldsymbol{U}$ and corresponding fluxes $\boldsymbol{F}_{r,\theta,\phi}$ are the same as those in Cartesian coordinates. The differences arise in the geometry factor in $\boldsymbol{F}_r$ and the source terms. To numerically solve the ideal MHD equations, we use HLLD solver (Miyoshi & Kusano, 2005) to calculate $\boldsymbol{F}_{r,\theta,\phi}$. In the reconstruction procedure, we use 5th-order MP5 method (Suresh & Huynh, 1997) for $\boldsymbol{v}$ and $\boldsymbol{B}$ and 2nd-order MUSCL method (van Leer, 1979) with minmod limiter (Roe, 1986) for ρ, p and ψ. High-order reconstructions of velocity and magnetic field are to minimize the numerical damping of Alfvén waves. Third-order SSP Runge–Kutta method (Shu & Osher, 1988) is used for time integration.

We use the same equation of state as van Ballegooijen & Asgari-Targhi (2016); we assume fully ionized hydrogen plasma with 10% contamination of helium. The equation of state is given as

$$p = c_1 \rho T, \tag{4.11}$$

where $c_1 = 2.3 k_B / (1.4 m_H)$. Here k_B is the Boltzmann constant and m_H is the hydrogen mass.

The radiative cooling, which is in general not negligible in the coronal base (Matsumoto & Suzuki, 2014; van Ballegooijen & Asgari-Targhi, 2016), is excluded for simplicity. Instead of solving the radiative cooling, we fix the coronal base temperature and attribute the cooling near the base to thermal conduction. As for thermal conduction, we use the following formula:

$$Q_{\rm cnd} = -\nabla \cdot \boldsymbol{q}_{\rm cnd}, \quad \boldsymbol{q}_{\rm cnd} = -\kappa_0 \xi(r) T^{5/2} \begin{pmatrix} \hat{b}_r^2 & 0 & 0 \\ 0 & f_{\rm red} \hat{b}_\theta^2 & 0 \\ 0 & 0 & f_{\rm red} \hat{b}_\phi^2 \end{pmatrix} \cdot \nabla T, \tag{4.12}$$

where $\kappa_0 = 10^{-6}$ in cgs unit and $\hat{\boldsymbol{b}} = (b_r, b_\theta, b_\phi) = \boldsymbol{B} / |\boldsymbol{B}|$ is the unit vector parallel to the local magnetic field. Meanwhile the Spitzer-Härm type conductive flux $\boldsymbol{q}_{\rm SH}$ is given

as

$$\boldsymbol{q}_{\rm SH} = -\kappa_0 T^{5/2} \hat{\boldsymbol{b}}\hat{\boldsymbol{b}} \cdot \nabla T = -\kappa_0 T^{5/2} \begin{pmatrix} \hat{b}_r^2 & \hat{b}_r\hat{b}_\theta & \hat{b}_r\hat{b}_\phi \\ \hat{b}_r\hat{b}_\theta & \hat{b}_\theta^2 & \hat{b}_\theta\hat{b}_\phi \\ \hat{b}_r\hat{b}_\phi & \hat{b}_\theta\hat{b}_\phi & \hat{b}_\phi^2 \end{pmatrix} \cdot \nabla T. \tag{4.13}$$

The first difference is the factor $\xi(r)$. This comes from the observational implication that the Spitzer-Härm conductive flux is larger than the observed heat flux. To solve this problem, Hollweg (1974, 1976) proposed an idea that the conductivity switches into another form in the vicinity of wind acceleration region. Following this idea, we quench the conductivity beyond $r \approx 5R_\odot$ via $\xi(r)$ as

$$\xi(r) = \min\left(1, \frac{r_{\rm sw}^2}{r^2}\right), \tag{4.14}$$

where $r_{\rm sw} = 5R_\odot$.

The other differences are found in matrix $\hat{\boldsymbol{b}}\hat{\boldsymbol{b}}$. We ignore the non-diagonal component of $\hat{\boldsymbol{b}}\hat{\boldsymbol{b}}$ for two reasons. First, the non-diagonal component of $\hat{\boldsymbol{b}}\hat{\boldsymbol{b}}$ can be a cause of negative temperature (Sharma & Hammett, 2007), and second, because the direction of local magnetic field is random, the non-diagonal components vanish when time-averaged:

$$\overline{\begin{pmatrix} \hat{b}_r^2 & \hat{b}_r\hat{b}_\theta & \hat{b}_r\hat{b}_\phi \\ \hat{b}_r\hat{b}_\theta & \hat{b}_\theta^2 & \hat{b}_\theta\hat{b}_\phi \\ \hat{b}_r\hat{b}_\phi & \hat{b}_\theta\hat{b}_\phi & \hat{b}_\phi^2 \end{pmatrix}} \approx \begin{pmatrix} \overline{\hat{b}_r^2} & 0 & 0 \\ 0 & \overline{\hat{b}_\theta^2} & 0 \\ 0 & 0 & \overline{\hat{b}_\phi^2} \end{pmatrix}, \tag{4.15}$$

where $\overline{X}$ denotes the time-average of X. Since the thermal conduction affects the wind velocity and mass flux and we are interested in the time-averaged value of them, the non-diagonal components are ignored. In addition, the conductive fluxes in θ and ϕ components are reduced by the factor of $f_{\rm red}$, reducing the numerical cost of thermal conduction. The role of thermal conduction is to radially distribute the heat deposited by wave dissipation, and therefore the horizontal thermal conduction can be reduced unless unrealistically

large temperature gap is observed. We apply $f_{\rm red} = 0.1$ in this study.

The thermal conduction is numerically solved separately from the ideal MHD equations using super-time-stepping method (Meyer et al., 2012, 2014), an explicit solver of parabolic equation that reduces the numerical cost.

4.2.3 Numerical settings

The simulation domain extends from the coronal base ($r_{\rm min} = 1.02 R_\odot$) to beyond the wind acceleration region ($r_{\rm max} = 20 R_\odot$). We solve in the range of $\theta_{\rm min} \le \theta \le \theta_{\rm max}$ and $\phi_{\rm min} \le \phi \le \phi_{\rm max}$, where

$$\theta_{\rm max} = \phi_{\rm max} = \frac{L_{\rm bottom}}{2R_\odot} \ {\rm rad}, \quad \theta_{\rm min} = \phi_{\rm min} = -\frac{L_{\rm bottom}}{2R_\odot} \ {\rm rad}. \tag{4.16}$$

Note that the horizontal size of numerical domain at the bottom boundary is approximately $L_{\rm bottom} = 20$ Mm. As auxiliary variables, we introduce x, y and $L(r)$ as

$$x = r\theta, \quad y = r\phi, \quad L(r) = r\left(\theta_{\rm max} - \theta_{\rm min}\right) = r\left(\phi_{\rm max} - \phi_{\rm min}\right), \tag{4.17}$$

where x and y represent the displacements in θ and ϕ directions and $L(r)$ represents the size of flux tube at radial distance of r.

The number of grid points are $(6600, 192, 192)$ in (r, θ, ϕ) directions. The radial grid size is fixed to 2 Mm independently of r. As the initial condition, we impose the isothermal Parker wind solution (Parker, 1958) with basal density of $\rho_0 = 8.5 \times 10^{-16}$ g cm^{-3} and temperature of $T = 1.1 \times 10^6$ K.

The periodic boundary conditions are used for θ and ϕ directions. The bottom boundary ($r = r_{\rm min}$) conditions are as follows. The fixed boundary condition is used for density, temperature and radial magnetic field as

$$\rho_{\rm bottom} = 8.5 \times 10^{-16} \ {\rm g \ cm^{-3}}, \quad T_{\rm bottom} = 6.0 \times 10^5 \ {\rm K}, \quad B_{r,{\rm bottom}} = 2.0 \ {\rm G}, \tag{4.18}$$

while the free boundary condition is used for the radial velocity:

$$\left.\frac{\partial}{\partial r} v_r \right|_{\rm bottom} = 0. \tag{4.19}$$

The horizontal components of the velocity and magnetic field are given in terms of Elsässer variables ($z^{\pm}_{\theta,\phi} = v_{\theta,\phi} \mp B_{\theta,\phi}/\sqrt{4\pi\rho}$). The upward Elsässer variable is fixed as

$$z^{+}_{\theta,\phi,\rm bottom} = \sum_{n_x=1}^{3}\sum_{n_y=1}^{3}\sum_{l=1}^{10} P\left(n_x, n_y, l\right) \exp\left[i\left(\pi n_x \theta/\theta_{\rm max} + \pi n_y \phi/\phi_{\rm max} + 2\pi l f_0 t + \Phi_{\theta,\phi}\left(n_x, n_y, l\right)\right)\right], \tag{4.20}$$

where $P\left(n_x, n_y, l\right) \propto \left(n_x^2 + n_y^2\right)^{-1/2} l^{-1/2}$ and $\Phi_{\theta,\phi}\left(n_x, n_y, l\right)$ is the random phase function. The amplitude of $z^{+}_{\theta,\phi,\rm bottom}$ is determined so that the root-mean-square value of $\sqrt{{z^{+}_{\theta,\rm bottom}}^2 + {z^{+}_{\phi,\rm bottom}}^2}$ is fixed to $60\ {\rm km\ s^{-1}}$. The typical frequency f_0 is

$$f_0 = 10^{-3}\ {\rm Hz}. \tag{4.21}$$

The boundary condition of inward Elsässer variables is free boundary condition:

$$\left.\frac{\partial}{\partial r} z^{-}_{\theta,\phi} \right|_{\rm bottom} = 0. \tag{4.22}$$

As for the top boundary, we apply a marginal numerical region that extends beyond $1000 R_\odot$ with radially expanding mesh. Since the supersonic and super-Alfvénic outflow is generated in the quasi-steady state, the choice of boundary condition does not affect the calculation result.

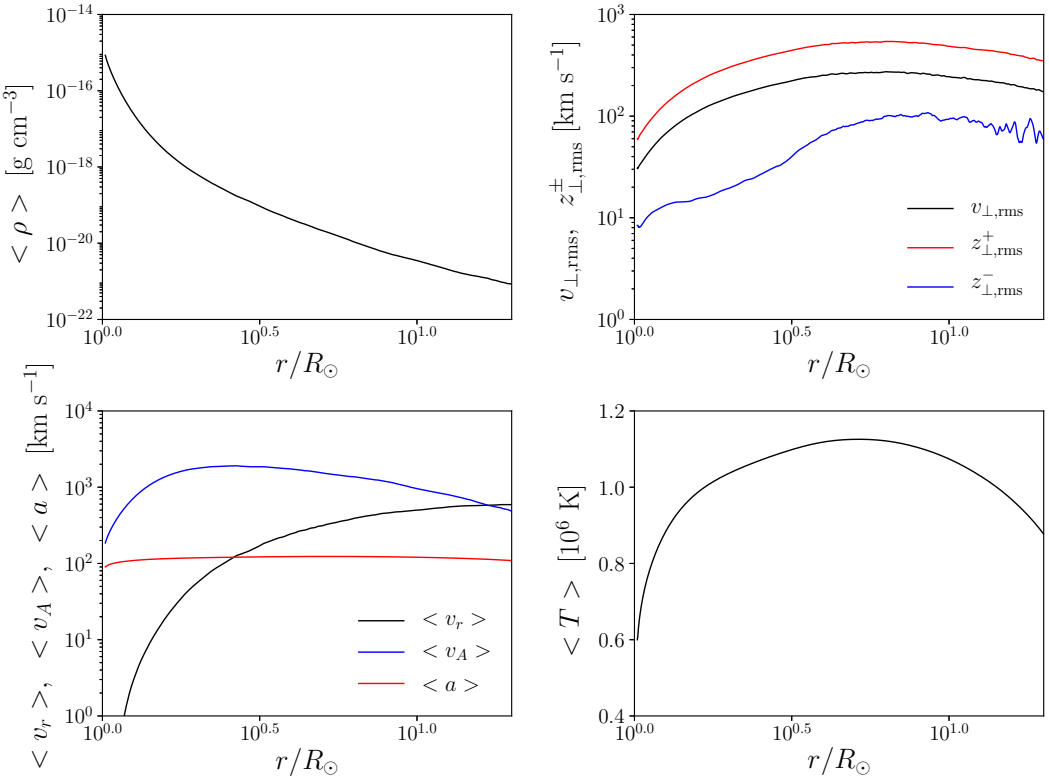

Figure 4.2: Horizontally and temporally averaged variables as functions of r in a quasi-steady state. Left top: mass density. Right top: root-mean-squared transverse velocity (black) and Elsässer variables (blue: outward, red: inward). Left bottom: radial velocity (black), Alfvén velocity (blue) and sound velocity (red). Right bottom: temperature.

4.3 Result

4.3.1 Averaged 1D structure in the quasi-steady state

We calculate the basic equations until the system reaches a quasi-steady state. To see the radial variance of the solar wind, we first calculate the temporal and horizontal averages of solar wind parameters. Here we directly average the density, temperature, radial velocity, Alfvén velocity $v_A = B_r/\sqrt{4\pi\rho}$ and sound velocity $a = \sqrt{p/\rho}$ in time and horizontal direction. Note that the isothermal sound speed is used because the thermal conduction is much faster than the time scale of sound wave. We conventionally define temporal-

horizontal averaging operator as

$$\langle X \rangle = \frac{1}{\tau_{\rm sim} L(r)^2} \int_0^{\tau_{\rm sim}} dt \int_{x_{\rm min}}^{x_{\rm max}} dx \int_{y_{\rm min}}^{y_{\rm max}} dy X, \tag{4.23}$$

where $t = 0$ corresponds to the time the system reached the quasi-steady state. Meanwhile the rms values are calculated for transverse velocity $v_\perp = \sqrt{v_\theta^2 + v_\phi^2}$ and Elsässer variables $z_\perp^\pm = \sqrt{z_\theta^{\pm 2} + z_\phi^{\pm 2}}$:

$$v_{\perp,\rm rms} = \langle v_\theta^2 + v_\phi^2 \rangle^{1/2}, \quad z_{\perp,\rm rms}^\pm = \langle z_\theta^{\pm 2} + z_\phi^{\pm 2} \rangle^{1/2}. \tag{4.24}$$

$\tau_{\rm sim} = 3000\,{\rm s}$ is used for temporal averaging. Note that $\tau_{\rm sim}$ is larger than the longest period of upward Alfvén waves $1/f_0 = 1000\,{\rm s}$.

Figure 4.2 shows the horizontally and temporally averaged variables versus r. The left top panel shows the mass density profile. The right top panel shows the transverse velocity (black line), upward Elsässer variable (red line) and downward Elsässer variable (blue line). The left bottom panel shows the radial velocity (black line), Alfvén velocity (red line) and sound velocity (blue line). The right bottom panel shows the temperature profile in unit of 10^6 K. The wind velocity v_r and mass-loss rate $\dot{M}_w$ measured at $r = 20 R_\odot$ is

$$v_r = 591\,{\rm km\,s^{-1}}, \quad \dot{M}_w = \langle \rho v_r r^2 \rangle_{r=20R_\odot} = 1.94 \times 10^{-14}\,M_\odot\,{\rm yr^{-1}}, \tag{4.25}$$

the latter of which is comparable with the observed value $(2 - 3 \times 10^{-14}\ M_\odot\ {\rm yr}^{-1})$. The result that the maximum coronal temperature exceeds 10^6 K and that the solar wind asymptotic velocity approximates $600\,{\rm km\,s^{-1}}$ shows that the coronal heating and fast solar wind acceleration are successfully reproduced from numerical simulation, indicating the sufficient heating rate by Alfvén waves. The fact that the reduced MHD modeling cannot and compressible MHD model can explain the required heating rate proves the importance of compressibility in the solar wind.

4.3.2 Density fluctuation and enhanced wave reflection

The transverse velocity disturbance is as large as or slightly larger than the sound speed in the solar wind, indicating that Alfvén waves have potential to compress plasma and fluctuate density. Such density fluctuation can enhance the energy cascading rate up to sufficient level to sustain the solar wind (Carbone et al., 2009; van Ballegooijen & Asgari-Targhi, 2016). To understand the role of density fluctuation in wave dynamics, we calculate the density fluctuation and wave reflection rate.

The magnitude of density fluctuation is defined by the root-mean-square value of density:

$$\delta\rho = \sqrt{\langle\rho^2\rangle - \langle\rho\rangle^2}. \tag{4.26}$$

The wave reflection rate is derived as follows. We use the linearized equation for radially propagating Alfvén waves in the spherically expanding magnetic field (Heinemann & Olbert, 1980) given as

$$\begin{aligned}\left[\frac{\partial}{\partial t} + (v_r \pm V_{A,r})\frac{\partial}{\partial r}\right]\boldsymbol{z}_\pm = \boldsymbol{z}_\pm &\left[\frac{\partial}{\partial t} + (v_r \mp V_{A,r})\frac{\partial}{\partial r}\right]\ln\rho^{1/4} \\ &- \boldsymbol{z}_\mp\left[\frac{\partial}{\partial t} + (v_r \mp V_{A,r})\frac{\partial}{\partial r}\right]\ln\left(r\rho^{1/4}\right),\end{aligned} \tag{4.27}$$

where $\boldsymbol{z}_+$ and $\boldsymbol{z}_-$ denote the upward and downward Alfvén wave amplitudes, respectively. The second term in the right hand side corresponds to the reflection term. Defining the reflection rate $\omega_{\rm ref}$ as the inverse of timescale of upward-to-downward wave energy transfer, we get

$$\omega_{\rm ref} = (v_r + V_{A,r})\frac{\partial}{\partial r}\ln\left(r\rho^{1/4}\right). \tag{4.28}$$

A classical understanding is that the radial inhomogeneity of the mean solar wind density makes nonzero $\omega_{\rm ref}$, triggering reflection and turbulence (Velli et al., 1989; Matthaeus et al., 1999; Cranmer et al., 2007; Verdini et al., 2010). On the contrary, van Ballegooijen

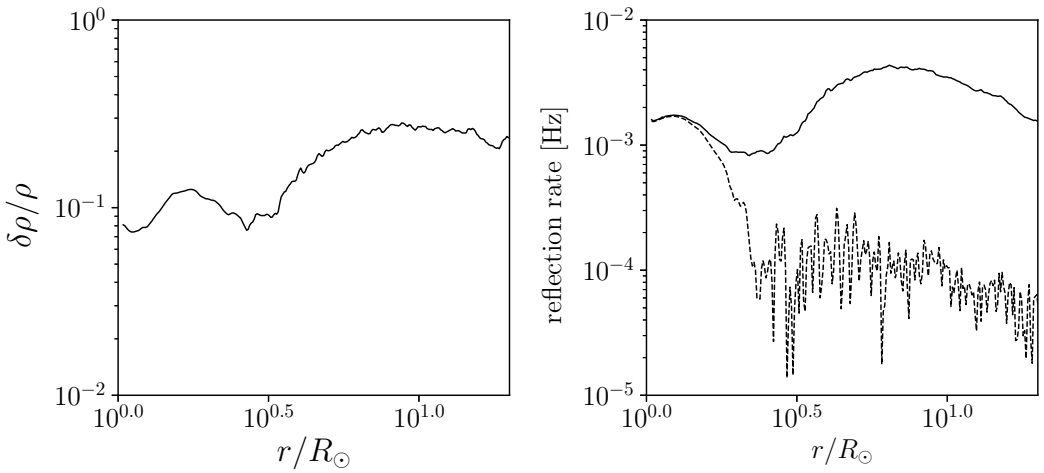

Figure 4.3: Radial profiles of the normalized density fluctuation ($\delta\rho/\langle\rho\rangle$, left panel) and reflection rates ($\omega_{\rm ref}$ and $\omega_{\rm ref,0}$, right panel). In the right panel, solid and dashed lines correspond to $\omega_{\rm ref}$ (including density fluctuation effect) and to $\omega_{\rm ref,0}$ (excluding density fluctuation effect), respectively.

& Asgari-Targhi (2016) point out the importance of density fluctuation for $\omega_{\rm ref}$. To reveal how density fluctuation enhances the reflection rate, we calculate the reflection rate with and without fluctuation as

$$\omega_{\rm ref,0} = \left(\langle v_r\rangle + \langle V_{A,r}\rangle\right) \frac{d}{dr} \ln\left(r\langle\rho\rangle^{1/4}\right), \tag{4.29}$$

$$\omega_{\rm ref} = \langle (v_r + V_{A,r}) \frac{\partial}{\partial r} \ln\left(r\rho^{1/4}\right)\rangle. \tag{4.30}$$

Figure 4.3 shows the radial profiles of density fluctuation normalized by mean value (left panel) and reflection rates with (solid line) and without (dashed line) density fluctuation (right panel). Density fluctuation in the order of 10 % of mean value is ubiquitously observed in the solar wind. Besides, the density fluctuation is observed to be maximum in the solar wind acceleration region ($r/R_\odot \lesssim 10$). These behaviors are consistent with previous observations (Carbone et al., 2009; Miyamoto et al., 2014; Hahn et al., 2018). A large gap between solid and dashed lines in the right panel directly means that the density fluctuation is a main driver of Alfvén-wave reflection. As a result, the wave reflection rate

(solid line, right panel) becomes spatially correlated with the magnitude of density fluctuation (solid line, left panel). Owing to the existence of density fluctuation, the reflection rate in the solar wind becomes approximately ten times larger. As a result, the plasma heating rate is expected to become ten times larger due to the density fluctuation, which is consistent with a previous RMHD study (van Ballegooijen & Asgari-Targhi, 2016).

The radial profile of the magnitude of density fluctuation shows several interesting behaviors. Near the coronal base, the magnitude of density fluctuation is as large as 10% of background, which is consistent with recent observation of the intensity fluctuation in the corona (Hahn et al., 2018). We should note, however, that our calculation can overestimate the density fluctuation near the bottom boundary, because the nonlinearity of Alfvén waves can be larger due to relatively smaller coronal magnetic field (2 G). The trend that the magnitude of the density fluctuation increases in the wind acceleration region is consistent with previous one-dimensional simulations and radio-wave observations Miyamoto et al. (2014).

4.3.3 Origin of density fluctuation: parametric decay instability

Now that we show the generation and role of density fluctuation in the solar wind, we discuss the physical mechanism relevant to the generation of it. Bearing in mind that the parametric decay instability (PDI) is a candidate mechanism to generate the density fluctuation, here we investigate whether the generated density fluctuations have consistent property with the theory of PDI.

According to the results in Chapter 3, the magnitude of density fluctuation is expected to be spatially correlated with the growth rate of PDI, which would support the generation of density fluctuation via PDI. The growth rate of PDI in the accelerating, expanding solar wind is given as

$$\gamma_{\rm PDI} = \tilde{\gamma}_{\rm GD} \frac{\langle v_A \rangle}{\langle v_A \rangle + \langle v_r \rangle} f_0 - 2 \left(\langle v_r \rangle + \langle a \rangle \right) / r - \frac{d}{dr} \left(\langle v_r \rangle + \langle a \rangle \right), \tag{4.31}$$

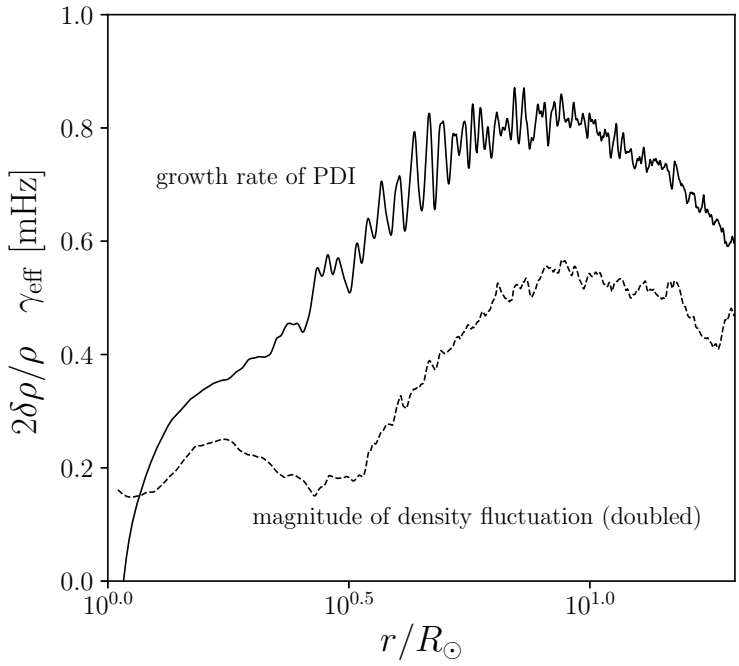

Figure 4.4: Solid line: averaged doubled fractional density fluctuation $2\delta\rho/\overline{\rho}$ versus radius. Black dashed line: effective growth rate of parametric decay instability $\gamma_{\rm PDI}$ in unit of $\rm mHz$.

where $\tilde{\gamma}_{\rm GD}$ is the normalized growth rate calculated from Goldstein–Derby dispersion relation:

$$\left(\tilde{\omega}^2 - \beta\tilde{k}^2\right)\left(\tilde{\omega} - \tilde{k}\right)\left(\tilde{\omega} + \tilde{k} - 2\right)\left(\tilde{\omega} + \tilde{k} + 2\right) = A^2\tilde{k}^2\left(\tilde{\omega}^3 + \tilde{k}\tilde{\omega}^2 - 3\tilde{\omega} + \tilde{k}\right), \tag{4.32}$$

where $\beta = a^2/v_A^2$ is plasma beta, $\tilde{\omega} = \omega/\omega_0$ and $\tilde{k} = k/k_0$ are the frequency and wave number normalized by parent wave values, and $\eta = \delta B/B_0$ is the normalized wave amplitude. The second and third terms in the right hand side correspond to the suppression by the wind expansion and acceleration, respectively.

Figure 4.4 shows the radial profiles of the relative density fluctuation (solid line) and the growth rate of parametric decay instability (solid line). For better visualization, the density fluctuation is doubled and the growth rate is shown in unit of $\rm mHz$. The trend of the solid and dashed lines are similar. Specifically, the growth rate of PDI increases in

$10^{0.5} \lesssim r/R_\odot \lesssim 10^{1.0}$, so does the magnitude of density fluctuation. This results is the first evidence that the origin of density fluctuation is PDI.

We also investigate the spatial scale of density fluctuation through auto-correlation function. For any variable X, spatial auto correlation $C_X(\boldsymbol{l})$ is defined as

$$C_X(\boldsymbol{l}) = \langle X(\boldsymbol{x}+\boldsymbol{l},t)X(\boldsymbol{x},t)\rangle \tag{4.33}$$

Since the mean magnetic field makes the turbulence anisotropic, we calculate the parallel and perpendicular auto-correlation functions as follows:

$$C_X\left(l_\parallel\right) = \langle X(\boldsymbol{x}+\boldsymbol{l}_\parallel,t)X(\boldsymbol{x},t)\rangle, \tag{4.34}$$

$$C_X(l_\perp) = \langle X(\boldsymbol{x}+\boldsymbol{l}_\perp,t)X(\boldsymbol{x},t)\rangle, \tag{4.35}$$

$$\tag{4.36}$$

where $\boldsymbol{l}_\parallel$ and $\boldsymbol{l}_\perp$ denote the parallel and perpendicular displacement vectors with respect to the mean magnetic field and $l_{\parallel,\perp} = \left|\boldsymbol{l}_{\parallel,\perp}\right|$. Note that the spatial variation scale of auto-correlation function corresponds to the spatial scale of X. Specifically, the spatial power spectrum of X is defined as the Fourier transformation of $C_X(\boldsymbol{l})$.

Figure 4.5 shows the auto-correlation functions of fractional density fluctuation $\rho/\langle\rho\rangle - 1$ (black solid line) and x-component of upward Elsässer variable z_x^+ with respect to parallel (top panel) and perpendicular (bottom panel) displacements, measured at $r/R_\odot = 10$. Both parallel and perpendicular auto-correlation functions show that density fluctuation has smaller scale than upward Elsässer variable. Given that the majority of density fluctuation comes from slow-mode waves, these results show that slow-mode waves have smaller spatial scale than upward Alfvén waves. This is consistent with the theory of PDI in that smaller-scale daughter slow-mode waves are generated from parent Alfvén waves. Therefore, the smaller scale density fluctuation is the second evidence of density fluctuation excitation by PDI.

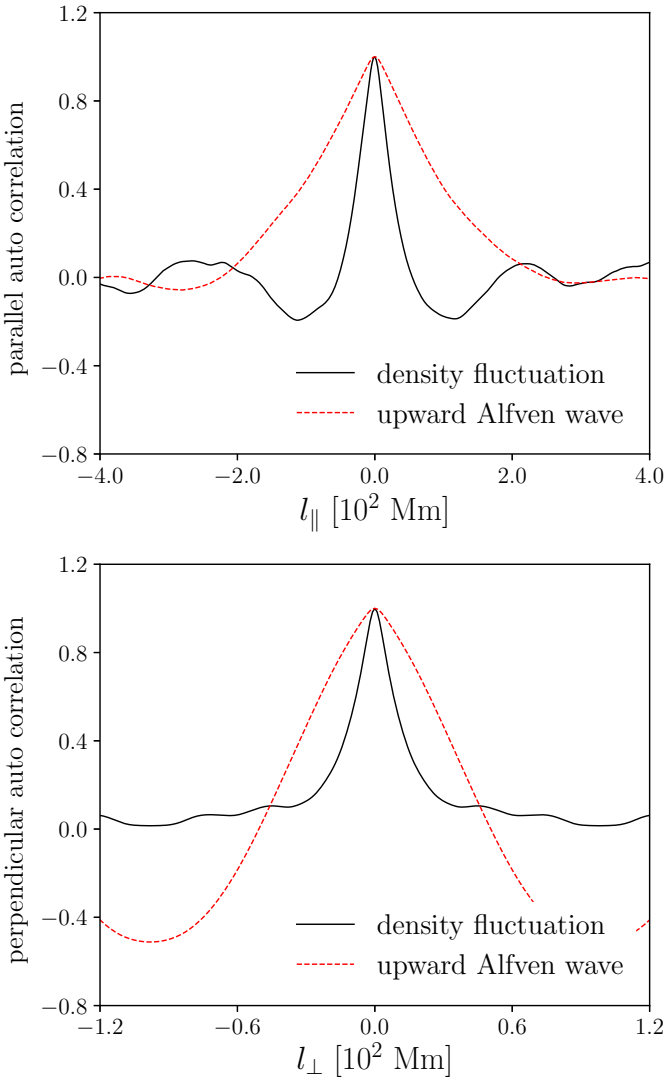

Figure 4.5: Parallel (top panel) and perpendicular (bottom panel) auto-correlation function of fractional density fluctuation $\rho/\langle\rho\rangle - 1$ (black solid line) and x-component of upward Elsässer variable z_x^+ (red dashed line), measured at $r/R_\odot = 10$ Note that the scale of x axis is different.

4.3.4 Two-dimensional slice: $r\theta$-plane

We next discuss the spatial structure in two-dimensional slices. First we focus on $r\theta$-plane to see the radial evolution of turbulence. Figure 4.6 shows a snapshot of variables in a $r\theta$-plane ($\phi = \phi_{\rm min}$) in the quasi-steady state. Shown in each panel is the relative density fluctuation $\delta\rho_{\rm hrz}/\langle\rho\rangle_{\rm hrz}$, temperature T, radial velocity v_r, upward Elsässer variable of ϕ

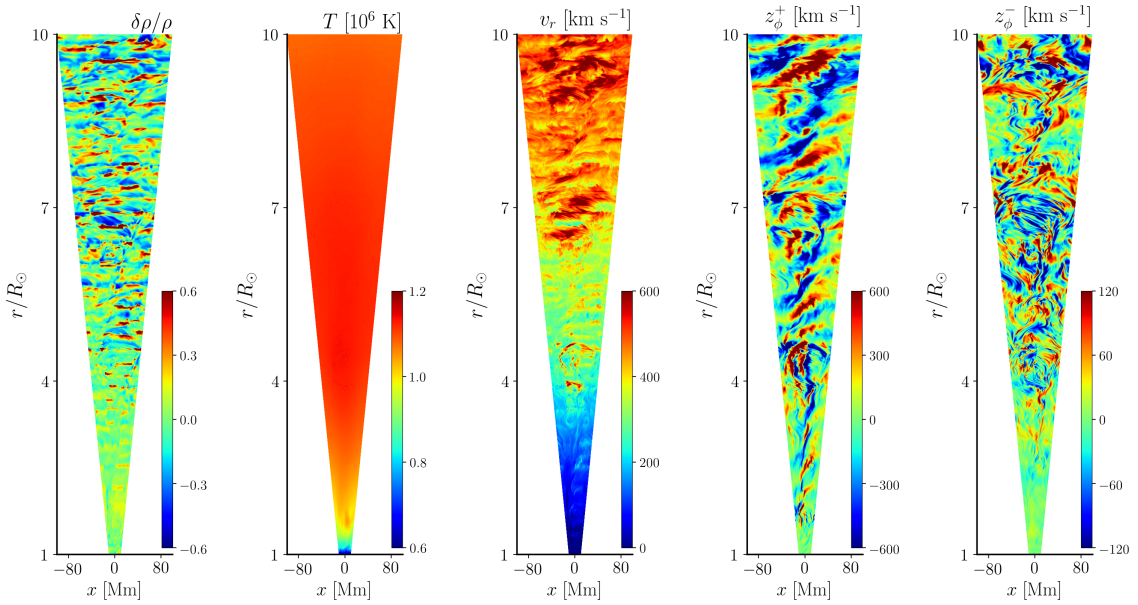

Figure 4.6: A snapshot of simulation result on $r-\theta$ plane. Displayed from left to right are the density fluctuation $(\delta\rho_{\rm hrz}/\langle\rho\rangle_{\rm hrz})$, temperature (T), radial velocity (v_r) in unit of, ϕ-component upward Elsässer variable (z_ϕ^+) and ϕ-component downward Elsässer variable (z_ϕ^-), respectively.

component z_ϕ^+ and downward Elsässer variable of ϕ component z_ϕ^-, respectively. Here $\langle\rho\rangle_{\rm hrz}$ and $\delta\rho_{\rm hrz}$ are defined as

$$\langle\rho\rangle_{\rm hrz} = \frac{1}{L(r)^2}\int_{x_{\rm min}}^{x_{\rm max}} dx \int_{y_{\rm min}}^{y_{\rm max}} dy\rho, \tag{4.37}$$

$$\delta\rho_{\rm hrz} = \rho - \langle\rho\rangle_{\rm hrz}. \tag{4.38}$$

Highly turbulent structures are observed for every variable except temperature. Note that temperature experiences fast spatial diffusion by thermal conduction that smooths the fine structures. The magnitude of density fluctuation is observed to increase in the wind acceleration region. This trend is consistent with the onset of parametric decay instability discussed in 1D simulations. What is important is that the density fluctuation is horizontally highly inhomogeneous, which triggers phase mixing in the solar wind (Shoda & Yokoyama, 2018a). An interesting feature of the solar wind turbulence is that

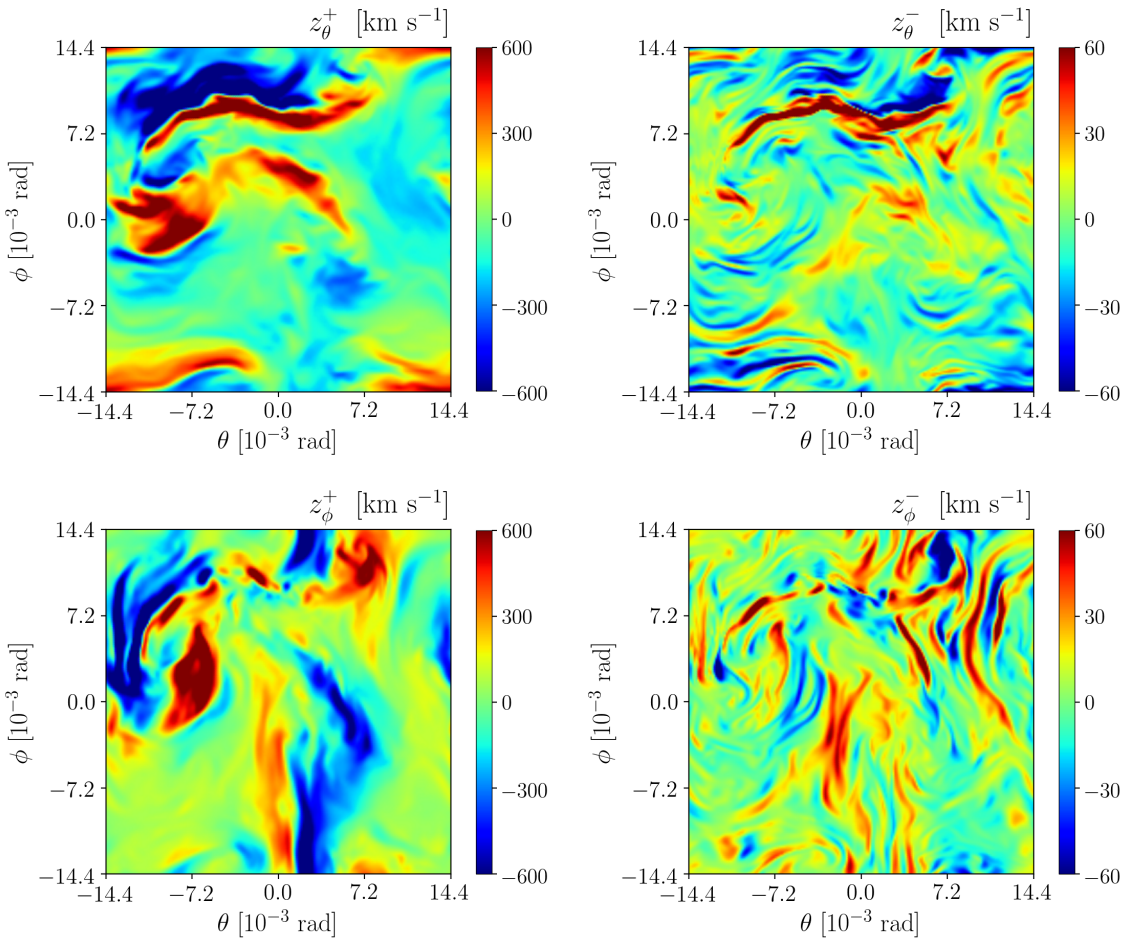

Figure 4.7: Spatial structures of Elsässer variables on the horizontal plane at $r = 3R_\odot$. The four panels correspond to z_θ^+ (left top), z_θ^- (right top), z_ϕ^+ (left bottom) and z_ϕ^- (right bottom), respectively, in unit of km s^{-1}. The corresponding color bar is shown in the right side of panel.

z_ϕ^- clearly has smaller horizontal scale than z_ϕ^+. A natural interpretation of this feature is that the cascading timescales of $z_\phi^\pm$ are different; when the cascading of z_ϕ^- proceeds faster than z_ϕ^+, the smaller structure is expected to be more apparent for z_ϕ^-.

4.3.5 Two-dimensional slice: $\theta\phi$-plane

For more detailed investigation of the scale difference between and outward and inward Alfvén waves and the radial evolution of it, the horizontal profiles of $z^\pm$ are discussed

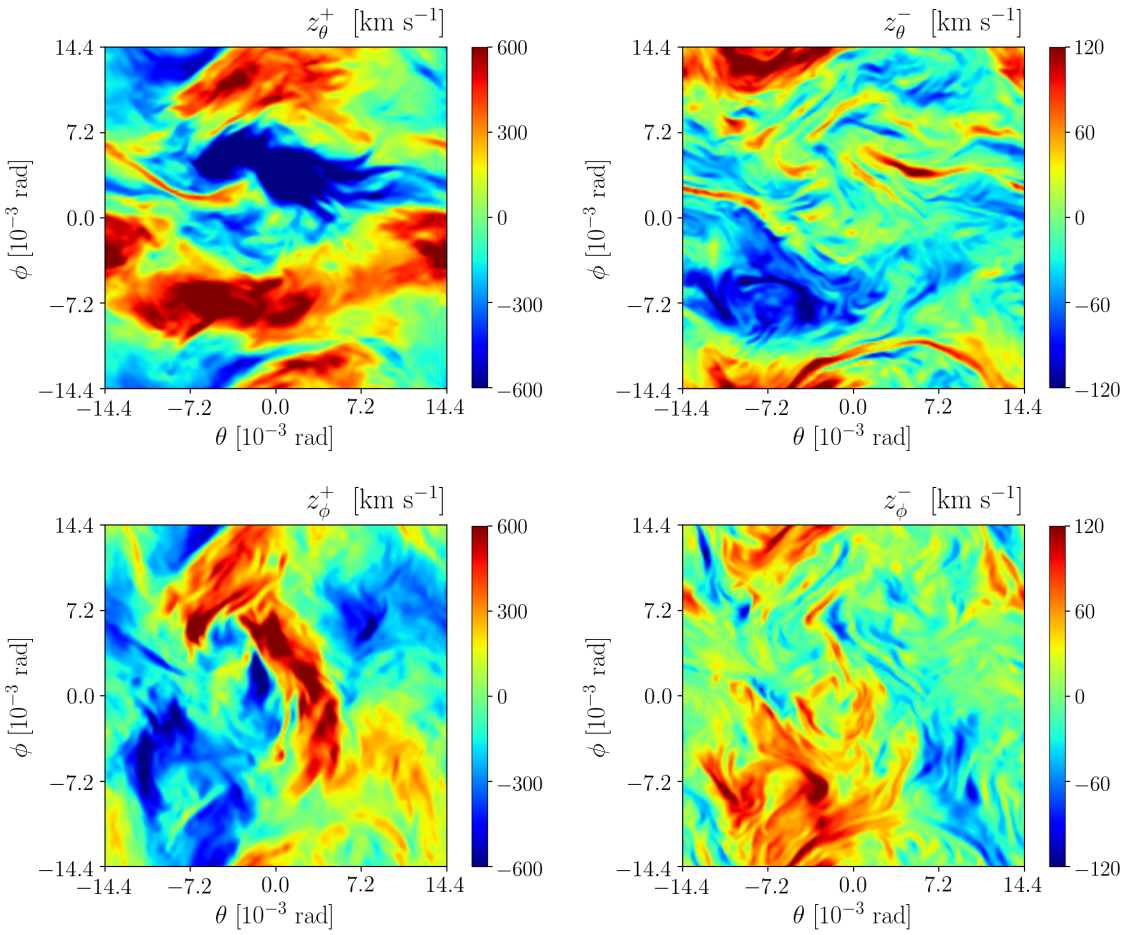

Figure 4.8: Same as Figure 4.7 but at $r = 20R_\odot$. Note that the color bar of inward Elsässer variables $z^-_{\theta,\phi}$ are different from Figure 4.7.

here. Figures 4.7 and 4.8 show the horizontal structures of Elsässer variables ($z^\pm_\theta$, $z^\pm_\phi$) at $r = 3R_\odot$ and $r = 20R_\odot$, respectively. The difference in spatial structures of outward and inward Elsässer variables is observed in both Figures. Furthermore, the difference is more significant in the inner region.

To see the scale difference more quantitatively, we calculate the power spectra of inward and outward Elsässer energies $E^\pm$ with respect to perpendicular wave number,

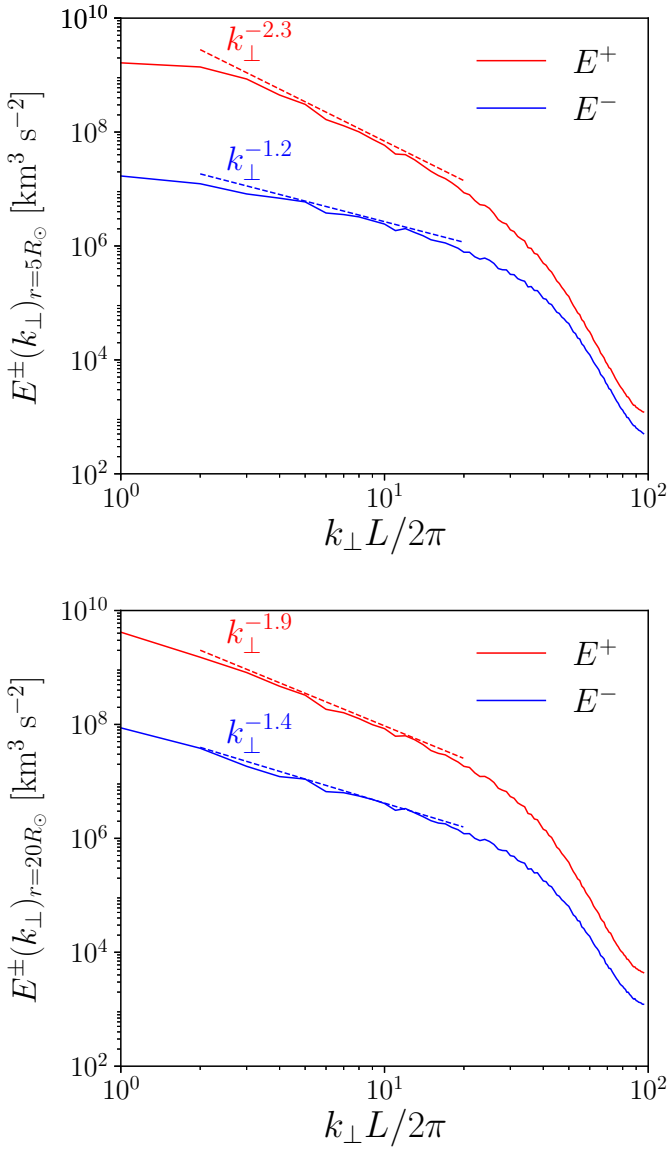

Figure 4.9: Power spectra of outward (E^+, red solid line) and inward (E^-, blue solid line) Elsässer energies at $r = 5R_\odot$ (top panel) and $r = 20R_\odot$ (bottom panel). Also shown by dashed lines are the power-law fittings in the inertial range.

defined as

$$E^{\pm}\left(k_\perp\right)_{r=r_0} = \frac{1}{\Delta k_\perp} \sum_{k_\perp < \sqrt{k_x^2+k_y^2} < k_\perp + \Delta k_\perp} \left[\left| z_\theta^{\pm}(r_0, k_x, k_y) \right|^2 + \left| z_\phi^{\pm}(r_0, k_x, k_y) \right|^2 \right], \tag{4.39}$$

where $z^{\pm}_{\theta,\phi}$ are the Fourier components of Elsässer variables:

$$z^{\pm}_{\theta}(r_0, k_x, k_y) = \frac{1}{L(r_0)^2} \int_{x_{\min}}^{x_{\max}} dx \int_{y_{\min}}^{y_{\max}} dy \ \exp\left[i\left(k_x x + k_y y\right)\right] z^{\pm}_{\theta}(r_0, x, y), \quad (4.40)$$

$$z^{\pm}_{\phi}(r_0, k_x, k_y) = \frac{1}{L(r_0)^2} \int_{x_{\min}}^{x_{\max}} dx \int_{y_{\min}}^{y_{\max}} dy \ \exp\left[i\left(k_x x + k_y y\right)\right] z^{\pm}_{\phi}(r_0, x, y), \quad (4.41)$$

where $x_{\max,\min} = r_0\theta_{\max,\min}$ and $y_{\max,\min} = r_0\phi_{\max,\min}$.

Figure 4.9 shows the Elsässer energy spectrum with respect to normalized perpendicular wave number. Red and blue solid lines indicate the outward and inward Elsässer energies. Top and bottom panels correspond to the spectra in $r = 5R_\odot$ and $r = 20R_\odot$, respectively. For smoothing, we averaged the spectra in time. Also shown by dashed lines are the power-law fittings in the inertial range. As the fitted lines indicate, the inclinations of red and blue lines in the inertial range are different; the outward Elsässer energy spectrum always show steeper slope in the inertial range than the inward one. Further interesting feature is that the difference of the inclination of slope reduces as waves get far from the Sun. Figure 4.10 shows the radial evolution of spectral indices of outward (red) and inward (blue) Elsässer energy spectra. The two indices approach each other as radial distance gets larger. It is interesting to note that the average of the two yields Kolmogorov's $5/3$ index, indicating that both spectra would be Kolmogorov-type in the sufficiently distant heliosphere.

The difference in power spectra is consistent with theory of imbalanced MHD turbulence. In the regime of Alfvén wave turbulence, the cascading timescale of outward Alfvén wave is controlled by the amplitude of inward Alfvén wave, and vice versa. Thus when the energies of outward and inward Alfvén waves are different (i.e., the turbulence is imbalanced), the cascading timescales are also different. This property leads to the relaxation process called dynamical alignment (Dobrowolny et al., 1980; Stribling & Matthaeus, 1991; Hossain et al., 1995). In terms of spectrum, the difference in cascading timescale appears in the difference in power spectrum (Boldyrev & Perez, 2009; Perez et al., 2012; Verdini et al., 2012a).

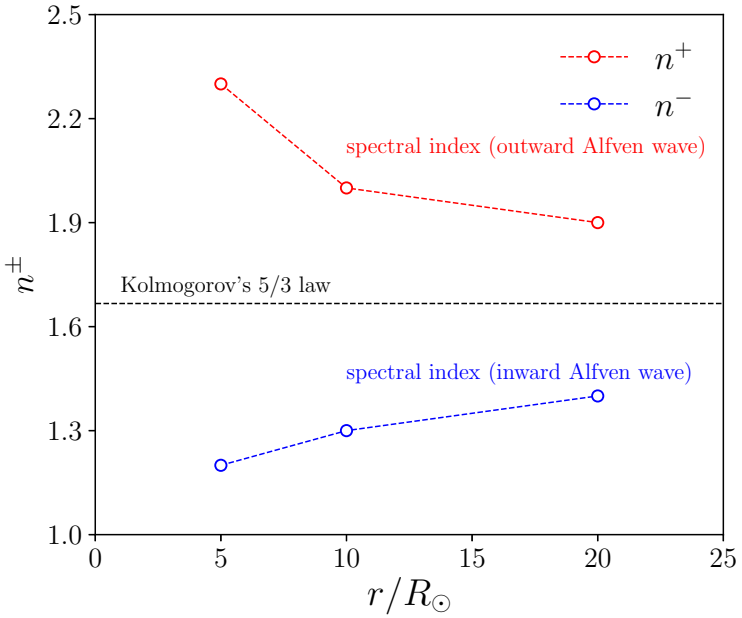

Figure 4.10: Spectral power indices of outward (n^+, red) and inward (n^-, blue) Elsässer energy spectra. Also shown by black dashed line represents the index of Kolmogorov's law.

4.3.6 Anisotropy of turbulence

Turbulence in the solar wind is expected to be anisotropic, because the energy of mean field should be larger than those of fluctuating components. The anisotropy appears both in power spectrum (Goldreich & Sridhar, 1995) and structure function (Cho & Lazarian, 2003; Verdini et al., 2015). Since the Fourier transformation is not applicable to inhomogeneous system, we discuss the anisotropy of turbulence using structure function.

For any variables $\boldsymbol{X}$, corresponding nth-order structure function SF_n is defined as

$$SF_n(\boldsymbol{l}) = \langle |\boldsymbol{X}(\boldsymbol{x}+\boldsymbol{l}) - \boldsymbol{X}(\boldsymbol{x})|^n \rangle_{\text{statistical}}, \tag{4.42}$$

where $\langle X \rangle_{\text{statistical}}$ denotes the statistical average. Practically, $\langle X \rangle_{\text{statistical}}$ means the average in time and transverse direction. Here we calculate the second-order structure function

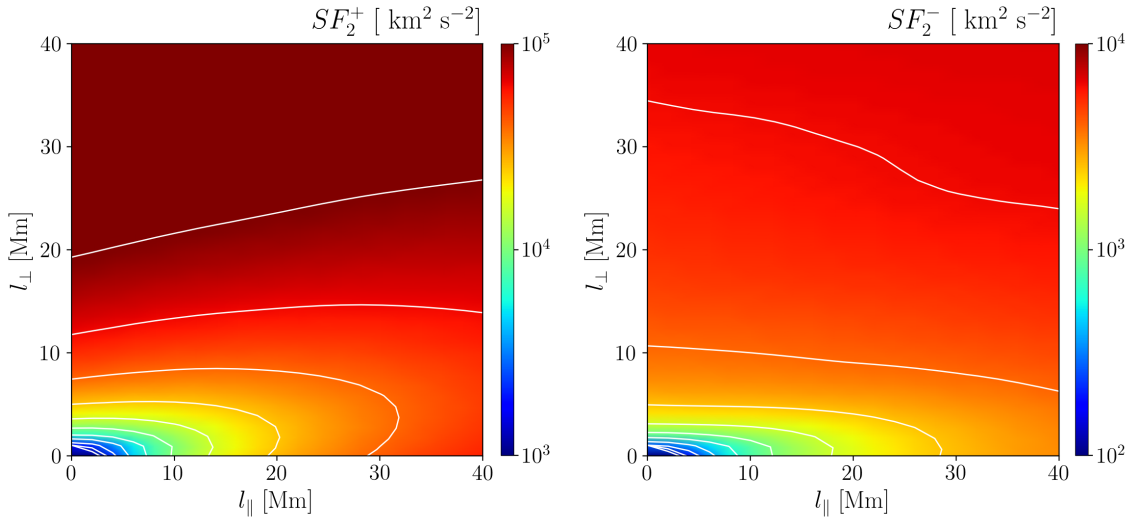

Figure 4.11: Second-order structure functions of upward (left panel) and downward (right panel) Elsässer variables measured at $r = 10R_\odot$. Shown by white lines are contour lines.

of upward and downward Elsässer variables:

$$SF_2^+(\boldsymbol{l}) = \left\langle \left| \boldsymbol{z}_\perp^+(\boldsymbol{x}+\boldsymbol{l}) - \boldsymbol{z}_\perp^+(\boldsymbol{x}) \right|^2 \right\rangle_{\text{statistical}}, \tag{4.43}$$

$$SF_2^-(\boldsymbol{l}) = \left\langle \left| \boldsymbol{z}_\perp^-(\boldsymbol{x}+\boldsymbol{l}) - \boldsymbol{z}_\perp^-(\boldsymbol{x}) \right|^2 \right\rangle_{\text{statistical}}. \tag{4.44}$$

For simplicity, we assume axisymmetry with respect to mean magnetic field, that is, r axis. The structure function is then calculated as

$$SF_2^+(l_\parallel, l_\perp) = \left\langle \left| \boldsymbol{z}_\perp^+\left(\boldsymbol{x} + l_\perp\hat{\boldsymbol{\theta}} + l_\parallel\hat{\boldsymbol{r}}\right) - \boldsymbol{z}_\perp^+(\boldsymbol{x}) \right|^2 \right\rangle_{\text{statistical}}, \tag{4.45}$$

$$SF_2^-(l_\parallel, l_\perp) = \left\langle \left| \boldsymbol{z}_\perp^-\left(\boldsymbol{x} + l_\perp\hat{\boldsymbol{\theta}} + l_\parallel\hat{\boldsymbol{r}}\right) - \boldsymbol{z}_\perp^-(\boldsymbol{x}) \right|^2 \right\rangle_{\text{statistical}}, \tag{4.46}$$

where $\hat{\boldsymbol{\theta}}$ and $\hat{\boldsymbol{r}}$ denote the unit vector in θ and r directions, respectively.

Figure 4.11 shows the second-order structure function of upward and downward Elsässer variables $SF_2^\pm$ measured at $r = 10R_\odot$. Also shown by white lines are contour lines of structure functions. The fact that the contours of both structure functions are elongated along $l_\parallel$ axis shows that the turbulence is anisotropic with smaller scales generated in the

perpendicular direction (Cho & Lazarian, 2003). Note that the structure function becomes smaller when the amplitude and phase of $\boldsymbol{z}^{\pm}$ are more similar between $\boldsymbol{x}$ and $\boldsymbol{x}+\boldsymbol{l}$. Therefore, the elongated structure along $l_{\parallel}$ axis means the phase of wave is more constant in parallel direction.

4.3.7 Plasma heating mechanism

One important result in Chapter 3 is the decomposition of heating rate into shock and turbulence heating rates. A similar analysis is applicable to 3D simulation by comparing the perpendicular cascading rate (that is modeled phenomenologically in 1D simulations) with the total heating rate.

Difficulty lies in the calculation of cascading rate. Here we calculate the third-order structure function (Yaglom's flux) to derivate the perpendicular cascading rate from simulation data. First, we assume that the dynamics of Alfvén waves and perpendicular cascading are described in the framework of reduced MHD. Under this assumption, the cascading rate is derivable from the equation of second-order Elsässer structure functions defined as

$$SF_2^{\pm}(\boldsymbol{l}) = \langle \left|\Delta \boldsymbol{z}_{\perp}^{\pm}(\boldsymbol{l},\boldsymbol{x},t)\right|^2 \rangle_{\text{statistical}}, \tag{4.47}$$

where $\langle X \rangle_{\text{statistical}}$ means the statistical average of X and

$$\Delta \boldsymbol{z}_{\perp}^{\pm}(\boldsymbol{l},\boldsymbol{x},t) = \boldsymbol{z}_{\perp}^{\pm}(\boldsymbol{x}+\boldsymbol{l},t) - \boldsymbol{z}_{\perp}^{\pm}(\boldsymbol{x},t), \tag{4.48}$$

$$\boldsymbol{z}_{\perp}^{\pm} = \boldsymbol{v}_{\perp} \mp \boldsymbol{B}_{\perp}/\sqrt{4\pi\rho}. \tag{4.49}$$

The time evolution of the second-order structure function is given as (Politano & Pouquet, 1998; Carbone et al., 2009; Verdini et al., 2015)

$$\frac{\partial}{\partial t}\langle \left|\Delta \boldsymbol{z}_{\perp}^{\pm}\right|^2 \rangle + \nabla_{\boldsymbol{l}} \cdot \langle \Delta \boldsymbol{z}_{\perp}^{\mp} \left|\Delta \boldsymbol{z}_{\perp}^{\pm}\right|^2 \rangle = -\Pi - \Lambda + 2\nu\nabla_{\boldsymbol{l}}^2 \langle \left|\Delta \boldsymbol{z}_{\perp}^{\pm}\right|^2 \rangle - 8\varepsilon^{\pm}, \tag{4.50}$$

where a statistical average is denoted by simple bracket for simplicity. Π and Λ correspond to pressure and sweeping terms, both of which are ignorable for nearly homogeneous turbulence. $\varepsilon^{\pm}$ stands for the cascading rate of $\langle \left|\boldsymbol{z}_{\perp}^{\pm}\right|^2/4\rangle$. In a quasi-steady state, when the scale of interest is much smaller than the scale length of background and much larger than the viscous damping scale, the cascading rate is expressed by

$$\varepsilon^{\pm} = -\frac{1}{8}\nabla \cdot \boldsymbol{Y}^{\pm}, \quad \boldsymbol{Y}^{\pm} = \langle \Delta \boldsymbol{z}_{\perp}^{\mp} \left|\Delta \boldsymbol{z}_{\perp}^{\pm}\right|^2 \rangle. \tag{4.51}$$

where $\nabla_{\boldsymbol{l}}$ is replaced by ∇ and $\boldsymbol{Y}^{\pm}$ is called Yaglom's flux. We are interested in the estimation of perpendicular cascading rate $\varepsilon^{\pm}$. A natural definition of perpendicular cascading rate is given by the perpendicular divergence of Yaglom's flux (Verdini et al., 2015):

$$\varepsilon_{\perp}^{\pm} = -\frac{1}{8}\nabla_{\perp} \cdot \boldsymbol{Y}^{\pm}. \tag{4.52}$$

A further simplification is available from the assumption of axisymmetry as

$$Y_{\perp}^{\pm}(l_{\perp}) = -4\varepsilon_{\perp}^{\pm} l_{\perp}, \tag{4.53}$$

where

$$Y_{\perp}^{\pm}(l_{\perp}) = \boldsymbol{Y}^{\pm}(\boldsymbol{l}_{\perp}) \cdot \frac{\boldsymbol{l}_{\perp}}{l_{\perp}}. \tag{4.54}$$

To compare with the cascading rate, we also calculate the total heating rate from the energy equation expressed as

$$\frac{\partial}{\partial t}e + v_r \frac{\partial e}{\partial r} + \frac{e+p}{r^2}\frac{\partial}{\partial r}\left(v_r r^2\right) = Q_{\mathrm{tot}} + Q_{\mathrm{cnd}}, \tag{4.55}$$

where we ignore the derivatives in θ and ϕ. In a quasi-steady state, averaged total heating

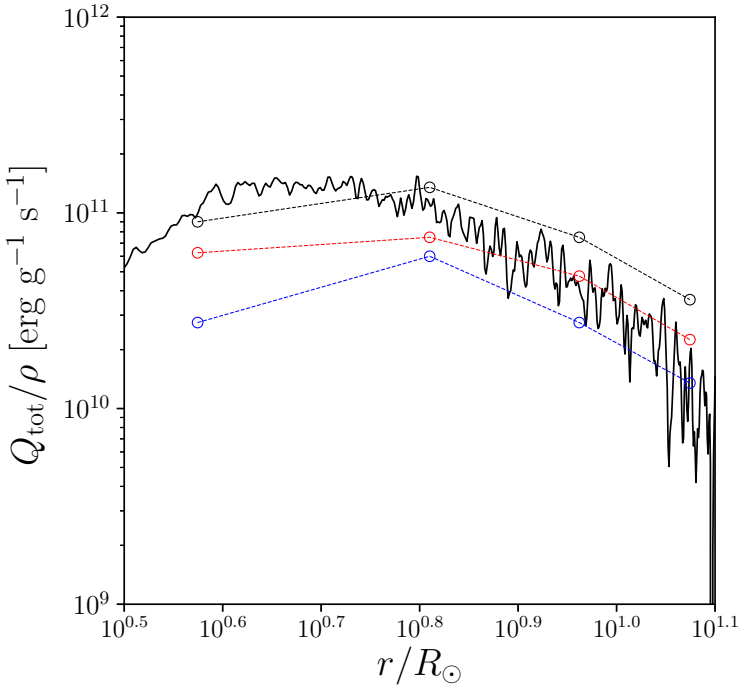

Figure 4.12: Total heating rate $Q_{\rm tot}$ divided by density (black solid line) and perpendicular cascading rates of upward Alfvén wave ($\varepsilon_\perp^+$, blue dashed line), downward Alfvén wave ($\varepsilon_\perp^-$, red dashed line), and summation of the two ($\varepsilon_\perp^+ + \varepsilon_\perp^-$, black dashed line).

rate is deduced as

$$Q_{\rm tot} = v_r \frac{\partial e}{\partial r} + \frac{e+p}{r^2}\frac{\partial}{\partial r}\left(v_r r^2\right) - Q_{\rm cnd}. \tag{4.56}$$

Here we use the temporally and horizontally averaged values to calculate $Q_{\rm tot}$. In Figure 4.12, we compare the total heating rate per unit mass $Q_{\rm tot}/\rho$ with cascading rates $\varepsilon_\perp^\pm$ derived from Yaglom's flux. The total perpendicular cascading rate is almost the same as the total heating rate, indicating that almost all the heat is supplied by perpendicular cascading. The cascading rate has a certain error, which should be the main cause of the unrealistic situation that the cascading rate is larger than the heating rate.

4.3.8 Prediction for Parker Solar Probe

Since the simulation domain extends beyond the nearest perihelion of *Parker Solar Probe* (hereafter *PSP*), we can directly provide the expected data based on the following procedure. Given the velocity of *PSP* in θ and ϕ directions, the position $(x_{PSP}, y_{\rm PSP})$ is calculated as

$$x_{PSP} = x_{PSP,0} + v_{PSP,\theta}\, t, \tag{4.57}$$

$$y_{PSP} = y_{PSP,0} + v_{PSP,\phi}\, t. \tag{4.58}$$

Then the expected observations are given as the value at $(r_0, x_{PSP}, y_{PSP}, t)$. For example, observed density at $r = r_0$ ($\rho_{PSP,r_0}(t)$) is given as

$$\rho_{PSP,r_0}(t) = \rho\left(r_0, x_{PSP}, y_{PSP}, t\right). \tag{4.59}$$

Figure 4.13 and 4.14 show the predicted *PSP* data at $r = 10R_\odot$ and $r = 20R_\odot$, respectively. The first prediction is that, both at $r = 10R_\odot$ and $r = 20R_\odot$, large density fluctuation in the order of 10% of the mean value is expected to be observed. Note that this is a direct consequence of parametric decay instability. Another interesting prediction is that the timescales of variation are different in $r = 10R_\odot$ and $r = 20R_\odot$. Predicted data at $r = 20R_\odot$ shows longer timescale of fluctuations, possibly because the crossing time over a turbulent vortex ($L/v_{\rm PSP}$ where L is the size of vortex and $v_{\rm PSP}$ is the velocity of *PSP*) is longer in $r = 20R_\odot$ because L is approximately proportional to r and $v_{\rm PSP}$ is smaller for larger r.

A unique point of our model is that we predict the in-situ generation of slow-mode waves in the solar wind possibly via parametric decay instability. We therefore expect that *PSP* would observe a signature of large-amplitude slow-mode waves in the solar wind. Such data can be predicted from our simulation. Since the plasma beta in the solar wind is lower than unity, slow-mode waves are essentially equivalent with acoustic waves propagating along magnetic field. In the linear regime, parallel slow-mode waves satisfy

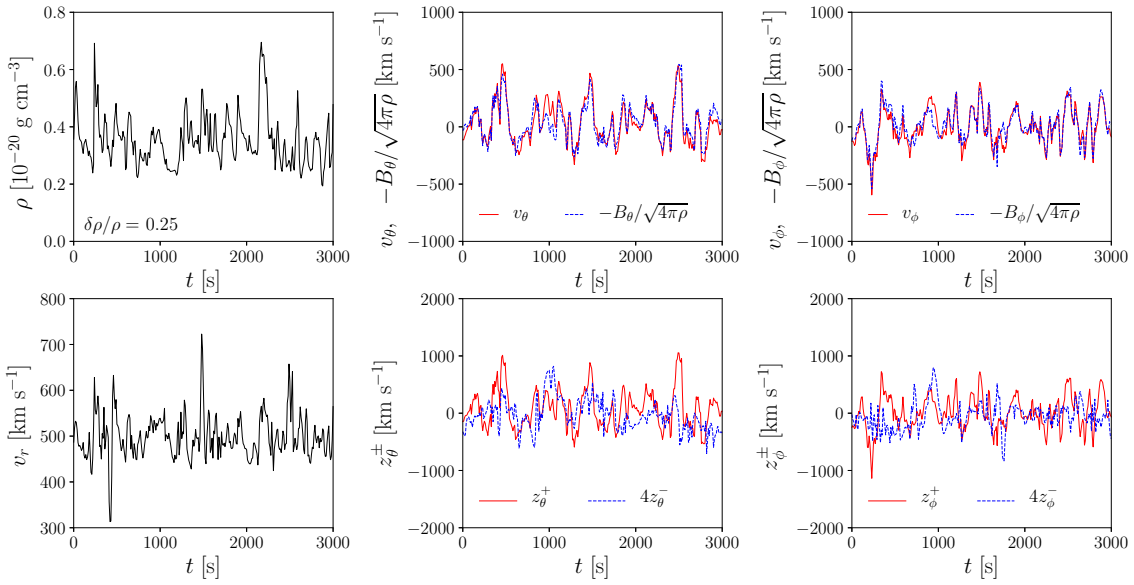

Figure 4.13: Predicted data of *Parker Solar Probe* in the radial distance of $r = 10R_\odot$ with *PSP* velocity $192\ \mathrm{km\ s^{-1}}$. Shown in the top panels from left to right are the density, v_θ (red solid line) and $-B_\theta/\sqrt{4\pi\rho}$ (blue dashed line), and v_ϕ (red solid line) and $-B_\phi/\sqrt{4\pi\rho}$ (blue dashed line), respectively. Shown in the bottom panels from left to right are the radial velocity v_r, z_θ^+ (red solid line) and $4z_\theta^-$ (blue dashed line), and z_ϕ^+ (red solid line) and $4z_\phi^-$ (blue dashed line), respectively. Also shown in the left bottom of the density panel is the normalized density fluctuation calculated from the time series data.

a characteristic relation as

$$\delta\rho/\rho = \delta v_\parallel/a, \tag{4.60}$$

where δ denotes the fluctuation and a stands for sound speed.

To confirm this relation, we calculate the fluctuation of density and parallel velocity from synthesized *PSP* data. Let $\rho_{PSP}(t)$, $\boldsymbol{v}_{PSP}(t)$ and $\boldsymbol{B}_{PSP}(t)$ be the predicted time-series data for density, velocity and magnetic field, respectively. We first calculate the

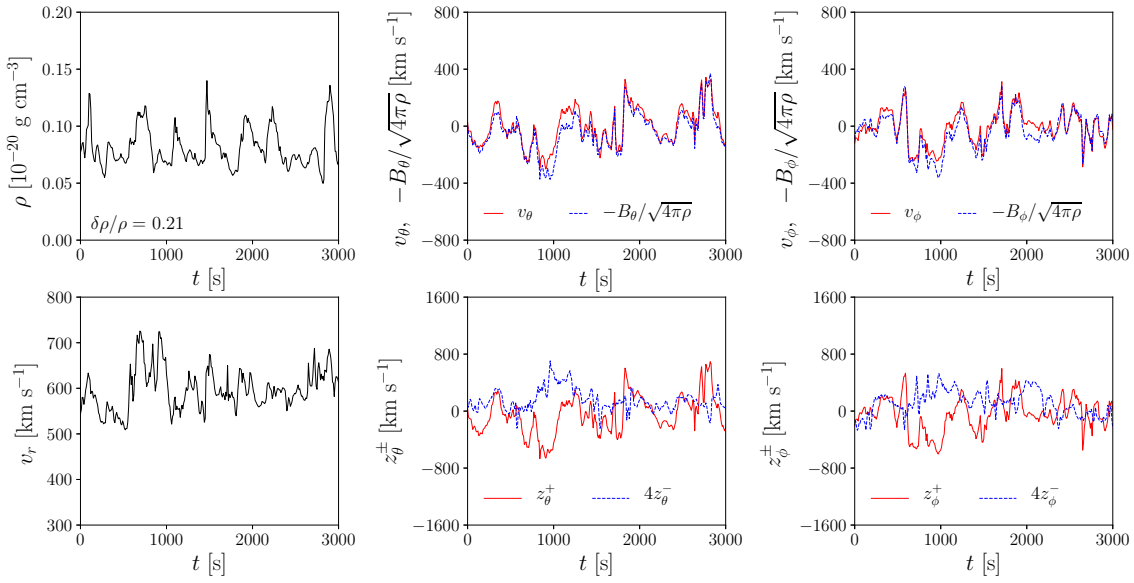

Figure 4.14: Same as Figure 4.13 but at $r = 20R_\odot$ with *PSP* velocity 129 km s^{-1}.

mean values as

$$\overline{\rho}_{PSP} = \frac{1}{\tau}\int_0^\tau dt\ \rho_{PSP}(t), \tag{4.61}$$

$$\overline{\boldsymbol{v}}_{PSP} = \frac{1}{\tau}\int_0^\tau dt\ \boldsymbol{v}_{PSP}(t), \tag{4.62}$$

$$\overline{\boldsymbol{B}}_{PSP} = \frac{1}{\tau}\int_0^\tau dt\ \boldsymbol{B}_{PSP}(t), \tag{4.63}$$

where τ is the observation period. The density and velocity fluctuations are defined as

$$\delta\rho_{PSP}(t) = \rho_{PSP}(t) - \overline{\rho}_{PSP}, \tag{4.64}$$

$$\delta\boldsymbol{v}_{PSP}(t) = \boldsymbol{v}_{PSP}(t) - \overline{\boldsymbol{v}}_{PSP}. \tag{4.65}$$

Since the slow-mode waves are associated with field-aligned velocity fluctuation, we deduce the field-aligned component as

$$\delta v_{\parallel,PSP}(t) = \delta\boldsymbol{v}_{PSP}(t)\cdot\boldsymbol{B}_{PSP}(t)/\left|\boldsymbol{B}_{PSP}(t)\right|. \tag{4.66}$$

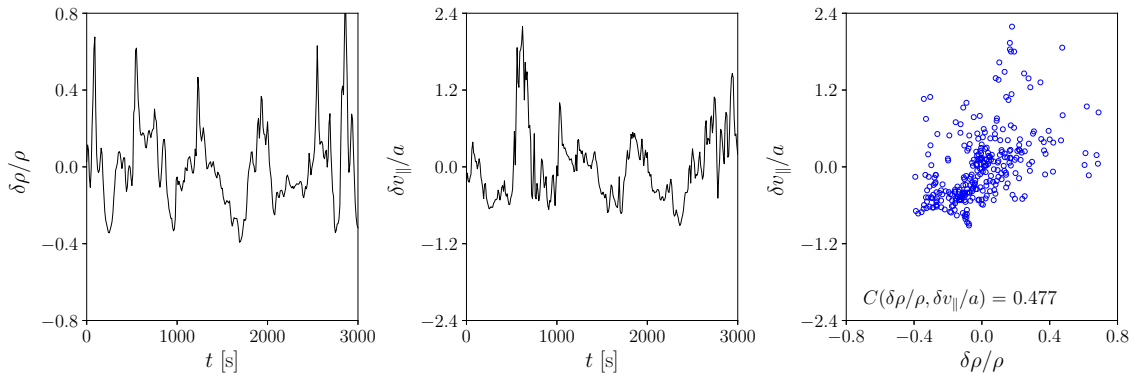

Figure 4.15: Density and parallel-velocity fluctuations predicted for *Parker Solar Probe* at $r = 20R_\odot$ with *PSP* velocity $200\ \mathrm{km\ s^{-1}}$. Left: time series of fractional density fluctuation. Middle: time series of parallel-velocity fluctuation normalized by sound speed a. Right: scatter plot between density and parallel-velocity fluctuations.

Figure 4.15 shows the synthesized data for normalized density fluctuation $\delta\rho_{PSP}(t)/\overline{\rho}_{PSP}$ (left panel), parallel-velocity fluctuation $\delta v_{\parallel,PSP}(t)/a$ (middle panel) and the scatter plot between the two variables (right panel). The scatter plot shows a positive correlation with correlation coefficient 0.477 between the fluctuations of density and parallel velocity, indicating the presence of slow-mode waves. Several factors are responsible for the scatter in the right panel, including the contamination of the other wave modes, the oblique propagation and nonlinear effects. A positive correlation shows that the major component of parallel-velocity fluctuation is the slow-mode waves, thus showing the slow-mode wave generation in the solar wind.

To study turbulence via spacecraft observation, the most fundamental information would be the power spectrum measure in the frame of spacecraft. We here predict the power spectrum to be observed by *PSP*. Among several variables that we can define the power spectrum, such as velocity, magnetic field, etc., we focus on the inward Elsässer energy. The reason is as follows. Outward Alfvén waves experience weak turbulence during the propagation from the bottom to top, thus preserving the information of bottom boundary condition, which is to some degree artificial. Since the outward Alfvén waves

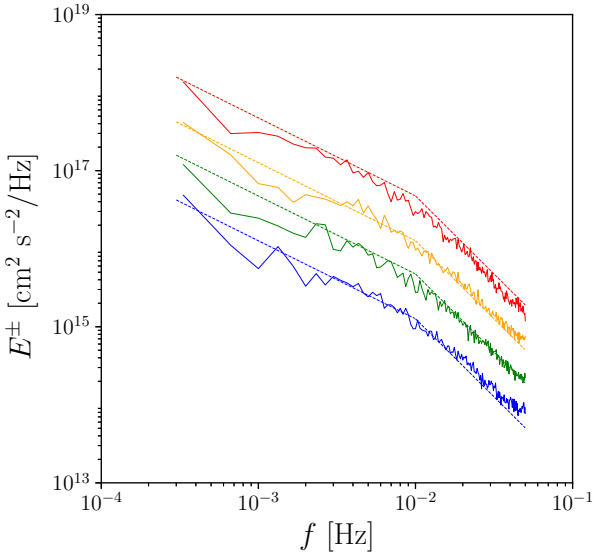

Figure 4.16: Power spectrum of inward Elsässer energy measured in the frame of spacecraft. Four lines correspond to the spacecraft velocity of $0\ \mathrm{km\ s^{-1}}$ (red), $67\ \mathrm{km\ s^{-1}}$ (orange), $133\ \mathrm{km\ s^{-1}}$ (green) and $200\ \mathrm{km\ s^{-1}}$ (blue), respectively. Red, orange and green lines are scaled upward by factors of $10^{1.5}$, $10^{1.0}$ and $10^{0.5}$, respectively. Dashed lines are the fitted lines to the solid lines with double-power law (f^{-1} and f^{-2}) with the break point 10^{-2} Hz.

are a main component of solar wind fluctuation, the same difficulty arises for velocity and magnetic field. While the inward Alfvén waves are generated within the simulation box and experience strong turbulent mixing that would extinguish artificial informations.

From the time-series of *PSP* data, we calculate the power spectrum of inward Elsässer energy. In doing so, we vary the velocity of *PSP* to investigate how the output varies with respect to spacecraft velocity. Figure 4.16, we plot the spectrum of inward Elsässer energy measured at $r/R_\odot = 11.9$. Four solid lines indicate the spectrum with *PSP* velocity $0\ \mathrm{km\ s^{-1}}$ (red), $67\ \mathrm{km\ s^{-1}}$ (orange), $133\ \mathrm{km\ s^{-1}}$ (green) and $200\ \mathrm{km\ s^{-1}}$ (blue), respectively. For better visualization, red, orange and green lines are scaled upward by factors of $10^{1.5}$, $10^{1.0}$ and $10^{0.5}$, respectively. Also shown by dashed lines are double-power fits to the solid lines. The lower- and higher-frequency regions are fitted by f^{-1} and f^{-2} power laws with break point 10^{-2} Hz. Regardless of *PSP* velocity, the power spectrum can be

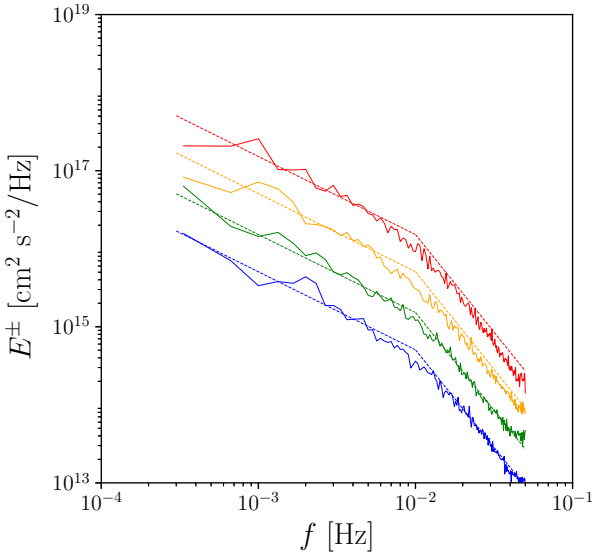

Figure 4.17: Same as Figure 4.16. Here dashed lines are a double-power law (f^{-1} and $f^{-2.5}$) with the break point 10^{-2} Hz.

approximated by the same double power law. According to Verdini et al. (2012a), the spectral break point comes from the energy injection scale. Our result is consistent with this interpretation because the highest-frequency waves that are injected from the bottom boundary is 10^{-2} Hz. Thus, we expect that *PSP* would find a double power law of inward Elsässer energy with the knee point corresponding to the energy injection scale.

A similar analysis is conducted for the data in $r/R_\odot = 20$. Figure 4.17 shows the same analysis as Figure 4.16 in $r/R_\odot = 20$. The fitted lines here are the double power law with lower side f^{-1}, higher side $f^{-2.5}$ and knee point 10^{-2} Hz. The spectral break occurs at the same frequency as the data in $r/R_\odot = 11.9$, suggesting that the break point is not determined by the local dynamics. The spectrum in the higher-frequency part shows steeper profile than that of $r/R_\odot = 11.9$. One possibility is that the numerical dissipation works stronger in the distant region to make a steeper profile. However, the spectrum knee point is a robust property and therefore would be an appropriate observational target for *PSP*.

4.4 Discussion

4.4.1 Plasma heating scenario

One of the most important motivations through this thesis is to clarify the plasma heating process in the solar wind. Summarizing the results in this Chapter, we given an answer to this question.

First, we have reproduced the fast solar wind with realistic termination velocity, mass-loss rate and coronal temperature (Figure 4.2). Therefore our simulation is nothing but a numerical demonstration that the fast solar wind is driven by Alfvén waves injected from the bottom.

Next, the dominant wave dissipation (or plasma heating) mechanism is likely to be Alfvén wave turbulence that are triggered by the collision of bi-directional Alfvén waves. Anisotropy of structure function (Figure 4.11) and the comparison between heating and perpendicular cascading rate (Figure 4.12) support this idea. The Alfvén wave turbulence in the solar wind can be described in the framework of reduced (incompressible) MHD.

This does not mean the compressibility has no role. By considering compressibility, large density fluctuations are excited, which drastically enhance the wave reflection rate (Figure 4.3). Since the wave reflection is the source for Alfvén wave turbulence, this means that compressibility and resultant density fluctuation activates turbulence. The origin of density fluctuation is shown to be the parametric decay instability, through the analysis of growth rate (Figure 4.4) and spatial structure (Figure 4.5).

A summary is as follows. Alfvén waves are subject to parametric decay instability, leading to the generation of density fluctuation. Enhanced wave reflection by density fluctuation promotes Alfvén wave turbulence and perpendicular cascading, which is a dominant heating mechanism in the solar wind.

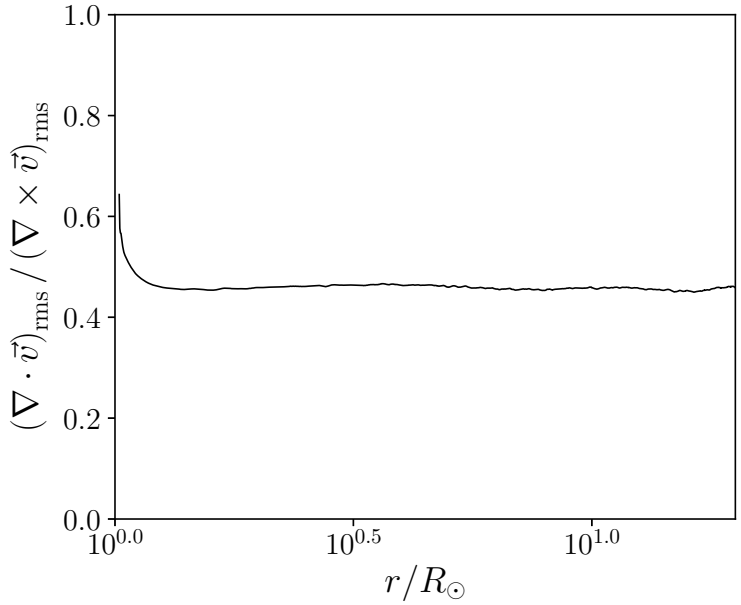

Figure 4.18: Root-mean-squared divergence-to-rotation ratio of velocity in the solar wind.

4.4.2 Parametric decay instability in an open system

One characteristic of the solar wind is that it is an open system. It affects the physics of parametric decay instability for following reason. The wave-wave interaction or resonance is an essence of parametric decay instability. In a periodic system, one wave can interact with another wave until the instability reaches a saturation phase, while in a open system, the interacting time between waves are limited as

$$\tau_{1-2} = (\lambda_1 + \lambda_2) \,/\, |c_1 - c_2| \,, \tag{4.67}$$

where τ_{1-2} denotes the interacting time between wave 1 and 2. $\lambda_{1,2}$ is the wave length or length of wave packet of wave 1 and 2, and $c_{1,2}$ is the signed wave propagating velocity. This expression means that the timescale of wave-wave interaction is limited to the period of interacting waves that is in general to short for resonance. Parametric decay instability in an open system therefore can be weaker than that in a periodic system.

Divergence-to-rotation ratio of velocity in the solar wind supports this idea. We cal-

culate the root-mean-squared divergence and rotation of velocity as

$$(\nabla \cdot \boldsymbol{v})_{\mathrm{rms}} = \sqrt{\langle (\nabla \cdot \boldsymbol{v})^2 \rangle}, \tag{4.68}$$

$$(\nabla \times \boldsymbol{v})_{\mathrm{rms}} = \sqrt{\langle (\nabla \times \boldsymbol{v})^2 \rangle}, \tag{4.69}$$

where $\langle X \rangle$ denotes the average of X in t, θ and ϕ. Divergence-to-rotation ratio is defined as $(\nabla \cdot \boldsymbol{v})_{\mathrm{rms}} / (\nabla \times \boldsymbol{v})_{\mathrm{rms}}$, indicating the power balance between compressible and incompressible waves. The radial profile of this ratio is shown in Figure 4.18. An interesting feature is that the divergence-to-rotation ratio is uniform in r and is always lower than unity. A simulation with periodic boundary condition shows that, when plasma beta is around 0.1, this ratio becomes larger than unity in the saturation phase of parametric decay instability (Del Zanna et al., 2001). Thus, the parametric decay instability in the solar wind cannot reach the same saturation phase as that in a periodic system.

4.4.3 Masking effect of line-of-sight super position

To mimic the observation, we calculate the spatial profiles of line-of-sight averaged variables on $r - \theta$ plane. For each variable in Figure 4.6, assuming that the line of sight is directed in ϕ direction, we calculate the ϕ-direction-averaged values as

$$X_{\mathrm{sp}} = \frac{1}{L(r)} \int_{y_{\mathrm{min}}}^{y_{\mathrm{max}}} dy X, \tag{4.70}$$

where sp stands for superposition.

Figure 4.19 is the same as Figure 4.6 but for ϕ-direction-averaged values. Due to the superposition effect, the magnitudes of density fluctuation and Elsässer variables apparently decrease. Moreover, fine turbulent structures are no longer observable for following reasons. The number of small-scale structures along the line of sight is larger than that of large-scale structures, and therefore the small-scale structures suffer from stronger canceling effect. This result implies that we need a careful consideration in the interpretation of remote sensing of solar wind turbulence.

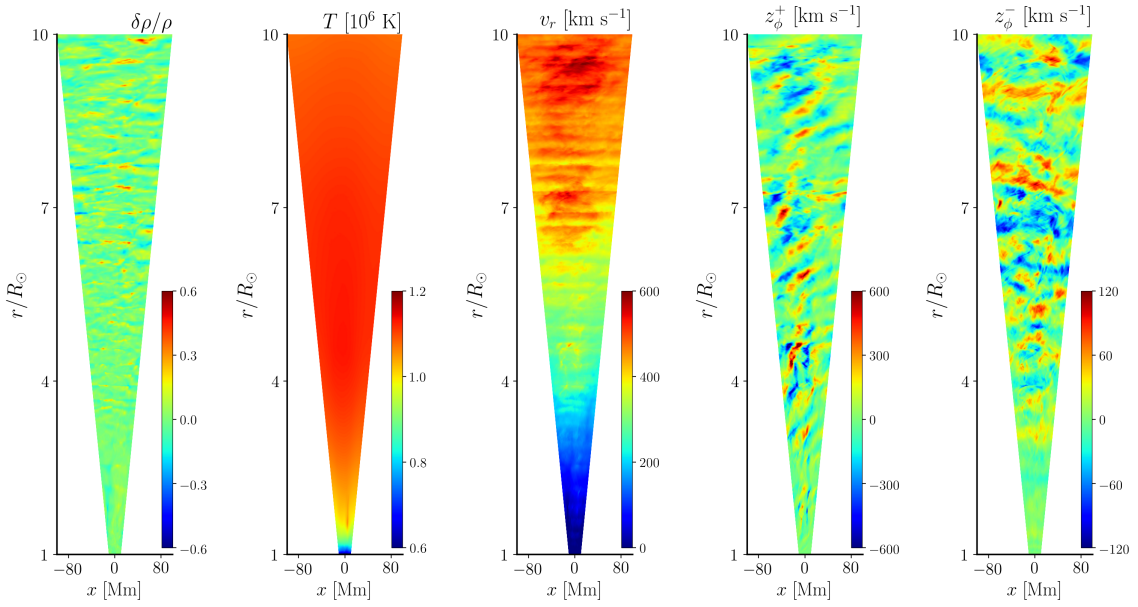

Figure 4.19: Same as Figure 4.6 but for ϕ-direction-averaged values.

4.4.4 Power spectrum with respect to perpendicular wave number

An interesting feature of the power spectra of Elsässer energies with respect to perpendicular wave number is that power indices of outward and inward Elsässer energies are different and the difference decreases as r increases. Previous works show somewhat different spectra from ours. For example, in Perez & Chandran (2013), both outward and inward spectra are Kraichnan type ($E^{\pm}(k_\perp) \propto k_\perp^{-3/2}$), regardless of radial distance. In Verdini et al. (2012a) on the other hand, the power spectrum is more like Kolmogorov type ($E^{\pm}(k_\perp) \propto k_\perp^{-5/3}$). In our understanding, these differences come from the theoretical models; Perez & Chandran (2013) solve the 3D reduced MHD equations with direct numerical calculation while Verdini et al. (2012a) solve them using shell models in which only local interaction in the wavenumber space is in consideration. It is still unclear why the introduction of compressional waves affect the power indices. Dependence on numerical resolution should also be investigated in future.

4.4.5 The lower boundary condition

The choice of boundary condition affects the numerical result. First, the horizontal spatial structure (or the correlation length) of Alfvén waves is a critical factor in this simulation. To reduce the numerical cost, we use relatively large horizontal extension (20 Mm) of the simulation domain at the bottom boundary. We also assume that the energy containing scale is the same as the box size. In van Ballegooijen & Asgari-Targhi (2016), the correlation length is fixed to 1 Mm. The turnover time of turbulence is therefore 20 times larger than van Ballegooijen & Asgari-Targhi (2016). Although we never know what is the exact correlation length in the coronal bottom, it is possible that we underestimate the turbulent dissipation due to unrealistically large horizontal scale.

The intensity of magnetic field at the coronal base is smaller compared with previous works (Suzuki & Inutsuka, 2005; Cranmer et al., 2007; Verdini et al., 2010; Lionello et al., 2014). In our setting, the magnetic field at the lower boundary is 2 G, while many studies use $5 - 10$ G for that value. This is inevitable because the super-radial expansion of the magnetic flux tube is not reproduced in our setting. Since we impose the periodic boundary condition in the horizontal direction, the magnetic field always radially expands. In terms of $B_{\rm cor}/f_{\rm exp}$, where $B_{\rm cor}$ is the coronal magnetic field and $f_{\rm exp}$ is the expansion factor of the coronal flux tube, the magnetic field strength is relatively large because $B_{\rm cor}/f_{\rm exp} = 2$ in this study while $B_{\rm cor}/f_{\rm exp} = 0.5 - 2$ in the usual setting of fast solar wind. The value of $B_{\rm cor}/f_{\rm exp}$ is important because it is correlated with the wind velocity (Suzuki, 2006; Fujiki et al., 2015).

4.5 Summary

We have conducted, for the first time, a three-dimensional, self-consistent, direct numerical MHD simulation of the solar wind acceleration. The fast solar wind with maximum temperature exceeding 10^6 K and termination velocity approximating 600 km s^{-1} is reproduced, validating our simulation. As well as 1D simulations, large density fluctuation

is observed in the wind acceleration region with magnitude correlated with the growth rate of parametric decay instability. Since the density fluctuation exceeds 10% everywhere in the simulation domain, the reflection possibly comes from the density fluctuation and therefore, the parametric decay instability triggers turbulence. The turbulence in the solar wind is characterized by imbalanced MHD turbulence in which the power spectra of outward and inward Elsässer energy spectra are different, both of which approaches Kolmogorov type spectrum as the radial distance becomes larger. As a prediction for *Parker Solar Probe*, we propose a positive correlation between density and parallel-velocity fluctuation that suggests the existence of slow-mode waves and a double power law of inward Elsässer energy spectrum with a knee point independent from r.

Chapter 5

Summary and discussion

In this thesis, 1D and 3D numerical simulations are conducted to clarify the physics of solar wind acceleration. Turbulence is a key factor in the solar wind acceleration because the turbulent dissipation generates the thermal pressure and Maxwell stress that drives plasma outward. The difficulty in the solar wind modeling lies in the solver of cascading process. In this thesis, two different approaches are used; phenomenological treatment with 1D model and direct calculation with 3D model. Specifically, our main interest is to investigate the coupling between turbulence and compressible process such as parametric decay instability. We summarize our results and discuss the achievements and limitations comparing with related works.

5.1 Summary of results

5.1.1 1D simulation

The one-dimensional simulation is motivated by the fact that two distinct models of the fast solar wind exist. Although both of them assumes the Alfvén-wave-driven model of the fast solar wind, the dissipation mechanisms are different. One assumes that Alfvén waves dissipate via reflection-driven turbulence (Cranmer et al., 2007; Verdini et al., 2010; Lionello et al., 2014), while the other assumes that parametric decay instability and resultant shock heating is the key (Suzuki & Inutsuka, 2005, 2006). We have introduced

additional terms corresponding to the phenomenological model of Alfvén wave turbulence into ideal compressible MHD equations. By doing so, we have developed for the first time a model incorporating both parametric decay instability and Alfvén wave turbulence.

The main results of our 1D simulations are as follows. First, the dominant heating process is dependent on the correlation length at the photosphere (Figure 3.3). When the photospheric correlation length is as large as the convection cell size $(1\ \mathrm{Mm})$, the shock and turbulence heatings are comparable. An interesting point is that the role of compressibility is not only adding the shock heating but also enhancing the turbulence heating by exciting reflection. Second, the mass-loss rate is independent from correlation length and dependent on energy injection or the photospheric wave amplitude (Figure 3.4). This trend is consistent with the comprehensive parameter survey based on Alfvén wave turbulence model (Cranmer et al., 2007). As the correlation length changes the location of energy dissipation, so does the location of energy dissipation but not the mass-loss rate (Hansteen & Leer, 1995; Cranmer & Saar, 2011). The scaling of mass-loss rate is given approximately as $\dot{M}_w \propto dv^{+4}$, where dv^+ denotes the velocity amplitude of outward Alfvén wave on the photosphere.

In addition to above, the onset and suppression of parametric decay instability are investigated. Due to the divergence (expansion and acceleration) of the solar wind and Doppler effect, the growth rate of PDI is reduced from that calculated by Goldstein–Derby dispersion relation. The spatial profile of the growth rate of PDI is correlated with the magnitude of density fluctuation, indicating that the origin of density fluctuation is PDI. The maximum growth rate of PDI in the solar wind acceleration region naturally explains the maximum of observed density fluctuation there (Figure 3.9).

The parametric decay instability can cause excessive reflection of Alfvén waves (Figure 3.10). In such cases, high cross helicity in the fast solar wind is no longer accountable. Thus a large part of Alfvén waves in the solar wind are not subject to PDI, that is, have lower frequency than the threshold value around $10^{-3.5}\ \mathrm{Hz}$. The radial evolution of the

outward and inward Alfvén waves in the solar wind is explained by the linear reflection.

5.1.2 3D simulation

3D simulations are conducted for more realistic modeling. Theoretical motivation is to test the concept of PDI-driven turbulence model of the fast solar wind proposed by 1D model and to investigate the spectrum of turbulence in the wind acceleration region. Meanwhile observational motivation is to predict the data for *Parker Solar Probe*. For these purposes, we have conducted the first, three-dimensional, compressible MHD simulation of the solar wind by explicitly solving the interaction between mean field and fluctuation.

Like 1D cases, large density fluctuation is observed in the wind acceleration region. By comparing the growth rate of parametric decay instability with the magnitude of density fluctuation, we have shown that the origin of density fluctuation is the parametric decay instability (Figure 4.4). The trend that the density fluctuation increases in the wind acceleration region is consistent with observation.

The turbulence in the wind acceleration region shows interesting features. Motivated by the clear spatial scale difference between outward and inward Alfvén waves, we calculate the outward and inward Elsässer energy spectra with respect to perpendicular wave number at various radial distances. Two characteristic features are found. First, the power spectrum of outward Elsässer energy is always steeper than that of inward one (Figure 4.9). This is interpreted as the difference of turbulence regime. Outward Alfvén waves are in weak turbulence with a small cascading rate regime since the amplitude of inward Alfvén wave is small. Inward Alfvén waves are, on the other hand, in strong turbulence regime with a large cascading rate. The difference of cascading time scales appears as the difference of power spectrum. Second, this difference becomes smaller as radial distance becomes larger. Interestingly, both outward and inward spectra approaches Kolmogorov-type spectrum.

We predict two characteristics of the solar wind turbulence for *Parker Solar Probe*

observation. One is the large density fluctuation in the order of 10% of mean value. A large density fluctuation would directly support the onset of parametric decay instability in the solar wind. The other is the presence of knee point in the inward Elsässer energy spectrum measured at in the *PSP* frame that depends on radial distance. The knee point possibly presents the transition point from weak to strong turbulence, and therefore, the correlation length is detectable from the knee point.

5.2 General discussion

We have listed three issues on the modeling of solar wind as a motivation of this thesis in Chapter 2. Let us discuss the insights to them obtained from our study.

5.2.1 Heating mechanism in the solar wind

Collision of bi-directional Alfvén waves drive turbulence (Iroshnikov, 1964; Kraichnan, 1965). Since the corona and solar wind are stratified, outward Alfvén waves linearly couple with inward Alfvén waves via the inhomogeneity in the radial direction, triggering turbulence (Velli et al., 1989; Matthaeus et al., 1999). This reflection-driven Alfvén wave turbulence has been widely studied in the context of heating in the corona and solar wind. Reduced MHD simulation shows that the reflection-drive turbulence has the potential to heat the corona (Oughton et al., 2001; Dmitruk et al., 2002). Using a phenomenological turbulence model proposed by Hossain et al. (1995) and Dmitruk et al. (2002), a number of studies construct the model of fast solar wind based on Alfvén wave turbulence scenario (Cranmer et al., 2007; Verdini et al., 2010; Lionello et al., 2014). In spite of successful explanation of observation, the standard model now needs modification, because direct 3D reduced MHD simulations show that the obtained heating rate is much smaller than the required value (Perez & Chandran, 2013; van Ballegooijen & Asgari-Targhi, 2016). Motivated by this background, we revisit the standard model including compressional waves.

The analysis in Chapter 3 reveals that the heating mechanism of the solar wind is correlation-length dependent. When the photospheric correlation length is comparable with the convection cell size, the turbulence heating is slightly larger than the shock heating. This result does not mean that the role of parametric decay instability is subtle. As van Ballegooijen & Asgari-Targhi (2016) show, the density fluctuation is a main driver of wave reflection (and turbulence) in the solar wind. Therefore the parametric decay instability is crucial in promoting turbulent heating in the solar wind. In fact, when the correlation length is $10\ \mathrm{Mm}$ in the coronal bottom, the heating rate by reduced MHD simulation is insufficient (Perez & Chandran, 2013), while both 1D and 3D simulation of our calculation successfully explain the fast solar wind. The parametric decay instability and resultant enhanced wave reflection is a key to understand the energetics of the solar wind.

In the standard model, Alfvén wave reflection is the source of turbulence. This is why it is called reflection-driven Alfvén wave turbulence model. Although it is true that reflection triggers turbulence even with the density fluctuation case, because the origin of density fluctuation is parametric decay instability (PDI), the turbulence should be called PDI-driven turbulence (Ghosh & Goldstein, 1994; Ghosh et al., 1994; Shoda & Yokoyama, 2018a). What is unique in our simulation is that we solve the generation of density fluctuation and the resultant amplification of turbulence in a self-consistent manner. Thus our model can be called PDI-driven turbulence model of the solar wind. We should note that in PDI-driven turbulence, not only the Alfvén wave turbulence but also the phase mixing (Heyvaerts & Priest, 1983; Magyar et al., 2017) works for the generation of finer scale fluctuations (Shoda & Yokoyama, 2018a). In addition, the presence of density fluctuation can affect the nature of turbulence. Although the importance of PDI is clarified through this thesis, the cascading mechanism within PDI-turbulence still remains unclear.

5.2.2 Turbulence in the solar wind

The solar wind turbulence is a unique laboratory of plasma turbulence (Bruno & Carbone, 2013). In-situ observations of the solar wind show several interesting behaviors of

turbulence, some of which are still unsolved. As a first step to understand the solar wind turbulence, we have investigated several fundamental properties of turbulence including compressibility.

The perpendicular power spectra of Elsässer energies show several interesting features. First, neither Iroshnikov-Kraichnan spectrum (Iroshnikov, 1964; Kraichnan, 1965) nor Goldreich-Sridhar spectrum (Goldreich & Sridhar, 1995) are observed in our simulation. One reason is that the solar wind turbulence is highly imbalanced (with large cross helicity). In such case, the power spectra of Elsässer energies should be different; minor component shows harder spectrum (Boldyrev & Perez, 2009). Such a trend is observed in our analysis. Although the numerical setting is similar, our spectra are drastically different from those in Perez & Chandran (2013). One possible reason is that the density fluctuation that is not considered in Perez & Chandran (2013) plays an important role in the energy cascade. In fact, van Ballegooijen & Asgari-Targhi (2017) point out that the cascading direction is affected by density fluctuation. However, it still remains an unsolved problem how the density fluctuation affects the power spectrum of MHD turbulence, especially in imbalanced case.

The cross helicity evolution is another interesting topic in the solar wind, Observationally, it is known that the normalized cross helicity decreases with radial distance (Bavassano et al., 1982, 2000) against the dynamical alignment effect (Dobrowolny et al., 1980; Stribling & Matthaeus, 1991; Hossain et al., 1995). Two physical mechanisms can explain such decrease: linear reflection (Velli, 1993; Cranmer & van Ballegooijen, 2005; Verdini & Velli, 2007) and parametric decay instability (Malara & Velli, 1996; Malara et al., 2000; Shoda & Yokoyama, 2016). By solving the wave propagation from the coronal base to $1\ \mathrm{au}$, we have shown that waves that are stable to parametric decay instability can explain the radial evolution of cross helicity. Therefore, at least in the inner heliosphere, the role of parametric decay instability in the cross helicity evolution is ruled out. Note, however, that parametric decay instability is required to explain the density fluctuation in the solar wind.

5.2.3 The mass-loss rate of solar/stellar wind

A motivation to study the mass-loss rate of stellar wind is to formulate the stellar angular momentum loss rate (Weber & Davis, 1967; Sakurai, 1985). The angular momentum loss by stellar wind and the dynamo activity interact with each other to regulate the stellar rotation history (Brun & Browning, 2017). One observational fact is that the mass-loss rate is correlated with the X-ray flux (Wood et al., 2002; Wood, 2004; Wood et al., 2014). Since the X-ray flux is expected to come from magnetically heated coronal loops, this observation implies a correlation between the Poynting flux and mass-loss rate.

A trend that the mass-loss rate increases with Poynting flux is confirmed by the parameter survey in Chapter 3. Approximately the mass-loss rate is proportional to the square of photospheric Poynting flux. The super-linear dependence of the mass-loss rate on the photospheric Poynting flux is also found in Suzuki & Inutsuka (2006) and Cranmer & Saar (2011). Such dependence seems controversial because previous models show that the mass-loss rate is proportional to the coronal Poynting flux (Withbroe, 1988; Hansteen & Leer, 1995). The reason for super-linear dependence is explained by the wave reflection at the transition region (Suzuki et al., 2013; Suzuki, 2018). The reflection coefficient of Alfvén waves at the transition region is dependent on the coronal density (Hollweg, 1984; Verdini et al., 2012b). When the photospheric Poynting flux increases, the coronal density also increases because of enhanced heating and chromospheric evaporation. The transmissivity of Alfvén waves is then enhanced, leading to nonlinear relation between photospheric and coronal Poynting fluxes. Specifically, when the photospheric Poynting flux becomes twice, the coronal Poynting flux becomes larger than twice due to the enhanced transmissivity, leading to super-linear dependence of mass-loss rate of the photospheric Poynting flux.

The mass-loss rate based on turbulence heating scenario (Cranmer & Saar, 2011) shows that the mass-loss rate $\dot{M}_w$ is scaled in terms of photospheric Poynting flux $F_{A,*}$ as

$$\dot{M}_w \propto F_{A,*}^{12/7}, \tag{5.1}$$

while our parameter survey yields

$$\dot{M}_w \propto F_{A,*}^2, \tag{5.2}$$

The fact that Eq.s (5.1) and (5.2) are similar suggests that the mass-loss rate is nearly independent from dissipation mechanism.

5.3 Future prospects

5.3.1 Chromosphere and transition region

The most crucial limitation in this thesis comes from the treatment of the chromosphere and transition region, both of which are ignored in a part of 1D simulations and 3D simulation. Although the chromosphere and transition region are explicitly considered and realistically reproduced in 1D simulations, we have used several assumptions that are not based on physics.

First, the radiative transfer is not solved. The chromosphere is the interface layer between optically thick (photosphere) and thin (corona) regions, and thus the radiative transfer should be solved (Carlsson & Stein, 1992, 1997; Iijima & Yokoyama, 2015, 2017). Since the temperature of the chromosphere determines the coronal density and mass loss rate, the exact treatment of radiation is crucial although it is yet unknown how accurate we need to consider radiation.

Second, turbulence is assumed not to work in the chromosphere and transition region. In spite of the presence of previous works that indicates the chromospheric turbulence (van Ballegooijen et al., 2011; Verdini et al., 2012b), we rule out the turbulent dissipation in the chromosphere because reduced MHD equation is not applicable to the chromosphere where the compressible waves are ubiquitous and strong (Tian et al., 2014; Kanoh et al., 2016). Our understanding is that a better model of turbulence is required in the chromosphere.

5.3.2 Toward a better modeling of turbulence

Although 3D MHD simulation is a powerful tool, we have several problems with it such as expensive numerical cost or difficulty in physical interpretation. To overcome such difficulties, our final goal is to reproduce 3D MHD simulation result with much simpler model with sufficient accuracy. Several models should be tested by the comparison with 3D MHD simulation.

First, the method in van Ballegooijen & Asgari-Targhi (2016) should be generalized. In van Ballegooijen & Asgari-Targhi (2016), by artificially introducing density fluctuation, the heating rate is successfully explained. Such density fluctuation should be physics-based one. As a generalization, we can set the amplitude and spatial scale of density fluctuation from, for example, the theory of parametric decay instability. Besides, the background and fluctuation can be solved simultaneously (Lionello et al., 2014) to see the dependence of wind density, temperature and velocity on the density fluctuation.

We can utilize a better model of MHD turbulence. The most important generalization compared with what we use in Chapter 3 is to solve the transport equation of correlation length (Breech et al., 2008; Cranmer & van Ballegooijen, 2012; Zank et al., 2017). Besides, the correlation lengths of outward and inward Alfvén waves should be solved separately (Zank et al., 2017; Shiota et al., 2017; Zank et al., 2018). The transport equation of the correlation lengths can be tested directly from 3D simulation. If the power spectrum of turbulence is of interest, shell model would be a powerful tool (Buchlin & Velli, 2007; Verdini et al., 2012a,b).

5.3.3 Stellar rotation and spin down

We have shown that the mass-loss rate is sensitive to the photospheric wave amplitude. Although this finding is important to understand the physics underlying mass-loss rate, we need several further steps to model the stellar rotation. First, we need to connect the stellar fundamental parameters such as luminosity, radius, etc., and the Poynting flux to give the mass-loss rate as a function of stellar fundamental parameters (Reimers, 1975;

Schröder & Cuntz, 2005). We also need to estimate the amount of open magnetic flux (See et al., 2018). The metallicity dependence should also be considered for accurate modeling (Suzuki, 2018). In the fast magnetic rotator, the rotation of mean magnetic field can directly affect the dynamics of stellar wind (Belcher & MacGregor, 1976; Johnstone, 2017), which should be taken into account as well.

Chapter 6

Concluding remarks

Since the idea of Alfvén wave heating (Alfvén, 1947; Osterbrock, 1961) and acceleration (Alazraki & Couturier, 1971; Belcher, 1971) of the fast solar wind was proposed, a number of theoretical and observational works are dedicated to more precise and comprehensive understanding of the formation of fast solar wind. Nowadays, it is widely accepted that turbulence plays a crucial role. Thanks to the development of theory, we now begin to understand the detailed physics of solar wind turbulence.

As repeatedly stressed in this thesis, a standard model has a critical problem that the heating rate is insufficient. Under the assumption that the shortage of heating is attributed to reduced MHD modeling that ignores compressional waves, we have performed compressible MHD modeling of the solar wind heating and acceleration, taking into account the turbulent heating either phenomenologically or directly. One of the main result is that the parametric decay instability (PDI), that is introduced in compressible MHD equations, plays a crucial role. First, PDI directly enhances the heating rate because shock waves are generated. Second, PDI activates turbulence by enlarging wave reflection. Owing to these effects, the heating rate becomes sufficient to reproduce the hot and fast solar wind. As a result of PDI, density fluctuation with magnitude of a few tens percent of mean value is generated. Bearing in mind that ten-percent density fluctuation enhances the turbulent heating rate by approximately a factor of 10 (van Ballegooijen & Asgari-Targhi, 2016), density fluctuation is a main source of wave reflection that triggers turbulence. Since the

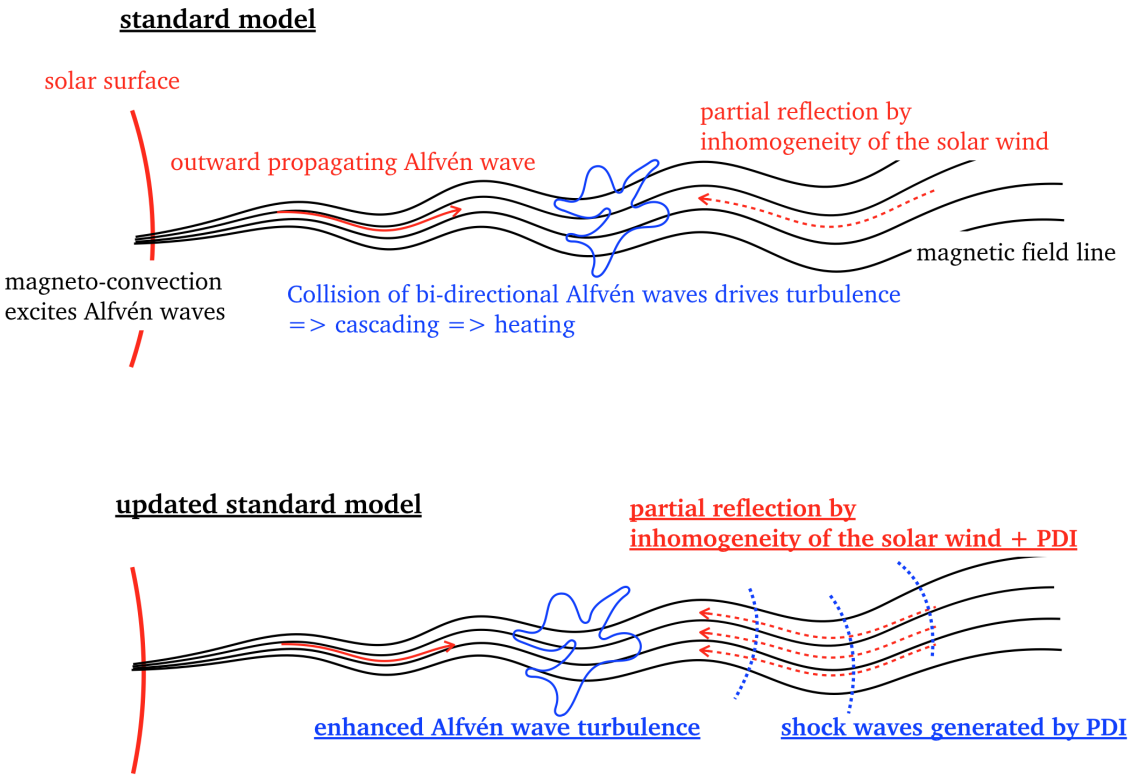

Figure 6.1: Schematic pictures of the standard model (upper figure) and the updated standard model (lower figure).

origin of density fluctuation is PDI, the turbulence in the solar wind is PDI-driven one.

Figure 6.1 shows the schematic pictures of the previous model and our model of the heating and acceleration of the fast solar wind. In the standard understanding, the reflection feeds inward Alfvén waves that triggers turbulence, and this is why the standard model is called reflection-driven Alfvén wave turbulence model. In our model, in addition to the classical reflection, PDI and resultant density fluctuation drastically enhances the amplitude of inward Alfvén waves, leading to sufficient heating rate of the solar wind. The shortage of heating rate in the standard model is therefore resolved by PDI. In this regard, our model should be called PDI-driven Alfvén wave turbulence model.

References

Alazraki, G., & Couturier, P. 1971, A&A, 13, 380

Alfvén, H. 1947, MNRAS, 107, 211

An, C.-H., Suess, S. T., Moore, R. L., & Musielak, Z. E. 1990, ApJ, 350, 309

Arge, C. N., & Pizzo, V. J. 2000, J. Geophys. Res., 105, 10465

Bale, S. D., et al. 2016, Space Sci. Rev., 204, 49

Banerjee, D., Pérez-Suárez, D., & Doyle, J. G. 2009, A&A, 501, L15

Banerjee, D., Teriaca, L., Doyle, J. G., & Wilhelm, K. 1998, A&A, 339, 208

Bavassano, B., Dobrowolny, M., Mariani, F., & Ness, N. F. 1982, J. Geophys. Res., 87, 3617

Bavassano, B., Pietropaolo, E., & Bruno, R. 2000, J. Geophys. Res., 105, 15959

Belcher, J. W. 1971, ApJ, 168, 509

Belcher, J. W., & Davis, Jr., L. 1971, J. Geophys. Res., 76, 3534

Belcher, J. W., & MacGregor, K. B. 1976, ApJ, 210, 498

Beresnyak, A., & Lazarian, A. 2008, ApJ, 682, 1070

Berger, T. E., Schrijver, C. J., Shine, R. A., Tarbell, T. D., Title, A. M., & Scharmer, G. 1995, ApJ, 454, 531

Berger, T. E., & Title, A. M. 2001, ApJ, 553, 449

Biermann, L. 1957, The Observatory, 77, 109

Boldyrev, S., & Perez, J. C. 2009, Physical Review Letters, 103, 225001

Bowen, T. A., Badman, S., Hellinger, P., & Bale, S. D. 2018, ApJ, 854, L33

Breech, B., Matthaeus, W. H., Minnie, J., Bieber, J. W., Oughton, S., Smith, C. W., & Isenberg, P. A. 2008, Journal of Geophysical Research (Space Physics), 113, A08105

Bretherton, F. P., & Garrett, C. J. R. 1968, Proceedings of the Royal Society of London Series A, 302, 529

Brun, A. S., & Browning, M. K. 2017, Living Reviews in Solar Physics, 14, 4

Bruno, R., & Carbone, V. 2013, Living Reviews in Solar Physics, 10, 2

Buchlin, E., & Velli, M. 2007, ApJ, 662, 701

Carbone, V., Marino, R., Sorriso-Valvo, L., Noullez, A., & Bruno, R. 2009, Physical Review Letters, 103, 061102

Carlsson, M., & Stein, R. F. 1992, ApJ, 397, L59

—. 1997, ApJ, 481, 500

Chandran, B. D. G. 2008, ApJ, 685, 646

Chandran, B. D. G., Dennis, T. J., Quataert, E., & Bale, S. D. 2011, ApJ, 743, 197

Chandran, B. D. G., & Hollweg, J. V. 2009, ApJ, 707, 1659

Chapman, S., & Zirin, H. 1957, Smithsonian Contributions to Astrophysics, 2, 1

Chitta, L. P., van Ballegooijen, A. A., Rouppe van der Voort, L., DeLuca, E. E., & Kariyappa, R. 2012, ApJ, 752, 48

Cho, J., & Lazarian, A. 2003, MNRAS, 345, 325

Coleman, Jr., P. J. 1968, ApJ, 153, 371

Coles, W. A., & Harmon, J. K. 1989, ApJ, 337, 1023

Cranmer, S. R. 2004, in ESA Special Publication, Vol. 575, SOHO 15 Coronal Heating, ed. R. W. Walsh, J. Ireland, D. Danesy, & B. Fleck, 154

Cranmer, S. R. 2009, Living Reviews in Solar Physics, 6, 3

Cranmer, S. R., Gibson, S. E., & Riley, P. 2017, Space Sci. Rev., 212, 1345

Cranmer, S. R., Matthaeus, W. H., Breech, B. A., & Kasper, J. C. 2009, ApJ, 702, 1604

Cranmer, S. R., & Saar, S. H. 2011, ApJ, 741, 54

Cranmer, S. R., & van Ballegooijen, A. A. 2005, ApJS, 156, 265

—. 2012, ApJ, 754, 92

Cranmer, S. R., van Ballegooijen, A. A., & Edgar, R. J. 2007, ApJS, 171, 520

Dahlburg, R. B., Einaudi, G., Taylor, B. D., Ugarte-Urra, I., Warren, H. P., Rappazzo, A. F., & Velli, M. 2016, ApJ, 817, 47

De Pontieu, B., et al. 2007, Science, 318, 1574

Dedner, A., Kemm, F., Kröner, D., Munz, C.-D., Schnitzer, T., & Wesenberg, M. 2002, Journal of Computational Physics, 175, 645

Del Zanna, L., Matteini, L., Landi, S., Verdini, A., & Velli, M. 2015, Journal of Plasma Physics, 81, 325810102

Del Zanna, L., Velli, M., & Londrillo, P. 2001, A&A, 367, 705

Derby, Jr., N. F. 1978, ApJ, 224, 1013

Dewar, R. L. 1970, Physics of Fluids, 13, 2710

Dmitruk, P., Matthaeus, W. H., Milano, L. J., Oughton, S., Zank, G. P., & Mullan, D. J. 2002, ApJ, 575, 571

Dobrowolny, M., Mangeney, A., & Veltri, P. 1980, Physical Review Letters, 45, 144

Durney, B. R. 1972, J. Geophys. Res., 77, 4042

Durney, B. R., & Hundhausen, A. J. 1974, J. Geophys. Res., 79, 3711

Edlén, B. 1943, ZAp, 22, 30

Elliott, H. A., Henney, C. J., McComas, D. J., Smith, C. W., & Vasquez, B. J. 2012, Journal of Geophysical Research (Space Physics), 117, A09102

Elsässer, W. M. 1950, Physical Review, 79, 183

Esser, R., Fineschi, S., Dobrzycka, D., Habbal, S. R., Edgar, R. J., Raymond, J. C., Kohl, J. L., & Guhathakurta, M. 1999, ApJ, 510, L63

Ferraro, C. A., & Plumpton, C. 1958, ApJ, 127, 459

Fox, N. J., et al. 2016, Space Sci. Rev., 204, 7

Fujiki, K., Tokumaru, M., Iju, T., Hakamada, K., & Kojima, M. 2015, Sol. Phys., 290, 2491

Gallet, F., & Bouvier, J. 2013, A&A, 556, A36

—. 2015, A&A, 577, A98

Ghosh, S., & Goldstein, M. L. 1994, J. Geophys. Res., 99, 13

Ghosh, S., Vinas, A. F., & Goldstein, M. L. 1994, J. Geophys. Res., 99, 19

Goldreich, P., & Sridhar, S. 1995, ApJ, 438, 763

Goldstein, M. L. 1978, ApJ, 219, 700

Gombosi, T. I., van der Holst, B., Manchester, W. B., & Sokolov, I. V. 2018, ArXiv e-prints

Grappin, R., Velli, M., & Mangeney, A. 1993, Physical Review Letters, 70, 2190

Hahn, M., D'Huys, E., & Savin, D. W. 2018, ApJ, 860, 34

Hahn, M., & Savin, D. W. 2013, ApJ, 776, 78

Hammer, R. 1982, ApJ, 259, 779

Hansteen, V. H., & Leer, E. 1995, J. Geophys. Res., 100, 21577

Hansteen, V. H., & Velli, M. 2012, Space Sci. Rev., 172, 89

Harmon, J. K., & Coles, W. A. 2005, Journal of Geophysical Research (Space Physics), 110, A03101

Hartle, R. E., & Sturrock, P. A. 1968, ApJ, 151, 1155

Heinemann, M., & Olbert, S. 1980, J. Geophys. Res., 85, 1311

Heyvaerts, J., & Priest, E. R. 1983, A&A, 117, 220

Hollweg, J. V. 1974, J. Geophys. Res., 79, 3845

—. 1976, J. Geophys. Res., 81, 1649

—. 1984, Sol. Phys., 91, 269

—. 1986, J. Geophys. Res., 91, 4111

Hollweg, J. V., & Isenberg, P. A. 2007, Journal of Geophysical Research (Space Physics), 112, 8102

Hollweg, J. V., Jackson, S., & Galloway, D. 1982, Sol. Phys., 75, 35

Holzer, T. E., & Leer, E. 1980, J. Geophys. Res., 85, 4665

Hossain, M., Gray, P. C., Pontius, Jr., D. H., Matthaeus, W. H., & Oughton, S. 1995, Physics of Fluids, 7, 2886

Iijima, H., & Yokoyama, T. 2015, ApJ, 812, L30

—. 2017, ArXiv e-prints

Iroshnikov, P. S. 1964, Soviet Ast., 7, 566

Jacques, S. A. 1977, ApJ, 215, 942

Johnstone, C. P. 2017, A&A, 598, A24

Kanoh, R., Shimizu, T., & Imada, S. 2016, ApJ, 831, 24

Kasper, J. C., et al. 2016, Space Sci. Rev., 204, 131

Kojima, M., Breen, A. R., Fujiki, K., Hayashi, K., Ohmi, T., & Tokumaru, M. 2004, Journal of Geophysical Research (Space Physics), 109, A04103

Kopp, R. A., & Holzer, T. E. 1976, Sol. Phys., 49, 43

Kraichnan, R. H. 1965, Physics of Fluids, 8, 1385

Kudoh, T., & Shibata, K. 1999, ApJ, 514, 493

Lamy, P., Quemerais, E., Llebaria, A., Bout, M., Howard, R., Schwenn, R., & Simnett, G. 1997, in ESA Special Publication, Vol. 404, Fifth SOHO Workshop: The Corona and Solar Wind Near Minimum Activity, ed. A. Wilson, 491

Landi, E. 2008, ApJ, 685, 1270

Leer, E., & Holzer, T. E. 1980, J. Geophys. Res., 85, 4681

Lionello, R., Velli, M., Downs, C., Linker, J. A., Mikić, Z., & Verdini, A. 2014, ApJ, 784, 120

Magyar, N., Van Doorsselaere, T., & Goossens, M. 2017, Scientific Reports, 7, 14820

Malara, F., Primavera, L., & Veltri, P. 2000, Physics of Plasmas, 7, 2866

Malara, F., & Velli, M. 1996, Physics of Plasmas, 3, 4427

Marsch, E., & Tu, C.-Y. 1990, J. Geophys. Res., 95, 11945

Matsumoto, T. 2018, MNRAS, 476, 3328

Matsumoto, T., & Kitai, R. 2010, ApJ, 716, L19

Matsumoto, T., & Shibata, K. 2010, ApJ, 710, 1857

Matsumoto, T., & Suzuki, T. K. 2012, ApJ, 749, 8

—. 2014, MNRAS, 440, 971

Matt, S., & Pudritz, R. E. 2008, ApJ, 678, 1109

Matt, S. P., MacGregor, K. B., Pinsonneault, M. H., & Greene, T. P. 2012, ApJ, 754, L26

Matthaeus, W. H., Zank, G. P., Oughton, S., Mullan, D. J., & Dmitruk, P. 1999, ApJ, 523, L93

McComas, D. J., et al. 2016, Space Sci. Rev., 204, 187

McIntosh, S. W., de Pontieu, B., Carlsson, M., Hansteen, V., Boerner, P., & Goossens, M. 2011, Nature, 475, 477

Meyer, C. D., Balsara, D. S., & Aslam, T. D. 2012, MNRAS, 422, 2102

—. 2014, Journal of Computational Physics, 257, 594

Miyamoto, M., et al. 2014, ApJ, 797, 51

Miyoshi, T., & Kusano, K. 2005, Journal of Computational Physics, 208, 315

Moll, R., Cameron, R. H., & Schüssler, M. 2012, A&A, 541, A68

Okamoto, T. J., & De Pontieu, B. 2011, ApJ, 736, L24

Osterbrock, D. E. 1961, ApJ, 134, 347

Oughton, S., Matthaeus, W. H., Dmitruk, P., Milano, L. J., Zank, G. P., & Mullan, D. J. 2001, ApJ, 551, 565

Parker, E. N. 1958, ApJ, 128, 664

—. 1965, Space Sci. Rev., 4, 666

Perez, J. C., & Chandran, B. D. G. 2013, ApJ, 776, 124

Perez, J. C., Mason, J., Boldyrev, S., & Cattaneo, F. 2012, Physical Review X, 2, 041005

Perkins, F. 1973, ApJ, 179, 637

Podesta, J. J., Roberts, D. A., & Goldstein, M. L. 2007, ApJ, 664, 543

Politano, H., & Pouquet, A. 1998, Geophys. Res. Lett., 25, 273

Raymond, J. C., McCauley, P. I., Cranmer, S. R., & Downs, C. 2014, ApJ, 788, 152

Reimers, D. 1975, Memoires of the Societe Royale des Sciences de Liege, 8, 369

Réville, V., Anna, T., & Marco, V. 2018, ArXiv e-prints

Réville, V., & Brun, A. S. 2017, ApJ, 850, 45

Réville, V., Brun, A. S., Matt, S. P., Strugarek, A., & Pinto, R. F. 2015, ApJ, 798, 116

Roe, P. L. 1986, Annual Review of Fluid Mechanics, 18, 337

Sagdeev, R. Z., & Galeev, A. A. 1969, Nonlinear Plasma Theory

Sakurai, T. 1985, A&A, 152, 121

Schatten, K. H., Wilcox, J. M., & Ness, N. F. 1969, Sol. Phys., 6, 442

Schröder, K.-P., & Cuntz, M. 2005, ApJ, 630, L73

See, V., et al. 2018, MNRAS, 474, 536

Sharma, P., & Hammett, G. W. 2007, Journal of Computational Physics, 227, 123

Shiota, D., Zank, G. P., Adhikari, L., Hunana, P., Telloni, D., & Bruno, R. 2017, ApJ, 837, 75

Shoda, M., & Yokoyama, T. 2016, ApJ, 820, 123

—. 2018a, ApJ, 859, L17

—. 2018b, ApJ, 854, 9

Shoda, M., Yokoyama, T., & Suzuki, T. K. 2018a, ApJ, 853, 190

—. 2018b, ApJ, 860, 17

Shu, C.-W., & Osher, S. 1988, Journal of Computational Physics, 77, 439

Spangler, S. R. 2002, ApJ, 576, 997

Spitzer, L., & Härm, R. 1953, Physical Review, 89, 977

Srivastava, A. K., et al. 2017, Scientific Reports, 7, 43147

Steiner, O., Grossmann-Doerth, U., Knölker, M., & Schüssler, M. 1998, ApJ, 495, 468

Stribling, T., & Matthaeus, W. H. 1991, Physics of Fluids B, 3, 1848

Sturrock, P. A., & Hartle, R. E. 1966, Physical Review Letters, 16, 628

Suresh, A., & Huynh, H. T. 1997, Journal of Computational Physics, 136, 83

Suzuki, T. K. 2006, ApJ, 640, L75

—. 2018, PASJ, 70, 34

Suzuki, T. K., Imada, S., Kataoka, R., Kato, Y., Matsumoto, T., Miyahara, H., & Tsuneta, S. 2013, PASJ, 65, 98

Suzuki, T. K., & Inutsuka, S.-i. 2005, ApJ, 632, L49

Suzuki, T. K., & Inutsuka, S.-I. 2006, Journal of Geophysical Research (Space Physics), 111, 6101

Suzuki, T. K., Lazarian, A., & Beresnyak, A. 2007, ApJ, 662, 1033

Tenerani, A., & Velli, M. 2013, Journal of Geophysical Research (Space Physics), 118, 7507

—. 2017, ApJ, 843, 26

Teriaca, L., Poletto, G., Romoli, M., & Biesecker, D. A. 2003, ApJ, 588, 566

Thompson, K. W. 1987, Journal of Computational Physics, 68, 1

Thurgood, J. O., Morton, R. J., & McLaughlin, J. A. 2014, ApJ, 790, L2

Tian, H., et al. 2014, ApJ, 786, 137

Tsuneta, S., et al. 2008, ApJ, 688, 1374

Usmanov, A. V., Matthaeus, W. H., Breech, B. A., & Goldstein, M. L. 2011, ApJ, 727, 84

Usmanov, A. V., Matthaeus, W. H., Goldstein, M. L., & Chhiber, R. 2018, ApJ, 865, 25

van Ballegooijen, A. A., & Asgari-Targhi, M. 2016, ApJ, 821, 106

—. 2017, ApJ, 835, 10

van Ballegooijen, A. A., Asgari-Targhi, M., Cranmer, S. R., & DeLuca, E. E. 2011, ApJ, 736, 3

van Ballegooijen, A. A., Nisenson, P., Noyes, R. W., Löfdahl, M. G., Stein, R. F., Nordlund, Å., & Krishnakumar, V. 1998, ApJ, 509, 435

van der Holst, B., Sokolov, I. V., Meng, X., Jin, M., Manchester, IV, W. B., Tóth, G., & Gombosi, T. I. 2014, ApJ, 782, 81

van Leer, B. 1979, Journal of Computational Physics, 32, 101

Velli, M. 1993, A&A, 270, 304

—. 1994, ApJ, 432, L55

Velli, M., Grappin, R., & Mangeney, A. 1989, Physical Review Letters, 63, 1807

Verdini, A., Grappin, R., Hellinger, P., Landi, S., & Müller, W. C. 2015, ApJ, 804, 119

Verdini, A., Grappin, R., Pinto, R., & Velli, M. 2012a, ApJ, 750, L33

Verdini, A., Grappin, R., & Velli, M. 2012b, A&A, 538, A70

Verdini, A., & Velli, M. 2007, ApJ, 662, 669

Verdini, A., Velli, M., Matthaeus, W. H., Oughton, S., & Dmitruk, P. 2010, ApJ, 708, L116

von Steiger, R., et al. 2000, J. Geophys. Res., 105, 27217

Vourlidas, A., et al. 2016, Space Sci. Rev., 204, 83

Wang, Y.-M., & Sheeley, Jr., N. R. 1990, ApJ, 355, 726

Weber, E. J., & Davis, Jr., L. 1967, ApJ, 148, 217

Wilhelm, K., Marsch, E., Dwivedi, B. N., Hassler, D. M., Lemaire, P., Gabriel, A. H., & Huber, M. C. E. 1998, ApJ, 500, 1023

Withbroe, G. L. 1988, ApJ, 325, 442

Withbroe, G. L., & Noyes, R. W. 1977, ARA&A, 15, 363

Wood, B. E. 2004, Living Reviews in Solar Physics, 1, 2

Wood, B. E., Müller, H.-R., Redfield, S., & Edelman, E. 2014, ApJ, 781, L33

Wood, B. E., Müller, H.-R., Zank, G. P., & Linsky, J. L. 2002, ApJ, 574, 412

Zangrilli, L., Poletto, G., Nicolosi, P., Noci, G., & Romoli, M. 2002, ApJ, 574, 477

Zank, G. P., Adhikari, L., Hunana, P., Shiota, D., Bruno, R., & Telloni, D. 2017, ApJ, 835, 147

Zank, G. P., Adhikari, L., Hunana, P., Tiwari, S. K., Moore, R., Shiota, D., Bruno, R., & Telloni, D. 2018, ApJ, 854, 32

Zhou, Y., & Matthaeus, W. H. 1990, J. Geophys. Res., 95, 10291